



UNIVERSITY OF LEEDS

# Interfacially Coupled Ferroelectric-Ferromagnetic Multiferroics



Robbie George Hunt

University of Leeds

School of Physics and Astronomy

Submitted in accordance with the requirements for the degree of

*Doctor of Philosophy*

September, 2023

## **Intellectual Property Statement**

The candidate confirms that the work submitted is his own and that appropriate credit has been given where reference has been made to the work of others.

This copy has been supplied on the understanding that it is copyright material and that no quotation from the thesis may be published without proper acknowledgement.

The right of Robbie George Hunt to be identified as Author of this work has been asserted by him in accordance with the Copyright, Designs and Patents Act 1988.

© 2023 The University of Leeds and Robbie George Hunt.

Below we detail the inclusion of published work in this thesis. Work is attributed according to the [CRediT](#) (Contributor Roles Taxonomy) system. Work from the following jointly authored publication is presented in Chapter 4 of this thesis:

‘Strain-Coupled Domains in BaTiO<sub>3</sub>(111)-CoFeB Heterostructures’,  
[R. G. Hunt](#), K. J. A. Franke, P. M. Shepley and T. A. Moore, *Phys. Rev. B*, vol. 107, American Physical Society, (2023), p. 014409. (Editor’s Suggestion).

**Work attributed to candidate:** Investigation (lead); methodology (lead); conceptualization (equal); writing - original draft (lead); visualization (lead); formal analysis (lead); writing - review and editing (equal).

**Work attributable to others:** **K. J. A. Franke:** Conceptualization (equal); formal analysis (supporting); writing - review and editing (equal). **P. M. Shepley:** Investigation (supporting); methodology (supporting), writing - review and editing (equal). **T. A. Moore:** Project administration (lead); funding acquisition (lead); conceptualization (equal); methodology (supporting); investigation (supporting); writing - review and editing (equal).

Work from the following jointly authored publication is presented in Chapter 5 of this thesis:

‘Temperature Dependence of Magnetic Anisotropy and Domain Wall Tuning in BaTiO<sub>3</sub>(111)/CoFeB Multiferroics’,  
[R. G. Hunt](#), K. J. A. Franke, P. S. Keatley, M. Rogers, P. M. Shepley and T. A. Moore, *APL Mater.* 11, 071112 (2023), (Featured).

**Work attributed to candidate:** Investigation (lead); methodology (lead); conceptualization (equal); writing - original draft (lead); visualization (lead); formal analysis (lead); writing - review and editing (equal).

**Work attributable to others:** **K. J. A. Franke:** Conceptualization (equal); formal analysis (supporting); writing - review and editing (equal). **P. S. Keatley:** Investigation (supporting), Methodology (supporting), writing - review and editing (equal). **P. M. Shepley:** Investigation (sup-

porting); methodology (supporting), writing - review and editing (equal).  
**M. Rogers:** Investigation (supporting); methodology (supporting); writing - review and editing (equal). **T. A. Moore:** Project administration (lead); funding acquisition (lead); conceptualization (equal); methodology (supporting); investigation (supporting); writing - review and editing (equal).

## Acknowledgements

This work would not have been possible without the help of all of the wonderful people at the condensed matter group in Leeds. First, I have to thank my supervisors Dr. Thomas Moore and Prof. Andrew Bell, both for the opportunity to carry out this PhD and for their support throughout. They have been nothing short of exceptionally helpful and have always had time to spare for me and for that, I will always be grateful.

There are several senior members of the group who have been exceptionally helpful and to whom I owe all of my experimental know-how. I am extremely grateful to Dr. Philippa Shepley for all of the help in the various trials and tribulations of growth and characterization, and for always providing exceptional guidance and support. The work in setting up, maintaining and understanding pulsed laser deposition would not have been possible without her assistance. Thank you to Dr. Nathan Satchell for the enlightening conversations and for always being willing to help with experimental advice and design, as well as general advice outside of science. Thanks to Dr. Kévin Franke for the useful discussions and guidance. Thanks to Dr Joseph Barker who, while not part of the project, always had useful feedback and helped me improve outside of my experimental skills.

I am grateful for the rest of the condensed matter group, of course, for their help and support in all of the ways too numerous to list here. It was a difficult time to be doing a PhD and all of the little bits of help have added up into helping overcome the various circumstances. A special thank you to all of those who have helped to maintain equipment, particularly Dr. Mannan Ali, Dr. Matthew Rogers and Dr. Philippa Shepley for all of the continued work they do keeping the main equipment of the group running.

Thanks to Jintao, Dan and Chris for the camaraderie and for helping me keep my sanity throughout the whole process, especially Dan for being a patient office neighbour. A special thanks to the members of the journal club, Ioannis, Robert, Chris, and Dr. Thomas Nussle who organized our biweekly meetings.

## Abstract

In this thesis I investigate the coupling of ferroelectric materials with thin film in-plane ferromagnets as a means of achieving voltage control of magnetism.

The strain-coupling of a (111)-cut barium titanate substrate with a sputtered CoFeB thin film has been investigated by Kerr microscopy. A one-to-one pattern transfer from ferroelectric domains to ferromagnetic domains has been observed through the imprinting of magnetoelastic anisotropy which couples magnetic domain walls to ferroelectric domain walls, where the orientation of the anisotropy rotates. We have observed two magnetoelastic coupled states in which the rotation of these magnetoelastic anisotropy axes is either  $60^\circ$  or  $120^\circ$ .

I have further investigated the magnitude of the magnetoelastic anisotropy change with temperature through the use of optical cryostat attachments to standard Kerr microscopes. The barium titanate substrate experiences three phase transitions with temperature from cubic above 420 K, to a polar tetragonal phase below 420 K, a polar orthorhombic phase below 290 K and a polar rhombohedral phase below 185 K. We observe corresponding transition behaviour in the coupled ferromagnetic layer in the magnitude of the magnetoelastic anisotropy measured from hard-axis hysteresis loops. These changes were significant, varying between  $13.6 \text{ kJ/m}^3$  and  $32.9 \text{ kJ/m}^3$  across the temperature range of interest. This has a huge impact on the domain wall properties, with the domain wall width changing significantly as the magnitude of this anisotropy changes depending on the angle of the magnetoelastic state simulation ( $60^\circ$  or  $120^\circ$ ) and the head-to-head or head-to-tail nature of the domain wall.

Based on these observations I try to understand the differences in the properties of the domain walls by means of micromagnetic simulation. For an arbitrary magnetoelastic anisotropy angle, I investigate what the impact of changing the various micromagnetic properties (saturation magnetization, anisotropy strength, magnetic field) is for each magnetoelastic angle. The resulting two-parameter landscapes are complex and reveal a strong dependence on the underlying magnetoelastic angle that can lead to the significant differences in properties seen in the previous chapters.

Finally, I present efforts to grow thin film ferroelectric materials using pulsed laser deposition. I have focused on trying to grow the single-phase multiferroic bismuth ferrite epitaxially with a conducting strontium ruthenate underlayer, a significant task that involves the optimization of two materials. I present an optimized set of conditions for both materials that I believe result in a good base from which to use this material in coupled all thin-film ferroelectric/ferromagnet heterostructures.

# CONTENTS

<b>1</b>	<b>Introduction</b>	<b>1</b>
1.1	Multiferroics . . . . .	4
1.2	Single Phase Multiferroics . . . . .	4
1.2.1	BiFeO <sub>3</sub> . . . . .	5
1.2.2	Other Multiferroics . . . . .	8
1.3	Artificial Multiferroics . . . . .	9
1.3.1	BaTiO <sub>3</sub> based Multiferroics . . . . .	9
1.3.2	PMN-PT based multiferroics . . . . .	13
1.4	Overview of the Thesis . . . . .	14
<b>2</b>	<b>Theoretical Background</b>	<b>16</b>
2.1	Introduction . . . . .	17
2.2	Ferroic Ordering . . . . .	17
2.2.1	Ferromagnetism . . . . .	18
2.2.2	Ferroelectricity . . . . .	20
2.2.3	Ferroelasticity . . . . .	22
2.3	Magnetic Domains . . . . .	23
2.3.1	Zeeman Energy . . . . .	24
2.3.2	Demagnetization Energy . . . . .	24
2.3.3	Magnetic Anisotropy . . . . .	25
2.3.4	Shape Anisotropy . . . . .	25
2.3.5	Magnetostriction . . . . .	26
2.3.6	Stoner-Wohlfarth Model . . . . .	27
2.4	Magnetic Domain Walls . . . . .	28



---

2.5	Magnetization Dynamics . . . . .	31
2.6	Summary . . . . .	32
<b>3</b>	<b>Experimental Methods</b>	<b>33</b>
3.1	Introduction . . . . .	34
3.2	DC Magnetron Sputtering . . . . .	34
3.3	Pulsed Laser Deposition . . . . .	36
3.4	X-ray Characterization . . . . .	38
3.5	Polarized Neutron Reflectometry . . . . .	41
3.6	Reflection High-energy Electron Diffraction . . . . .	43
3.7	Kerr Magnetometry & Wide-field Microscopy . . . . .	47
3.7.1	Imaging Ferroelectric Domains . . . . .	50
3.8	XMCD-PEEM . . . . .	51
3.9	SQUID-VSM Magnetometry . . . . .	52
3.10	Atomic Force Microscopy . . . . .	54
3.11	Micromagnetic Simulation . . . . .	55
<b>4</b>	<b>Pattern Transfer in BaTiO<sub>3</sub>(111)/CoFeB Films</b>	<b>59</b>
4.1	Introduction . . . . .	60
4.2	The Tetragonal Phase . . . . .	61
4.3	Sample Growth . . . . .	64
4.4	Kerr Microscopy . . . . .	64
4.5	Photo-emission Electron Microscopy . . . . .	73
4.6	Micromagnetic Simulations . . . . .	74
4.7	Summary . . . . .	78
<b>5</b>	<b>Temperature Control of Magnetic Properties in BaTiO<sub>3</sub>(111)/CoFeB Films</b>	<b>81</b>
5.1	Introduction . . . . .	82
5.2	Temperature Dependence of Crystal Phases . . . . .	82
5.3	Bulk Magnetometry . . . . .	86
5.4	Local Magnetoelastic Anisotropy . . . . .	90
5.5	Micromagnetic Simulation . . . . .	95
5.6	Summary . . . . .	98

---

<b>6</b>	<b>Effect of Magnetoelastic Anisotropy Angle on Magnetic Domain Walls</b>	<b>100</b>
6.1	Introduction . . . . .	101
6.2	Domain Wall Structure . . . . .	101
6.3	Applied Magnetic Field . . . . .	104
6.4	Micromagnetic parameters . . . . .	108
6.5	Interfacial DMI Induced Canting . . . . .	112
6.6	Domain Wall Resonance . . . . .	112
6.7	Conclusions . . . . .	115
<b>7</b>	<b>Growth and Characterization of BiFeO<sub>3</sub> thin films</b>	<b>118</b>
7.1	Introduction . . . . .	119
7.2	Substrate Characterization . . . . .	119
7.3	Growth of SrRuO <sub>3</sub> . . . . .	121
7.3.1	X-ray characterization . . . . .	121
7.3.2	AFM Characterization . . . . .	123
7.3.3	RHEED characterization . . . . .	127
7.4	Growth of BiFeO <sub>3</sub> . . . . .	128
7.4.1	Deposition Temperature . . . . .	129
7.4.2	Deposition Fluence . . . . .	133
7.4.3	PNR of BFO/CoFeB Heterostructure . . . . .	135
7.5	Summary . . . . .	142
<b>8</b>	<b>Conclusions</b>	<b>144</b>
8.1	Summary . . . . .	145
8.2	Future Work . . . . .	146
	<b>References</b>	<b>148</b>

# LIST OF FIGURES

1.1	Yearly sales for the global semiconductor industry between 2000 and 2021, from the Semiconductor Industry Association ‘2022 state of the industry report’ . . . . .	2
1.2	Doubled unit cell of bismuth ferrite in the $R\bar{3}c$ crystal phase. Indicated are the directions of polarization, $P$ , ferrodistortion, $\Omega$ , and magnetization $M$ . The Néel vector $L$ represents the orientation of the antiferromagnetic moments. Reproduced from Ref. [14]. . . . .	6
1.3	a) Schematic diagram of the cycloid structure in BFO reproduced from Ref. [23] by plotting the orientation of the magnetization in each sublattice (green arrows, top and bottom) and the resulting net moment (black arrows, middle). b) Corresponding imaging of the cycloid structure obtained from nitrogen-vacancy microscopy in the work of Zhong et al. [24]. The period $\lambda$ in the schematic would correspond to the periodicity along the y-axis of b). . . . .	7
1.4	Imaging of ferroelectric and ferromagnetic domain structures in a thin film $\text{BiFeO}_3/\text{CoFe}/\text{Pt}$ multilayer deposited on a DSO substrate. a) The ferroelectric domains in a $\text{BiFeO}_3$ layer measured by in-plane piezoresponse force microscopy. b) Ferromagnetic domains of the adjacent CoFe layer measured by XMCD-PEEM in the same region as in a). The imaging shows that there is a one-to-one pattern transfer from the BFO layer to the CoFe, indicating a strong coupling between the two layers in the stack. Reproduced from Ref. [26] . . . . .	8

1.5	Demonstration of strain-based multiferroic heterostructures. The electric field generates changes in the strain profile of the piezoelectric or ferroelectric substrate, which leads to a change in magnetization. Reproduced from Ref. [44]. . . . .	11
1.6	Vector imaging of the ferromagnetic layer in a BTO/CoFeB stack in the a) charged and b) uncharged domain wall configurations. Colour wheel (bottom right) represents the orientation of the local magnetization, represented also by the black arrows. c) Schematic representation of the ferroelectric domain structure that the magnetization is pinned to, with the imprinted strain represented as double-headed director arrows, deduced from a) and b). Dividing line in c) represents the ferroelectric domain wall. Reproduced and adapted from Ref. [47] . . . . .	12
2.1	Time reversal and spatial inversion symmetry preservation for the four ferroic orders. Schematic diagrams represent a simplistic version of the ordering in the relevant ferroic. . . . .	19
2.2	Simplistic picture of the spin-dependent density of states (indicated by $\uparrow$ and $\downarrow$ ) for a) paramagnetic state and b) the ferromagnetic state. The difference in occupancy at the Fermi level leads to a net magnetic moment. The situation in b) can also be created with an applied field for a paramagnet. . . . .	20
2.3	Demonstration of ferroelastic domains in an orthorhombic (left) to monoclinic (right) phase transition. The distortion of the $a$ and $b$ axes by angle $\beta$ leads to ferroelastic domains that are equivalent except in orientation. . . . .	23
2.4	Stoner-Wohlfarth particle with the variables used in the model to describe the energetics labelled. . . . .	28
2.5	Example pathways of magnetization reversal. Shown are the Bloch and Néel pathways corresponding to a rotation in the plane of the domain wall or perpendicular to it, alongside a 2D representation of the domain wall structure. . . . .	29
2.6	Cross-section of a) a Bloch domain wall and b) a Néel domain wall. Black arrow, $\hat{n}$ , marks the domain wall normal and blue arrows indicate the local orientation of magnetization at each point in the domain wall. . . . .	30

2.7	Torques acting on a magnetic moment (blue arrow) during magnetic field-driven precession. . . . .	32
3.1	Schematic setup of the 7-target DC magnetron sputtering system used. Each magnetron gun is equally angled towards the substrate heater (top) such that each gun is, in theory, identical. . . . .	34
3.2	Schematic diagram of a pulsed laser deposition chamber. A series of mirrors direct the UV laser onto a focal point at the surface of the target, evaporating a plume of material that is deposited on the heated substrate. . . . .	37
3.3	a) $2\theta$ - $\omega$ setup for x-ray diffraction. b) Microscopic view of the Bragg diffraction at the sample surface. . . . .	39
3.4	Schematic diagram of a RHEED setup, with the sample surface face up. Electrons are focused at a shallow angle onto the surface of the sample and the resulting 2D diffraction pattern is detected through a phosphorous screen. The pattern shown here is for a SrTiO <sub>3</sub> (100) substrate (not to scale). . . . .	44
3.5	Expected RHEED patterns for various surface features shown in steps; the feature as it appears in real space, the reciprocal space equivalent, and the resulting pattern obtained by intersecting a Ewald sphere with the reciprocal pattern. Figure reproduced from Ref. [110] . . . . .	46
3.6	Schematic diagram of a laser MOKE setup. A polarized laser incident on a material with a magnetic moment experiences some rotation of the polarization angle, measured after a cross-polarized analyzer. . . . .	48
3.7	a) Wide-field Kerr microscopy illustrated for an in-plane flux closure domain. The lens focuses the beam path onto microscopic parts of the sample and the incident polarized light, $\mathbf{E}$ , is rotated by a vector $\mathbf{k}$ away from the initial reflected position, $\mathbf{N}$ , allowing for contrast to be obtained on the other side of an analyzer. Magnetization direction within a domain is indicated by the arrows. b) Schematic diagram of the beam path that the light follows (reproduced from Ref. [112]) . . . . .	49

3.8 a) Extinction cross obtained on the back focal plane. Highlighted are the three regions corresponding to the three standard contrast directions. b) Position of LEDs within the extinction cross which can be illuminated selectively to highlight contrast regions from a). . . . . 50

3.9 Schematic diagram of a SQUID-VSM Magnetometer. The sample sits between the pickup coils and vibrates along the  $z$  axis, producing a current that is converted via the flux transformer and SQUID circuit into an output voltage. An example response function is sketched in the top right. . . . . 53

3.10 Schematic atomic force microscopy setup. The cantilever is brought close to the sample and experiences tip-surface interactions that deflect the laser and produce an output signal. Tip oscillation and height are controlled by piezoelectric motors. . . . . 54

3.11 Force-distance diagram for AFM tip-sample interactions. Shown are the regimes corresponding to the contact and non-contact modes. Figure reproduced from Ref. [119] . . . . . 56

4.1 Differences in domain structure between (111) and (100) oriented BTO substrates. a) Projections of lattice elongations onto the (111) plane in BaTiO<sub>3</sub>. The orientations in which the lattice can be elongated and that the domain walls can form through either a 60° or 120° rotation. b) An example domain structure where the lattice elongation rotates through 60° between  $t_1$  and  $t_2$ . c) The alternative 120° rotation possible for a  $t_1 - t_2$  domain structure. d) Lattice elongations possible for a (100) substrate with two in-plane  $a_1$  and  $a_2$  axes and an out-of-plane  $c$  axis. e) The in-plane domain structure possible on the (100) plane. f) The  $a - c$  domain structure possible on (100) oriented substrates. The surface is canted as a result of the change in the out-of-plane thickness by an angle  $\beta$ . . . . . 62

4.2	Schematic diagram of ferroelectric domains within a BTO(111) substrate. Both $60^\circ$ and $120^\circ$ domain walls can exist as shown in the two blown-up regions of the substrate. Arrows indicate the direction of ferroelectric polarization. Each region of ferroelectric domains contains many ferroelectric domains that alternate between two vectors with all domain walls in the same orientation. Different regions with a different set of underlying polarization vectors are then identified by a change in the orientation of ferroelectric domain walls. . . . .	65
4.3	Polarised light microscopy of ferroelectric domains in BTO(111) in three distinct regions, A, B and C, illustrating different orientations of ferroelectric domain walls. Dashed lines indicate the ferroelectric domain walls, and double headed arrows represent possible directions of lattice elongation. In each of these regions it is possible to see two distinct ferroelectric domain structures through the penetration depths of the light into the substrate which is the origin of the two sets of domains with different domain wall orientations. . . . .	66
4.4	Coupling between a) ferroelectric and b) ferromagnetic domains in BaTiO <sub>3</sub> (111)/CoFeB. Changes in magnetic contrast line up exactly with ferroelectric domain walls. The dashed line indicates the position of the same domain wall in each image. . . . .	67
4.5	Kerr effect hysteresis loops taken at varying angles for two adjacent stripe domains labelled ‘A’ and ‘B’. The angle at which the magnetic field was applied is indicated. Drift and Faraday effects have not been compensated for in these hysteresis loops. . . . .	68
4.6	Remanent magnetization taken from hysteresis loops in individual magnetic domains for a) $60^\circ$ and b) $120^\circ$ configurations, with the orientation of the easy axes marked by dashed lines. Red and blue triangles represent adjacent magnetic stripes from which data is obtained. $\Delta$ is the change in angle through the domain wall boundary, here oriented at $90^\circ$ . . . . .	70
4.7	All four field-contrast combinations for a) $60^\circ$ and b) $120^\circ$ domain patterns. Black arrows indicate the local direction of magnetization, black and yellow double-headed arrows show the direction of magnetic contrast and the direction of applied field is shown at the top of the column. . . . .	71

4.8	Magnetization reversal at an applied field of 17 mT for a) 60° and b) 120° domain configurations as a function of field angle. Direction of the magnetic field is indicated above the images and scale bars are indicated below. Each of the eight reversal processes defined by domain wall configuration and field angle is represented by a single image. A schematic representation of the experiment is shown above, with the pole pieces rotating around the sample to achieve the angles specified in a) and b).	72
4.9	a) Magnetic domain image taken using XMCD-PEEM for a 60C domain wall state. b) The result profile of the XMCD signal taken along the LP01 line, with the red dashed line being a fit to the data.	74
4.10	Micromagnetic simulations of the four domain wall configurations. Local direction of magnetization is shown by the black arrows. The underlying uniaxial anisotropy configuration is shown by the cartoon graphic on the left, and the initializing field direction is indicated above. HSV colour also represents the angle of magnetization as indicated by the colour wheel.	76
4.11	Micromagnetic simulations of the domain width (a), (c) and spin rotation (b), (d) for 60° and 120° configurations respectively as a magnetic field is rotated with respect to the ferroelectric domain wall.	77
4.12	Magnetic field dependence of domain width in (a) the 60° configuration and (b) the 120°. Left and right axes correspond to the uncharged and charged domain wall widths respectively.	79
5.1	Crystal phases of BaTiO <sub>3</sub> plotted using Vesta[117] Presented in order from high-to-low temperature, a) the cubic phase, b) the tetragonal phase, c) the orthorhombic phase and d) the rhombohedral phase. The bonds of the oxygen octahedron are highlighted to show the movement of the Ti <sup>4+</sup> ion within the octahedron. Orientations of the cubic <i>a</i> , <i>b</i> and <i>c</i> axes are shown in the bottom right of each structure.	83
5.2	Crystal lattice structure of BaTiO <sub>3</sub> on the (111) plane for the a) cubic, b) tetragonal, c) orthorhombic and d) rhombohedral phases. Only the barium atoms are shown for brevity. One direction of elongation is shown for each phase. Red arrows indicate the axis along which the crystal lattice is distorted.	85



5.3 Schematic illustration of the magnetization and anisotropy configurations in the strain-coupled ferromagnet. The domain wall configurations are labelled by the underlying angle between the magnetoelastic anisotropy axes ( $60^\circ$  or  $120^\circ$ ) and the charged or uncharged nature of the domain wall structure leading to four configurations: 60U, 60C, 120U and 120C. Black double-headed arrows indicate the direction of magnetoelastic anisotropy, blue arrows represent the direction of local magnetization. . . . . 87

5.4 MvT measurement in an applied field of 200 mT. The blue curve corresponds to data taken during cooling, with the red curve taken while heating to room temperature. The regions corresponding to the rhombohedral (**R**), orthorhombic (**O**), and tetragonal (**T**) phases of BaTiO<sub>3</sub> are indicated. Dashed lines indicate the average phase transition temperature. . . . . 88

5.5 a) Saturation magnetization (points) for 20nm CoFeB thin film coupled to a BTO(111) substrate, extracted from hysteresis loops at each temperature and the corresponding Bloch  $T^{3/2}$  law fit (dashed line). Indicated are the temperatures at which the rhombohedral (**R**), orthorhombic (**O**) and tetragonal (**T**) phase transitions occur. No significant change around these points is observed. b) Example hysteresis loop taken at room temperature without the background subtracted. Hysteresis loops are taken with a maximum field of 1 T. . . . . 89

5.6 Field-cooled and field-warmed measurements of a BTO/CoFeB heterostructure under a) 100 mT, b) 200 mT and c) 1000 mT magnetic fields. With increasing field strength the change in moment around the phase transitions of BTO is suppressed. Dashed lines indicate the average phase transition temperature. . . . . 90

5.7 Ferromagnetic domain images taken in the same vicinity for the a) rhombohedral (**R**), b) orthorhombic (**O**), and c) tetragonal phases (**T**). The magnetic stripe orientation changes to match the ferroelectric domain structure demonstrating good coupling between films across phase transitions. . . . . 91

5.8	Change in magnetic domain structure around the ferroelectric Curie temperature. At 420 K, the striped ferromagnetic domains disappear indicating that the surface strain has vanished. . . . .	92
5.9	Local magnetoelastic anisotropy imprinted in the CoFeB film by the BaTiO <sub>3</sub> (111) substrate. Dashed lines indicate the phase transitions between the rhombohedral ( <b>R</b> ), orthorhombic ( <b>O</b> ) and tetragonal ( <b>T</b> ) phases of the substrate. . . . .	93
5.10	Calculated magnitude of the lattice elongations on the (111) plane using structural data obtained by Kwei et al. [133], expressed as a percentage of the in-plane lattice parameter. . . . .	94
5.11	a) Representation of the spatially-varying anisotropy directors in micromagnetic simulations for the 60° ferroelectric domain structure, with the anisotropy axis set by a vector direction. b) Simulated magnetic domain structure initialized in the uncharged configuration. c) Simulated magnetic domain structure initialized in the charged configuration. Arrows and colour represent vector direction. . . . .	96
5.12	Domain wall width in the charged (C) and uncharged (U) configurations as a function of temperature. Numbers in the legend represent the total angle through the domain wall between the magnetoelastic anisotropy axes in adjacent stripe domains corresponding to the rotation of polarization. . . . .	97
6.1	Schematic diagram of the micromagnetic setup used for this chapter. The angle indicated, $\theta_A$ , defines the orientation of the easy axis to the domain wall. Double-headed arrows show the easy axis in each of the stripes. . . . .	102
6.2	Change in the domain wall widths for the uncharged (a) and charged (b) configurations, and the corresponding spin rotation (c,d). The spin rotation remains linear, matching closely with the angle $(180 - 2\theta_A)$ for the uncharged configurations and $2\theta_A$ for the charged configurations. . .	103
6.3	Magnetic field dependence of the domain wall width for the (a) uncharged and (b) charged domain wall states. For $\theta_A = 45^\circ$ , the scaling is linear while for the other two cases there is some curvature that is inverted from the charged to the uncharged case. . . . .	105

6.4	Full field-angle dependence of the domain wall width (a, b) and spin rotation (c,d) for the uncharged and charged domain wall states respectively. In both values, the charged and uncharged states appear as mirror images of each other, with some discrepancies introduced as a result of the magnetic charge accumulation at charged domain walls. . . . .	106
6.5	(a) Change in the field-induced magnetization deviation, $\zeta$ , calculated numerically based on Equation 6.2 for the three realistic values of $\theta_A$ . (b) Full field-angle phase diagram of these calculations with the rotation of magnetization, $\zeta$ , as the ‘heat’. . . . .	107
6.6	Change in the domain wall width and spin rotation with increasing anisotropy strength for the uncharged (a, c) and charged (b, d) domain wall configurations. Regions marked in black represent data points at which the domain wall becomes too large and covers most of the stripe. .	109
6.7	Change in the uncharged domain wall width and spin rotation with increasing saturation magnetization for the uncharged (a, c) and charged (b, d) domain wall configurations. Regions marked in black represent data points at which the domain wall did not initialize in the charged configuration. . . . .	110
6.8	Change in the uncharged domain wall width and spin rotation with increasing film thickness for the uncharged (a, c) and charged (b, d) domain wall configurations. Regions marked in black represent data points at which the domain wall did not initialize in the charged configuration. . .	111
6.9	Maximum $m_z$ vector component with varied $\theta_A$ for an interfacial DMI of 1 mJ/m <sup>2</sup> and a simulated film thickness of (a) 1 nm, (b) 20 nm. . . . .	113
6.10	(a) Power spectrum density obtained from the relaxation of the $m_z$ component of the magnetization for values of $\theta_A = 30, 45, 60^\circ$ . (b) Extracted resonant frequencies as a function of $\theta_A$ . . . . .	114
6.11	Dispersion diagrams for magnetic domain walls with (a) $\theta_A = 30$ , (b) $\theta_A = 45$ and (c) $\theta_A = 60$ excited under an AC current. . . . .	116
7.1	Substrate quality measured by a) XRD around the (200) peak and b) AFM for a single-side polished STO(100) substrate. . . . .	120

7.2	(a) X-ray reflectivity curve and (b) X-ray diffraction around the (100) substrate peak obtained from a 28 nm SRO film grown onto STO with a substrate temperature of 700 °C and fluence of 1.05 J/cm <sup>2</sup> . The fit in (a) is obtained using GenX. . . . .	122
7.3	Temperature-Fluence phase diagrams for trends in (a) film roughness and (b) film strain obtained from XRR and XRD respectively. Lattice strain is calculated relative to the substrate. . . . .	123
7.4	AFM scans of SRO layers grown at three different fluences in the range 0.98-1.17 J/cm <sup>2</sup> with a deposition temperature of 680 °C. The topographic character remains the same with islands visible on the surface for each fluence. . . . .	125
7.5	AFM scans of SRO layers grown at different temperatures in the range 620 - 700 °C with a constant deposition fluence of $f = 0.98$ J/cm <sup>2</sup> . The surface quality changes significantly, with terrace structures becoming visible at 700 °C. . . . .	125
7.6	(a) AFM scan of an SRO film grown at $T = 700$ °C with $f = 1.05$ J/cm <sup>2</sup> . (b) Linescan taken along the region indicated in blue in (a), with the ticks representing the width of the data taken. The peak-to-trough height (step height) is on the order of 3 Å. Large particles are dust contaminants on the substrate prior to deposition. . . . .	126
7.7	RHEED signal taken during deposition of SrRuO <sub>3</sub> layers at a) 660 °C, b) 680 °C, and c) 700 °C. All show signs of layer formation and increasing roughness at the initial stages of deposition. For the 660 and 680 the recovery of layer-by-layer growth shown in c) is not obtained. . . . .	128
7.8	(a) RHEED intensity for the first 10,000 pulses of an SRO layer grown at $T = 700$ °C and $f = 1.5$ J/cm <sup>2</sup> . The RHEED oscillations have a period of 15 s up to about 120s, and then a period of 90 s from 330 s onwards. (b) The following 10,000 pulses grown after a 5 minute anneal, with the intensity change during the anneal shown in the inset. Sharp jumps correspond to a realignment of the electron optics. . . . .	129
7.9	Optimized BFO surfaces grown on STO/SRO reproduced from Fig. 3 of Ref. [153] . . . . .	130

7.10 X-ray reflectivity comparison for STO/SRO/BFO films where the BFO layer has been grown at a deposition temperature varied between 660 - 760 °C. For the case of  $T = 660$ , there are additional metallic layers deposited on top of CoFeB/Pt. . . . . 131

7.11 Change in surface topography of BFO layers with increasing substrate temperature in the range of 660 - 760 °C, grown onto nominally identical SRO layers underneath. Temperature is indicated above each image. . . . 131

7.12 Zoomed-in AFM scans of the same regions from Fig. 7.11, with the region chosen to be away from the (110) oriented nanostructures for the 680 °C and 700 °C scans. Temperature is indicated above each image. . . 133

7.13 Temperature-fluence AFM phase diagram with fluence being the deposition fluence used for both the SRO and BFO layer, and temperature being the deposition temperature of the BFO only. . . . . 134

7.14 (a) PNR data obtained from the STO/SRO/BFO/CoFeB/Pt sample with raw data (points) and fits (lines) plotted above and the spin asymmetry plotted below. Fit corresponds to Model 1, where the magnetism is confined to the CoFeB layer only. (b) SLD profile corresponding to the best fit. Black dashed lines show nuclear SLD interface locations and blue dashed lines show magnetic SLD interfaces only. Data shown is for the dataset with a biasing field of 50 Oe. . . . . 137

7.15 (a) PNR data obtained from the STO/SRO/BFO/CoFeB/Pt sample with raw data (points) and fits (lines) fitted to Model 2 where a magnetic moment is allowed in the BFO layer. The spin asymmetry for the previous model (No BFO Mag.) is included and red arrows highlight the key regions where the two fits differ. (b) SLD profile corresponding to the best fit. Black dashed lines show nuclear SLD interface locations and blue dashed lines show magnetic SLD interfaces only. Data shown is for the dataset with a biasing field of 50 Oe. . . . . 140

# LIST OF TABLES

4.1	Relaxed domain wall widths for all four domain wall configurations . . .	76
7.1	Sample parameters and fitting outputs (thickness, roughness) for XRR measurements modelled with GenX. . . . .	124
7.2	Fitting parameters obtained for the model with no ferromagnetic moment fit to the BFO layer shown in Fig. 7.14. . . . .	136
7.3	Fitting parameters obtained for the weak ferromagnetic BiFeO <sub>3</sub> model shown in Fig. 7.15. . . . .	141

## Abbreviations

AC	Alternating current	PLD	Pulsed laser deposition
AFM	Atomic force microscopy	PMA	perpendicular magnetic anisotropy
BFO	Bismuth ferrite	PNR	Polarized Neutron Reflectivity
BTO	Barium titanite	RHEED	Reflection electron high-energy diffraction
Co	Cobalt	SLD	Scattering Length Density
CoFeB	Cobalt Iron Boron	SQUID	Superconducting quantum interference device
DC	Direct current	SRO	Strontium Ruthenate
DMI	Dzyaloshinskii-Moriya interaction	STO	Strontium titanite
LLG	Landau-Lifshitz-Gilbert	UHV	Ultra High Vacuum
LLGS	Landau-Lifshitz-Gilbert-Slonczewski	VSM	Vibrating sample magnetometer
MOKE	Magneto-optic Kerr effect	XMCD	X-ray magnetic circular dichroism
MRAM	Magnetoresistive random-access memory	XRD	X-ray diffraction
PEEM	Photo-emission electron microscopy	XRR	X-ray reflectivity

---

# CHAPTER 1

---

Introduction



---

The speed at which technology has advanced in the previous 20 years has been explosive. The demand and corresponding revenue for the semiconductor industry has doubled in the previous decade [1]. Cloud computing services have been adopted by technology companies of all sizes to offset the large initial investment costs in setting up the infrastructure required for modern data processing and web service requirements, which have become ubiquitous in all aspects of life, which has led to huge server farms operated by large tech companies [2]. These two examples are representative of a bigger trend - the increasing demand for more technology in every aspect of life, and it can only be expected that the demand will continue to grow. The most recent example of this has been with machine learning, a cutting-edge AI process that ‘trains’ a program to become extremely good at one specific task (such as image recognition) and requires a large amount of power and processing time to train [3]. This technology is already becoming integrated into modern life and the expansion of this technology is only going to increase the demand for processing power and increase the energy spent on these tasks.

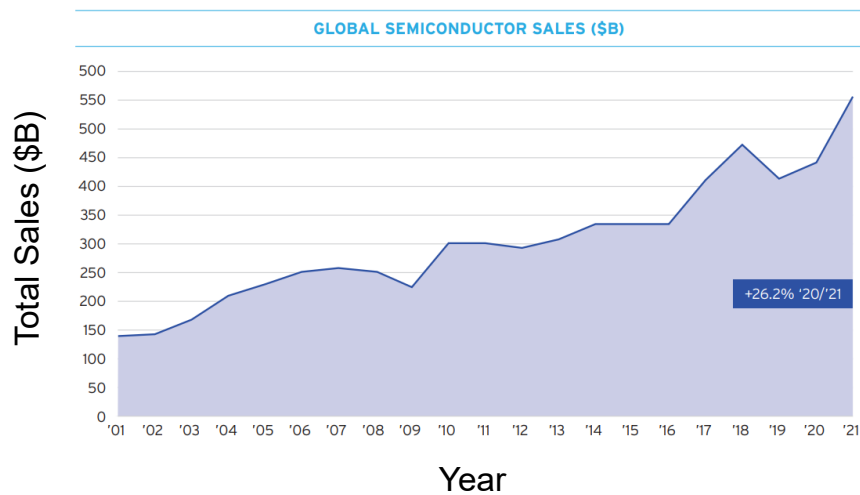


Figure 1.1: Yearly sales for the global semiconductor industry between 2000 and 2021, from the Semiconductor Industry Association ‘2022 state of the industry report’ [1].

Research to improve upon existing computing devices can be broadly categorized

---

into two goals with significant overlap: improving the performance of a device and improving the energy efficiency. The method of achieving these goals can be quite similar, with routes such as the optimization of material choices and improvement of device architecture being potentially mutually beneficial to both goals.

Improving either of these points requires an understanding of the core physics involved in these devices. The majority of components take advantage of nanometer-sized thin films of magnetic material that are controlled by magnetic fields such as in the magnetoresistive random-access memory (MRAM) device which I will use as an example. The device takes advantage of magnetoresistance, a dependence of the measured resistance upon the orientation of the magnetization to the applied current, typically using two layers of ferromagnetic thin films separated by either a non-magnetic (giant magnetoresistance) or insulating (tunneling magnetoresistance). Within this stack, one layer will have a high coercivity and is termed the ‘pinned’ layer and the other will switch magnetization at a lower applied magnetic field and is called the ‘free’ layer. The total resistance depends on if these layers are parallel or anti-parallel corresponding to a 1 or 0 respectively. Application of a magnetic field to switch the free layer is achieved by applying current along a ‘write’ electrode in the desired direction. The full device then contains an array of these tunnel junctions which will be switched many times according to the device operation.

This method of controlling the magnetic state can be improved upon. The current required to switch a magnetic layer scales as  $I^2R$  and wastes energy in the form of heat that introduces a need for heat management among other problems. To improve upon this we need to explore ways in which devices can be controlled by applications of voltages without requiring large currents. The way in which I have explored this in this thesis is through the use of multiferroics, a subset of materials that represent a very real possibility of controlling the magnetic state in these devices purely through application of voltages - no current required. This could push the energy spent on these operations down to just a few attojoules per switch, a saving of up to 4 orders of magnitude [4].

In this chapter I will describe the current progress in multiferroics, providing a sweeping overview of the current state of multiferroic research as well as some of the challenges involved in exploiting these materials. This will be focused primarily on crystalline materials that can be grown in ways that are commensurate with the fabrication

pipeline used in existing device manufacturing factories.

## 1.1 Multiferroics

Multiferroics are materials which contain more than one ferroic ordering. The more desirable of these are multiferroics with a coupled magnetic and electrical ordering as this leads to the possibility to create magnetoelectric devices. In what follows, I shall do my best to provide a detailed overview of crystal multiferroics but, even in doing this, I admit that it will not be possible to cover everything. The field and community surrounding multiferroics is exciting and incredibly engaged, with an average of 400 publications per year in the 4 years preceding 2023. To this end, I focus on the sections and results that I believe to be most relevant to this thesis.

## 1.2 Single Phase Multiferroics

A single-phase multiferroic is one which has multiple ferroic orderings intrinsically [5]. In this context, this means some electric and magnetic ordering as opposed to toroidal or elastic. These are naturally very attractive materials as they can be manipulated either magnetically or electrically to produce a response in the inverse. Naturally, as one might expect, there are other challenges in these materials that need addressing which will be discussed. I discuss the most important single-phase multiferroic for this thesis, that of bismuth ferrite, and then give broader overview of other single-phase multiferroic materials.

In this section I will describe several types of ferroelectricity, primarily displacive ferroelectrics, but also relaxor and improper geometric ferroelectric materials. A displacive ferroelectric is one which, upon going through a phase transition, experiences a displacement of ions from their equilibrium position leading to a net dipole moment [6].

Relaxor ferroelectrics are typically composites of two ferroelectric materials, which differ only by the occupying element of one atomic site such as  $\text{Pb}(\text{Mn}_{\frac{1}{3}}, \text{Nb}_{\frac{2}{3}})\text{O}_3$  (PMN) [7]. The result is that there is significant disorder within the system which leads to anomalous temperature dependent behaviour of the dielectric permittivity, among other properties, and short-range nanodomain structures originating from the structural inhomogeneity.

In the improper geometric ferroelectrics, the ferroelectricity is a secondary order parameter (improper) and the polarization is attributed to electrostatic and geometric rather than displacive effects [8, 9]. For example, in the prototypical material  $\text{YMnO}_3$  the ferroelectricity emerges due to a tilting of three of the  $\text{MnO}_5$  bipyramids towards the same oxygen ions at the centre, referred to as a trimerization. The net polarization is then only properly described by considering all three bipyramids[10].

### 1.2.1 $\text{BiFeO}_3$

It would be an oversight to mention multiferroics without talking about bismuth ferrite,  $\text{BiFeO}_3$  (BFO). This material is a room-temperature multiferroic without requiring any substitution or doping to achieve simultaneous magnetic and electric ordering pioneered by the Smolenskii group in the bulk form in the 1960s [11], and later revisited in the thin-film form by the work of the Ramesh group [12] which kick-started the trend of modern research into multiferroics [13].

The crystal structure is that of an oxide perovskite, with the  $\text{ABO}_3$  chemical formula. The normal way of visualising a perovskite unit cell is with the  $B$  atom in the centre of the unit cell, the  $A$  atom at the corners and the  $O$  atoms in an oxygen octahedron surrounding the central atom. The unit cell in Fig. 1.2 shows this as a doubled unit cell (reproduced from Ref. [14]) is the normal way of representing the unit cell of bismuth ferrite. I will explain the features of this unit cell by describing the various factors that impact the unit cell.

Bismuth ferrite is a displacive ferroelectric with antiferromagnetic ordering. It has the  $\text{R}\bar{3}\text{c}$  crystal structure up until the ferroelectric Curie temperature at 1120 K [15]. The ferroelectricity originates from the  $\text{Bi}^{3+}$  lone-pair [16]. The crystal structure leads to a displacement of the bismuth ions along the (111) crystal directions allowing for 8 total ferroelectric directions.

The Fe atoms contribute to the antiferromagnetic order by an indirect superexchange interaction mediated by the oxygen molecules [17], with a Néel temperature of 650 K. This antiferromagnetic coupling is G-type, which means that the Fe atoms align in ferromagnetic planes that are coupled to each other antiferromagnetically. There is a bulk Dzyaloshinskii-Moriya interaction (DMI) that favours the spins being perpendicular to each other which leads to a canting of the spins along the antiferromagnetic plane [18, 19]. This canting manifests as a spin cycloid with a periodicity of 62 nm [20]

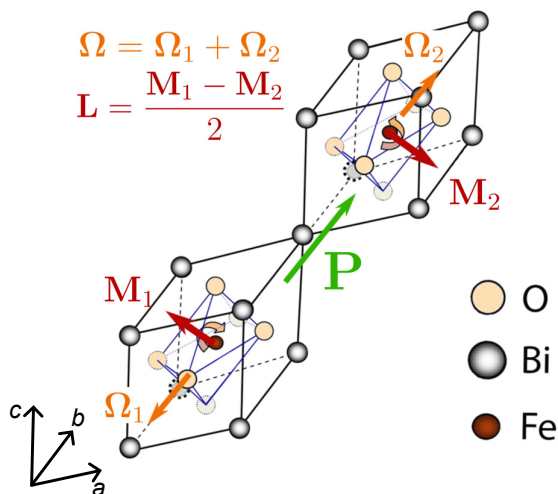


Figure 1.2: Doubled unit cell of bismuth ferrite in the  $R\bar{3}c$  crystal phase. Indicated are the directions of polarization,  $P$ , ferrodistortion,  $\Omega$ , and magnetization  $M$ . The Néel vector  $L$  represents the orientation of the antiferromagnetic moments. Reproduced from Ref. [14].

that, if the thickness is thin enough, can be truncated before one complete rotation and lead to a weak ferromagnetic moment.

The coupling through the oxygen octahedra is critical to the multiferroic nature of the material. In BFO there is an antiferrodistortive displacement that results in antiphase tilting of the oxygen octahedra that is commensurate over two unit cells, leading to a doubled unit cell in which the octahedra rotate clockwise around the polarization axis in one cell and anticlockwise in the other [21]. The antiferromagnetic ordering relies on the positions of the oxygen octahedra which will change when the ferroelectric polarization rotates, leading to a strong coupling between the ferroelectric and antiferromagnetic orders [22]. When the direction of polarization changes, the positions of the oxygen atoms are forced to change which leads to a change in the antiferromagnetic ordering.

However, this is an inherent problem in integrating this material in a way that meets the simplistic picture of voltage control laid out earlier. The magnetic ordering in this material is antiferromagnetic - meaning it exhibits no stray magnetic field and it is difficult to probe the magnetic state for read operations. There can exist a small ferromagnetic moment, but this is small (and so difficult to detect) and unreliable,

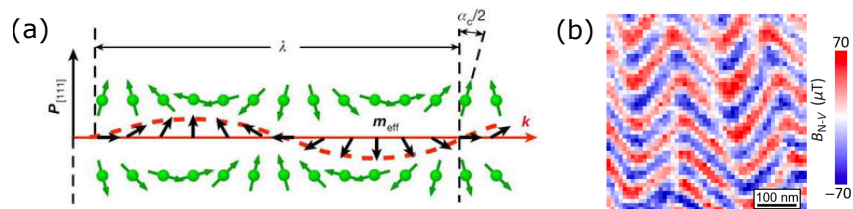


Figure 1.3: a) Schematic diagram of the cycloid structure in BFO reproduced from Ref. [23] by plotting the orientation of the magnetization in each sublattice (green arrows, top and bottom) and the resulting net moment (black arrows, middle). b) Corresponding imaging of the cycloid structure obtained from nitrogen-vacancy microscopy in the work of Zhong et al. [24]. The period  $\lambda$  in the schematic would correspond to the periodicity along the y-axis of b).

resulting primarily when the cycloid does not fully complete and so there is not a total compensation of the moment along this axis. Measurement of this cycloid is difficult, requiring high-resolution techniques such as nitrogen-vacancy microscopy to measure the small changes such as is shown in Fig. 1.3. So a significant challenge for researchers is how do we make use of the antiferromagnetism in bismuth ferrite?

One approach has been to directly make use of the antiferromagnetic order. In thin film devices, the interfacial magnetism differs considerably from the bulk of the film and particularly at antiferromagnet/ferromagnet interfaces the magnetic properties can be altered by the interfacial interaction. In the work by Martin et al. [25] they demonstrated that the antiferromagnetic phase can be used to modify the magnetic hysteresis loops of a coupled thin film, showing exchange bias (shifting of the loop along the  $x$ -axis) and coercivity enhancement dependent upon the domain structure which is voltage-controllable. The work by Heron et al. [26] showed directly using x-ray imaging that this manifests in a coupling of magnetic domains to ferroelectric (and presumably antiferromagnetic) domains shown in Fig. 1.4. There are problems with this domain-level control of magnetic devices, but these papers and the work surrounding them were instrumental and defined the principles that the devices that came afterwards would follow [27–29].

However, devices based on bilayers such as these are essentially two-phase multiferroics and will, naturally, increase the challenges in designing efficient devices. In

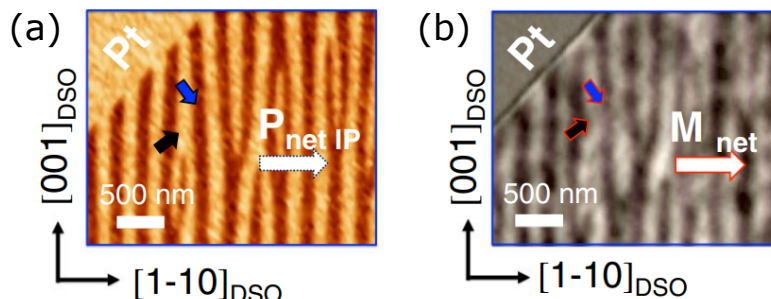


Figure 1.4: Imaging of ferroelectric and ferromagnetic domain structures in a thin film BiFeO<sub>3</sub>/CoFe/Pt multilayer deposited on a DSO substrate. a) The ferroelectric domains in a BiFeO<sub>3</sub> layer measured by in-plane piezoresponse force microscopy. b) Ferromagnetic domains of the adjacent CoFe layer measured by XMCD-PEEM in the same region as in a). The imaging shows that there is a one-to-one pattern transfer from the BFO layer to the CoFe, indicating a strong coupling between the two layers in the stack. Reproduced from Ref. [26]

recent years a much more significant amount of effort has been spent trying to exploit the properties of bismuth ferrite by itself, by study of the physics at the domain wall structures themselves [30–32], by modification of the chemical composition via doping [33, 34] to achieve a larger magnetic moment, and changing the crystal structure through the application of strain which brings with it more interesting domain textures in the tetragonal [35] and orthorhombic phases [36].

These routes are promising but it remains a challenge to integrate the material into spintronic devices beyond the early proof-of-concept work.

### 1.2.2 Other Multiferroics

While it is ideal to have a multiferroic at room temperature for device applications, if this is not a concern then there are actually many multiferroics that exhibit ferromagnetism alongside ferroelectricity, they simply exist at low temperatures that make immediate integration of these materials into devices challenging.

Notably, there is the multiferroic manganites, with the prototypical material being YmMnO<sub>3</sub> and a generic formula of  $RMnO_3$  where  $R$  is a rare-earth metal. These materials are classified as improper geometric ferroelectrics where the ferroelectric order

is a secondary effect of the trimerization of the  $\text{MnO}_5$  bipyramids [37]. This leads to interesting ferroelectric domain structures which are not strongly bound to the crystal, with particularly interesting topological properties such as clover domains which correspond to six-fold domains linked with a single topological defect in the centre [8]. Such topological features are extremely interesting for non-volatile devices. In these materials the Mn typically contributes an antiferromagnetic order and, in similar ways to that of BFO, this can be canted to produce small ferromagnetic moments with Néel temperatures in the region of 80-150 K [38]. This low Néel temperature makes measurement of these materials challenging, particularly for imaging where the antiferromagnetic and ferroelectric domains can be on the length scale of a few 10-100 nm and sensitive, high-resolution techniques have to be combined with low-temperature, high-vacuum conditions.

Several other promising room-temperature multiferroic materials have been reported. One is the hexagonal ferrite  $\text{LuFeO}_3$  [39], which also couples a ferroelectric order to an antiferromagnetic state. Of interest also is  $\text{GdFeO}_3$ , which is a ferroelectric-ferrimagnetic and has recently reported multiferroic properties at room temperature when grown on silicon [40]. Much of the research on these materials focus on engineering enhancements of the multiferroic properties at this time.

## 1.3 Artificial Multiferroics

So far I have considered the case of single-phase multiferroics. As I have outlined above these materials can be difficult to work with. A great deal of work is still being carried out exploring how to grow these materials and, though I have not touched on it, the growth of these materials is complex. Here I will discuss an alternative set of multiferroics in which the two ferroic phases, ferroelectricity and ferromagnetism, are linked artificially. I will focus only on interfacially coupled artificial multiferroics, between ferroelectric substrates and ferromagnetic thin films, but there are other approaches such as composite nanostructures [41] that will not be discussed here.

### 1.3.1 $\text{BaTiO}_3$ based Multiferroics

Barium titanate is the prototypical perovskite ferroelectric with the chemical formula  $\text{BaTiO}_3$  (BTO). It has a large polarization on the order of  $25 \mu\text{C}/\text{cm}^2$  [42] and was used



as a model perovskite ferroelectric system to probe ferroelectricity and its properties [43], particularly as it has multiple crystal phase transitions which encompass all of the allowed polar phases for perovskites, although in this section I will focus mainly on the room temperature tetragonal phase in which the lattice is elongated along one direction, the crystal (100) orientation. It is simultaneously a ferroelastic material which allows for complex domain structure in which there are more switching directions than just a  $180^\circ$  rotation. For example, there is a  $90^\circ$  pathway opened in the tetragonal phase that leads to in-plane  $a_1$  and  $a_2$  orientations of ferroelectricity and an out-of-plane  $c$  direction corresponding to the equivalent tetragonal axes. Here, the terminology  $a_1$  and  $a_2$  refers to the two equivalent in-plane axes of displacement for the BTO(100) substrate and  $c$  refers to the out-of-plane axis of displacement.

Given some of the difficulties with achieving single-phase multiferroics an interesting route towards electric control of magnetism is to create artificial multiferroics in which a magnetic phase is controlled by an electric phase. Barium titanate is a prime candidate for the electric phase and is compatible with traditional thin-film magnetism as it can be used as a substrate for deposition techniques, and has a large lattice elongation accompanying the polar distortion that can be used to impart strain which makes it useful for the field of straintronics [44]. The ideal coupling mechanism is shown in Fig. 1.5, where the strain acts as a proxy for the electric field control of magnetization, but in practice it is not so simple in ferroelectric-based heterostructures.

This was first explored in detail by Lahtinen et al. [46] by making use of a magnetostrictive thin film of CoFe to receive the strain from the BTO(100) substrate. They observed a pattern transfer from the ferroelectric domains to the ferromagnetic domains imprinted by the strain which resulted in long magnetic stripe domains that were strongly pinned to the ferroelectric domain walls.

The pinning of the domain walls by the change in local anisotropy is an intriguing side-effect of the interfacial coupling. The magnetic domain walls pinned to the ferroelectric domain walls behave differently to magnetic domains in the bulk, with the magnetization being strongly pinned to the local magnetoelastic anisotropy axes either side of the domain wall which leads to a reduction in the domain wall angle from  $180^\circ$  to  $90^\circ$ . This strong pinning of the magnetization leads to two viable routes for the magnetization to transition across the domain wall, dependent upon the field history: either a head-to-tail (uncharged) domain wall or a head-to-head (charged) domain wall. The

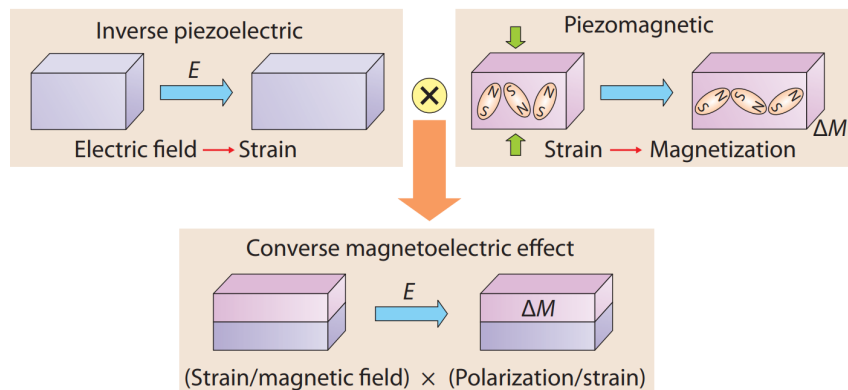


Figure 1.5: Demonstration of strain-based multiferroic heterostructures. The electric field generates changes in the strain profile of the piezoelectric or ferroelectric substrate, which leads to a change in magnetization. Reproduced from Ref. [45].

terminology of head-to-head (HtH) or head-to-tail (HtT) describes the way in which the magnetization rotates across the domain wall. With a HtH domain wall, the magnetization on either side of the domain wall points into the domain wall, leading to an accumulation of magnetic charge at the domain wall. A HtT rotation minimizes the magnetic charge at the domain wall by matching each ‘head’ with a ‘tail’ of magnetic moment.

Both domain wall states are shown in Fig. 1.6 from the work of Casiraghi et al. [47] who obtained vector images using two-component scanning electron microscopy polarization analysis (SEMPA).

Further work showed the viability of electric field control over these heterostructures with applied electric fields being used to write  $c$ -domains with out-of-plane voltages [48], modifying the in-plane strain but not completely wiping out the strain history although complete erasure of  $a$ -domains would be realized [49] and the work would be expanded upon by Franke et al. who demonstrated that with an  $a - c$  domain structure the magnetic domain wall would remain pinned to the motion of the ferroelectric domain wall under an applied electric field [50].

The viability of this electric field control has also been explored in magnetic multilayers with perpendicular magnetic anisotropy (PMA), in which the goal is to have the magnetization aligned out-of-plane. This is an important step that tests the limits

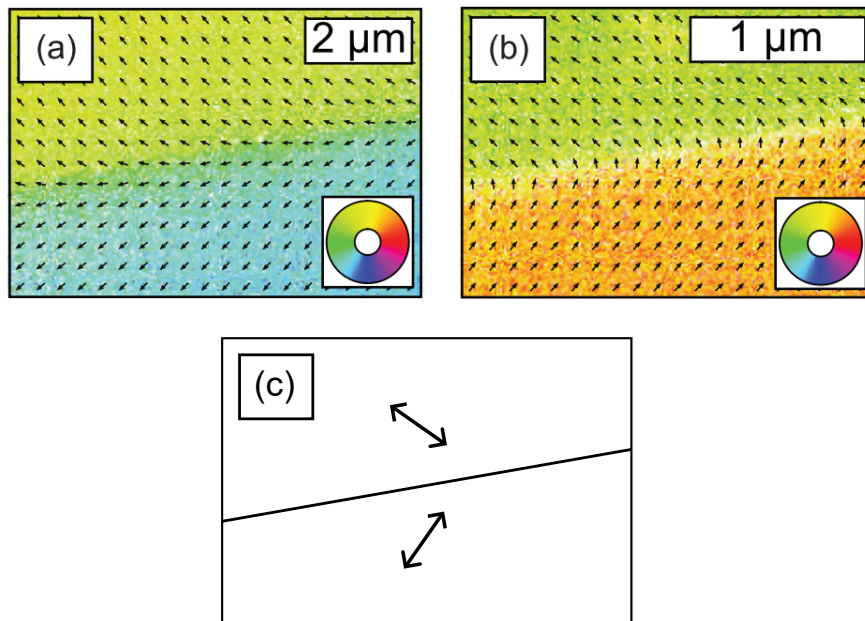


Figure 1.6: Vector imaging of the ferromagnetic layer in a BTO/CoFeB stack in the a) charged and b) uncharged domain wall configurations. Colour wheel (bottom right) represents the orientation of the local magnetization, represented also by the black arrows. c) Schematic representation of the ferroelectric domain structure that the magnetization is pinned to, with the imprinted strain represented as double-headed director arrows, deduced from a) and b). Dividing line in c) represents the ferroelectric domain wall.

Reproduced and adapted from Ref. [47].

of how viable it will be to integrate these types of artificial multiferroics into existing device architectures.

The work by Shirahata et al. [51] reported an electric-field switching of a perpendicular  $[\text{Cu}(9\text{nm})/\text{Ni}(2\text{nm})]_5$  multilayer structure grown epitaxially onto a BTO substrate buffered with a 1nm Fe layer. The large in-plane strain generated from the  $a$ -domains leads to a reduction in the PMA strength, generating polar contrast which was electrically controlled by the formation and expansion of either  $a$  or  $c$ -type domains in the BTO, and so the control here is to electrically set the film to be either in-plane or out-of-plane. It is however not expanded upon what the role of the buffer layer was, which presumably would have an in-plane magnetization also coupled to the BTO. This was followed on by showing that this ferroelectric domain wall motion also leads to a motion in the out-of-plane magnetization [52], an analogue to the work performed by Franke in purely in-plane systems.

This topic remains actively researched with investigations into the effects of the BTO quality on PMA-switching being performed [53], and the work by Cheng et al. [54] expanding even further and developing all-thin-film BTO-PMA membranes lifted off from a substrate, which could then be transferred onto a Si substrate.

There are clear limitations to the electric field control over the magnetic state in these heterostructures. Most devices will require an out-of-plane voltage to manipulate the magnetic state in a way that is space efficient. This limits the device architecture to a default state with in-plane strain to one without under an applied electric field, which is non-volatile and so limits the applications. However, these challenges are surmountable and there remains interesting work to be done with these material structures.

#### 1.3.2 PMN-PT based multiferroics

For the majority of straintronic devices, the optimization requirement is to get the most strain per applied volt to maximise device performance or modification. This makes the large domain structure of a ferroelectric like BTO potentially frustrating; it requires care in the lithography process of making the device, engineering of the domains relative to the device, or otherwise designing things in such a way that it is not important.

A popular alternative is PMN-PT, a relaxor ferroelectric [55] that has a large strain

response and is used commonly in actuators for the electromechanical response. This has been used particularly in PMA systems [56–58] in which the realistic goal, as with the BTO-PMA devices, is to control the out-of-plane anisotropy and trigger an in-plane transition with strain. These devices typically lack the large domains of BTO, even in single crystal form, which makes it ideal for applying large strains or through patterned electrode regions. A large problem in these devices remains that for voltage-controlled magnetic switching a magnetic biasing field is required to assist the switching, and solutions to reduce the reliance on this are still being explored through temperature-assistance [59], a shift to spin-orbit torque switching [60], and various other approaches.

Current research has also focused on using the reliable strain from this substrate to control other sensitive interfacial effects, such as inter-layer RKKY coupling [61] and the interfacial DM interaction [62], as it is well-suited to investigating the effect of strain on these complicated interactions by traditional sample-wide experimental techniques. The electric field control of these effects are not strictly in line with the magnetoelectric themes of other devices, in which the purpose of an applied electric field is to generate a response purely in the magnitude of the magnetization, but nonetheless are an interesting direction for electric field control of more complex devices and interactions in magnetic systems.

## 1.4 Overview of the Thesis

So far I have introduced the work that will be carried out in this thesis. This chapter has served as both a motivation for the wider research topic as a whole and as a literature review to provide the context in which this work sits.

In Chapter 2 I will present the theory necessary to understand the results, explaining first on the origin of ferroic ordering and then proceeding to delve deeper into ferromagnetism and the origin of the microstructure of ferromagnetic domains. Chapter 3 will present and explain in some detail the experimental methods that were used in this thesis.

In Chapter 4 I present results on the interfacial coupling of BaTiO<sub>3</sub>(111)/CoFeB heterostructures. I have investigated primarily the effects of the interfacial strain on the domain morphology, with particular attention to how it differs from previous work on the (100) cut of substrate. Micromagnetic simulations were performed that provide additional insight into the performed experiments.

In Chapter 5 I continued the work of Chapter 4 with a detailed study of the temperature-varied response of BaTiO<sub>3</sub>(111)/CoFeB heterostructures. Similar to Chapter 4, magnetic imaging will comprise a large portion of the results alongside sample-wide magnetometry to investigate the magnitude of magnetoelastic anisotropy as a function of temperature. The results are used to predict the response of domain wall structures to temperature variance.

Chapter 6 will expand upon the work of Chapters 4 and 5 in an endeavor to understand in more detail some of the results obtained. Through micromagnetic means, the impact of the angle of pinned magnetization on the properties of the magnetic domain walls has been investigated, focusing on the domain wall width but later exploring current-induced properties and canting of the domain wall.

Chapter 7 will change focus. In this chapter, I report on the growth of multiferroic BiFeO<sub>3</sub> thin films by pulsed laser deposition onto SrRuO<sub>3</sub> thin films on SrTiO<sub>3</sub>(100) substrates. I present results on the growth of BiFeO<sub>3</sub> thin films via pulsed laser deposition with a particular focus on the surface quality, which varies greatly with deposition parameters and is believed to have a large effect on surface ferroelectricity and antiferromagnetism.

Finally, I end with a summary of the results obtained and an outlook of the future. I discuss potential routes which could follow on from this work taking advantage of both ferroelectric substrates and thin films.

---

# CHAPTER 2

---

Theoretical Background

## 2.1 Introduction

In this chapter, we will describe the physics most closely required for this thesis. First, we will introduce the concept of ferroic materials and explain how ferromagnets and ferroelectric materials come to exist and the most important properties of them relevant to this work.

We will discuss ferromagnetism in more detail than the other ferroic orders, with a focus on the various energy terms that lead to the formation of domain structures and the consequent domain wall textures that emerge due to this. Then we will finish by discussing the equations that govern the magnetization dynamics - a crucial part of micromagnetic calculations used to predict and understand magnetic domain states.

## 2.2 Ferroic Ordering

The focus of this thesis is on multiferroic materials and so the first question we should answer is what is a ferroic material, and from this it will become more clear what a multiferroic is.

A ferroic material can be understood, at a superficial level, to be any material in which a primary order parameter displays hysteresis in response to an applied field related to that order parameter. Take for example a ferromagnet, from which ferroic materials derive their name, where the order parameter is the magnetization of the material which displays hysteretic behaviour in response to an applied magnetic field, drawing out the distinctive loops in which at some magnetic field the magnetization abruptly switches direction and there is a large response of the magnetization.

By itself, this is not enough to truly define a ferroic material. A more rigorous set of criteria based on the phenomenological behaviour of ferroics (domain structure, Curie temperature) was put forward by V. K. Wadhawan [63] as such:

1. Long-range ordering of at least one order parameter below a Curie temperature that defines the ferroic phase.
2. A ferroic material must have domain structure in which the order parameter varies that can be modified by the field corresponding to the order parameter. The velocity at which a domain wall moves will increase close to the Curie temperature.



3. There will be large, non-linear responses of macroscopic properties around the Curie temperature.
4. Close to the Curie temperature, it should be possible to undergo a field-induced phase transition.

At the time of writing, there are four types of ferroic ordering. These are ferromagnetic ordering coupling magnetization to magnetic fields, ferroelectric ordering coupling electrical polarization to electric fields, ferroelastic ordering coupling strain to stress fields and ferrotoroidic ordering coupling to a toroidal field.

Interestingly, the time reversal and spatial inversion symmetry properties of each type of ferroic is distinct from the others. A ferromagnet has a broken time-reversal symmetry, a ferroelectric has a broken space-reversal symmetry, a ferroelastic does not break either symmetry and ferrotoroidics breaks both. In this way, a grid defining the space-time symmetries of each order can be constructed such as in Fig. 2.1.

This thesis mainly focuses on ferromagnetic ordering, with ferroelectricity and ferroelasticity playing some important roles, but we will not discuss ferrotoroidicity in any detail. With a basic understanding of what a ferroic is, we will now discuss what the criteria to be a ferromagnet and ferroelectric are as well as a surface understanding of how ferroelastics come to be with a particular focus on the role of ferroelasticity in ferroelectric and multiferroic materials.

### 2.2.1 Ferromagnetism

A ferromagnetic material has a spontaneous magnetic moment under no external magnetic field (which we consider to be the remanent state) [64], as we might expect from the criteria outlined above. The origin of the long-range ordering in a ferromagnet is the exchange interaction [65].

The exchange interaction arises purely from quantum mechanical considerations. The wavefunction describing an ensemble of electrons must, by the Pauli exclusion principle [66], remain antisymmetric. This can be achieved in either the spin component of the wavefunction, corresponding to spins being anti-aligned and the spin singlet state, or in the spatial component of the wavefunction leading to the spin-triplet state in which the spin components are aligned. The singlet state naturally corresponds to no net magnetic moment while the triplet state has some magnetic moment. Which state

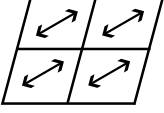
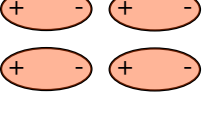
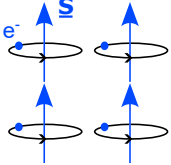
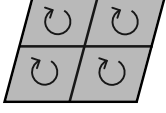
Space \ Time	Invariant	Broken
Invariant	Ferroelastic 	Ferroelectric 
Broken	Ferromagnetic 	Ferrotoroidic 

Figure 2.1: Time reversal and spatial inversion symmetry preservation for the four ferroic orders. Schematic diagrams represent a simplistic version of the ordering in the relevant ferroic.

is energetically preferable, for a system of two indistinguishable electrons, is defined by the exchange integral [67],

$$J = \frac{E_s - E_T}{2} = \int \psi_a^*(\mathbf{r}_1) \psi_b^*(\mathbf{r}_2) \hat{\mathcal{H}} \psi_a(\mathbf{r}_2) \psi_b(\mathbf{r}_1) d\mathbf{r}_1 d\mathbf{r}_2, \quad (2.1)$$

where  $E_s$  is the energy of the singlet state,  $E_T$  is the energy of the triplet state,  $\hat{\mathcal{H}}$  is the Hamiltonian operator,  $\mathbf{r}_1$  and  $\mathbf{r}_2$  are the positions of two indistinguishable electrons defined by the wavefunctions  $\psi_a$  and  $\psi_b$ , and  $J$  is the exchange constant. For positive values of  $J$ , the ferromagnetic state is favourable while for negative values the ordering will be antiferromagnetic. This is used in the Heisenberg Hamiltonian,

$$\mathcal{H} = - \sum_{i,j} J_{i,j} \vec{S}_i \cdot \vec{S}_j, \quad (2.2)$$

where  $\vec{S}_i, \vec{S}_j$  are two spin sites being evaluated. This leads to the expected behaviour where for ferromagnets it is preferred for spins to align and for antiferromagnets it is preferred to be anti-aligned.

To predict whether a material will be ferromagnetic or not based on this exchange interaction we introduce the idea of band ferromagnetism, that the density of states for a spin-up and spin-down electron will be split. It does not matter which band is

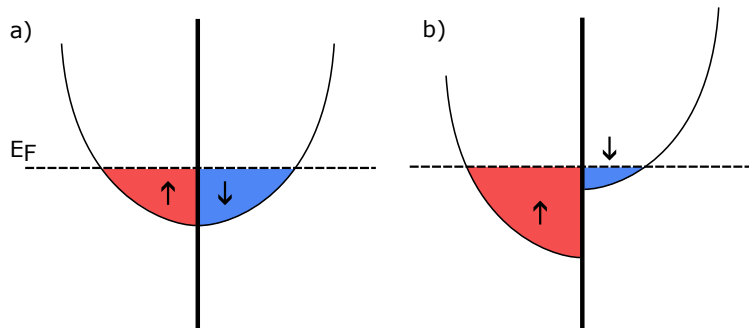


Figure 2.2: Simplistic picture of the spin-dependent density of states (indicated by  $\uparrow$  and  $\downarrow$ ) for a) paramagnetic state and b) the ferromagnetic state. The difference in occupancy at the Fermi level leads to a net magnetic moment. The situation in b) can also be created with an applied field for a paramagnet.

preferred and the convention is to consider the spin-up band  $g_{\uparrow}$  to be the majority band and the spin-down  $g_{\downarrow}$  band the minority. We illustrate this case simplistically in Fig. 2.2. In the ferromagnetic state there will be an unequal occupation of the spin bands at the Fermi level giving rise to a net magnetic moment.

With this model in mind, the Stoner criterion is put forward: For the ferromagnetic state to be preferred over the paramagnetic state, the density of states must satisfy,

$$\mu_0 \mu_B^2 \lambda g(\varepsilon_F) > 1, \quad (2.3)$$

where  $\lambda$  is the exchange coefficient, an indirect measure of the strength of the exchange interaction used within the molecular mean-field model,  $g(\varepsilon_F)$  is the density of states at the Fermi level,  $\mu_0$  is the permeability of free space, and  $\mu_B$  is the Bohr magneton. It is a combination of exchange and the material-specific density of states that makes a material ferromagnetic and also gives rise to effects such as induced ferromagnetism in nearly-ferromagnetic materials such as Pt [68].

### 2.2.2 Ferroelectricity

There are many types of ferroelectric materials. The defining feature is the presence of a spontaneous polarization which can be manipulated by an applied electric field. This can be satisfied for a variety of material structures including crystal materials (such as perovskites) [69], liquid crystals [70], and polymer [71] systems.

We will focus on the origin of ferroelectricity in perovskite oxide materials, such as  $\text{BaTiO}_3$  and  $\text{BiFeO}_3$ . These materials are crystalline in nature and the onset of ferroelectricity is at a crystal phase transition from a high-temperature non-polar phase to a low-temperature polar phase.

Ferroelectricity is defined by a spontaneous electric dipole moment meaning that it must exist without an applied electric field. In order for a dipole moment to exist the ions within the crystal must be offset such that there is a polarization within the crystal, so the crystal structure must break spatial inversion symmetry. From the available 32 point groups, 20 groups lack a centre of symmetry and allow for piezoelectric effects, that is a coupling between an applied electric field and elastic distortion. Polar groups are defined by a unique polar axis which then restricts the polar point groups to the 10 non-centrosymmetric point groups. These polar point groups define the crystal groups that ferroelectric crystals must take, and the ferroelectric phase transition is then a crystal phase transition between a polar phase below the Curie temperature to a non-polar phase above it [72].

A concept commonly associated with the ferroelectric phase transitions into these polar phases is the condensation of a ‘soft mode’ [73]. These represent vibrational phonon modes which, below a critical temperature (in the case of ferroelectric materials, the Curie temperature  $T_c$ ), ‘freeze out’ leading to a constant displacement of the atoms within the crystal structure as opposed to some transient phonon vibration. For a ferroelectric material, this condensed soft mode involves the unbalanced displacement of dissimilar ions which leads to a spontaneous polarization of the unit cell.

To understand and derive the behaviour of properties in ferroelectrics a description of the energy is useful. The free energy of a ferroelectric is typically described phenomenologically using a Landau approach. The initial approach by Devonshire, the Landau-Devonshire formalism [74], assumes that the free energy of a ferroelectric is well-defined by polarization and strain order parameters (as a deformation will change the polarization of the crystal), and that the values of each parameter in thermal equilibrium is achieved when the free energy is optimized and that this free energy function is unique. Each parameter is assumed also to be temperature dependent. Under zero strain, the free energy takes the form,

$$F = \frac{1}{2}aP^2 + \frac{1}{4}bP^4 + \frac{1}{6}cP^6 + \dots - EP, \quad (2.4)$$

with  $F$  the free energy,  $P$  the polarization of the crystal,  $E$  the electric field, and  $a$ ,  $b$ , and  $c$  constants [75]. To explain the coupling to strain I will consider only the simplest case of a uniaxial material such as BTO. The symmetry is broken along the uniaxial axis which has some strain in the absence of any applied stress, and couples to the polarization as  $\eta P^2$  to give a new free energy of,

$$F = \frac{1}{2}K\eta^2 + Q\eta P^2 + \dots + \eta\sigma \quad (2.5)$$

with  $K$  a constant that represents the deformation according to Hooke's law,  $\eta$  is the strain,  $\sigma$  is the applied stress and  $Q$  is a constant that represents the coupling strength. In other materials, the coupling term will change dependent on the symmetry.

Importantly, this means that the properties of ferroelectrics are linked strongly to the strain. This allows for the generation of strain under an applied electric field, relevant to this thesis, and also that any property that might be derived from this free energy will also depend upon the strain which leads to, among other properties, a strain-dependent Curie temperature.

### 2.2.3 Ferroelasticity

A ferroelastic material is one in which there is an elastic hysteresis loop with strain being the order parameter and the measurable phenomena and the applied stress being the field that affects it [76]. The origin of ferroelasticity is closely tied to the crystalline structure of the material and the formation of twinning domains. A representation of this is shown in Fig. 2.3 for an orthorhombic to monoclinic phase transition. In the monoclinic phase, the tilting of the  $a$  and  $b$  crystal axes results in two orientations for the unit cell which are the possible domains. Although we must point out that materials with twinning domains are not necessarily ferroelastic, all ferroelastic materials have twinning domains.

Twin domains in ferroelastic materials are needle-like domains in which the crystal structure changes between two energetically equivalent orientations. In response to stress, one crystal orientation will be preferred and these domains will grow to eventually encompass the entire sample at saturation giving rise to elastic hysteresis [77].

Ferroelasticity and ferroelectricity can exist simultaneously, leading to multiferroic materials through this overlap (although they are usually not considered as such). One example is  $\text{BaTiO}_3$  which possesses ferroelastic order. The existence of both

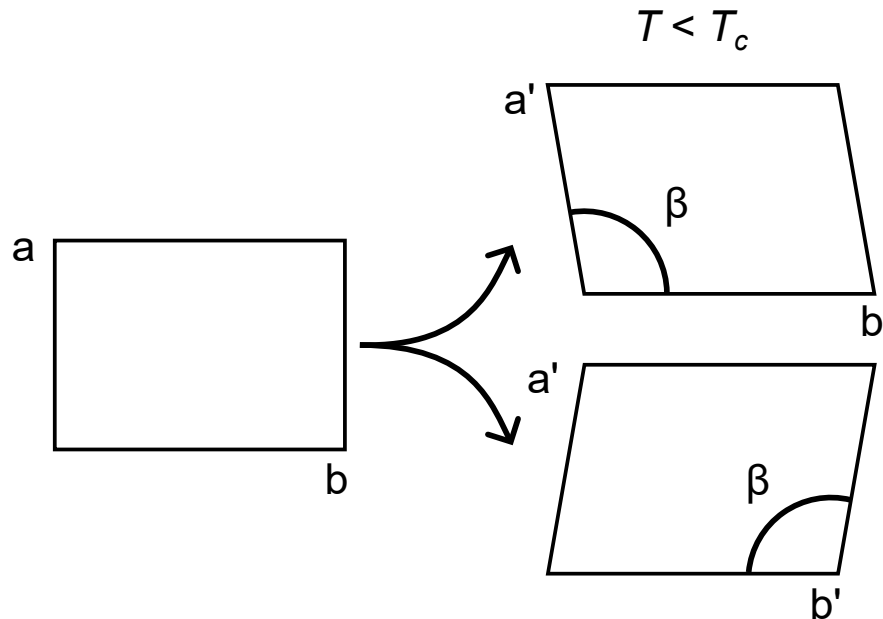


Figure 2.3: Demonstration of ferroelastic domains in an orthorhombic (left) to monoclinic (right) phase transition. The distortion of the  $a$  and  $b$  axes by angle  $\beta$  leads to ferroelastic domains that are equivalent except in orientation.

ferroelectricity and ferroelasticity leads to additional degrees of freedom in which the polarization can rotate. Rather than the polarization being forced to rotate by  $180^\circ$ , there exists the possibility of a ferroelastic switching event taking place simultaneously with the ferroelectric switching leading to domain wall angles that correspond to the ferroelastic freedom within the material - for example,  $90^\circ$  domain walls in tetragonal BTO [78]. This becomes an important factor for the ferroelectric domain structure of such multiferroics.

## 2.3 Magnetic Domains

Critical to the work carried out in this thesis is the idea of magnetic domains and domain structure within magnetic materials. Previously we have already brought this up as a requirement of ferroic materials and by extension ferromagnets, but now we will delve into the origin of ferromagnetic domains in more detail by consideration of the demagnetizing field inherent to magnetic materials. We will then discuss some of the additional energy terms that can affect the domain structure.

Similar arguments can be made that consider the various energy terms relating to ferroelectric materials, with defects playing a larger part due to how strongly the order is tied to the crystal structure, to explain the existence of ferroelectric domains and domain structure, but we will not explore this in any detail.

### 2.3.1 Zeeman Energy

We will first explain the simplest energy term that describes the response of a magnet under a static magnetic field. Under an external magnetic field, we can expect *a priori* that the magnetization should align with the field and so there should be some energy term that describes the energy saved in aligning with the field. This is called the Zeeman energy. There should be an energy gain by aligning with the magnetic field, and a cost for being antiparallel to the field, and so the Zeeman energy density takes the form,

$$E_Z = -\mu_0 \mathbf{M} \cdot \mathbf{H} \quad (2.6)$$

### 2.3.2 Demagnetization Energy

The demagnetization energy arises from the demagnetizing field of the ferromagnet. From Maxwell's equations, the divergence of the magnetic flux density  $\mathbf{B} = \mu_0(\mathbf{M} + \mathbf{H})$  must be zero which leads to a stray field that must act in opposition to the internal magnetization of the magnet [67].

The demagnetization field,  $\mathbf{H}_d$  takes the form of,

$$\nabla \cdot \mathbf{H}_d = -\nabla \cdot \mathbf{M}, \quad (2.7)$$

which has a consequent energy association of,

$$U = -\frac{\mu_0}{2} \int_V \mathbf{M} \cdot \mathbf{H}_d, \quad (2.8)$$

with a factor of  $\frac{1}{2}$  to avoid double counting. The energetic impetus is then to minimize the energy associated with this demagnetization field - best achieved by reducing the demagnetization field entirely. This leads to a competing lower-energy state with multiple domains over the monodomain state, as the introduction of *flux closure* domains minimize the total stray field.

### 2.3.3 Magnetic Anisotropy

In many magnetic materials the response of the magnetization will depend on the orientation along which the magnetic field is applied with some axis (or set of axes) being ‘easy’ and showing square hysteresis loops, and another being ‘hard’ along which there is a linear response until the magnetization is fully saturated. This is referred to as magnetic anisotropy and can arise from a number of factors including the magnetocrystalline anisotropy related to the crystal structure of a magnetic material, a shape anisotropy relating to the shape-specific demagnetizing field, and (in thin films) various forms of interface-limited anisotropy such as magnetostriction. In the absence of any anisotropy, the hysteresis behaviour of the magnet is equivalent in all directions of applied field.

The simplest form of anisotropy is that of a uniaxial anisotropy, a director that is energetically favourable for the magnetization to be aligned along and from which there is some energetic penalty to deviate. An energy density term of this type can be described as,

$$E_K = K \cos^2(\theta), \quad (2.9)$$

where  $K$  is the anisotropy constant and  $\theta$  is the angle between the magnetization and the easy axis. The way in which anisotropy can arise depends heavily on the material system and the growth technique. In crystalline magnetic materials, there can be a large magnetocrystalline contribution that will be more complex than this simple uniaxial picture. In amorphous thin-film magnets, a uniaxial anisotropy can be introduced by an in-plane growth field which affects the preferred orientation of magnetic grains during the deposition process which creates a preferred bond orientation [79].

### 2.3.4 Shape Anisotropy

An immediate consequence of the demagnetizing field is the creation of a shape anisotropy. The effect of the shape the demagnetizing field can be explicitly included by the introduction of a demagnetizing tensor such that,

$$\mathbf{H}_d = -\mathcal{N}\mathbf{M} \quad (2.10)$$

where  $\mathcal{N}$  is the demagnetization tensor. The tensor is usually defined such that the diagonal elements correspond to the coordinate axes of magnetization and so the diagonals correspond to the demagnetization factor,  $D_i$ , of the system along the  $i$  axis. The



trace of these diagonals is unity and so the sum of the demagnetization factors must obey,

$$D_x + D_y + D_z = 1, \quad (2.11)$$

with  $x$ ,  $y$  and  $z$  chosen here for a Cartesian coordinate system although the same will hold true for any coordinate system. These demagnetization factors can be worked out analytically for simple systems but are generally found through computational methods [80].

The introduction of an anisotropy will be demonstrated by consideration of the demagnetization factors of a sphere and an ellipsoid. In a perfectly spherical magnetic system, a symmetry argument can be made to find the demagnetization factors. As all directions are equivalent, and the sum of all factors must be 1, the demagnetization factors are,

$$D_x = D_y = D_z = \frac{1}{3}, \quad (2.12)$$

and so there is effectively no shape anisotropy in a spherical particle. If instead one of the axes is elongated, then the same magnetization will be spread over a longer distance leading to a lower density of magnetic charge, which results in a lower magnitude of the demagnetization field if the magnetization is pointing along this direction - the introduction of an easy axis. This is reflected in the change of the demagnetization factors. If the axes  $x$  and  $y$  remain the same then  $D_x = D_y$  and, from the trace of the demagnetization tensor,  $D_z = 1 - 2D_x$ . The exact change will depend on the magnitude of elongation, but already with a small perturbation to the ellipsoid it becomes a complex process to calculate an exact demagnetization factor, the details of which for the generalized ellipsoid case (in which all axes are allowed to vary) can be seen in Ref. [81].

This difference in demagnetizing energy along different directions is the cause of shape anisotropy. For thin-film materials, that are essentially infinite along the  $x$  and  $y$  directions but finite along  $z$ , the demagnetizing factors are  $D_x = D_y = 0$  and  $D_z = 1$ , which leads to a preference for the magnetization to lie in-plane over out-of-plane.

### 2.3.5 Magnetostriction

Magnetostriction is the coupling of a material's dimensions to its magnetization state. A traditional magnetostrictive material, such as terfenol-D [82], will expand or contract dependent upon the rotation of the magnetic moments [83].

More relevant to the thin film magnets is inverse magnetostriction, the Villari effect [84]. Here the change in applied stress results in a change in the magnetization state.

This leads to an anisotropic energy term of,

$$E = \frac{3}{2}\sigma\lambda\sin^2(\theta), \quad (2.13)$$

with a magnetostrictive constant,  $\lambda = \frac{dl}{l}$ , and applied stress,  $\sigma$ . For stress applied along one direction, this effectively acts as a uniaxial anisotropy term that is magnetoelastic in origin and has the form  $K_{me}\cos^2(\theta)$ .

### 2.3.6 Stoner-Wohlfarth Model

A useful model to define at this point is that of the Stoner-Wohlfarth (SW) particle [85]. Say that we have a magnetic ellipsoid, there is an inherent shape anisotropy that results in a uniaxial anisotropy along the long axis of the ellipsoid. This is a useful model to understand the origin of hysteresis and the effect of anisotropy on these loops.

The model makes a few assumptions. First, the magnitude of the magnetization does not vary and rotates coherently in response to the applied magnetic field, applied along one axis only. Only a single domain is considered in which the anisotropy is uniaxial, corresponding to a single elliptical grain. Only two energy terms are considered, the previously discussed Zeeman energy (Equation. 2.6) resulting from the interaction of the particle with a magnetic field and the uniaxial anisotropy energy (Equation. 2.9) resulting from the shape anisotropy. The model assumes there is only one magnetic domain and so does not take into account the effects of domain nucleation and expansion. The model is athermal and likewise does not reproduce temperature-dependent effects seen in hysteresis loops.

The total energy of the SW particle can be written as,

$$E = K_u V \sin^2(\varphi - \theta) - \mu_0 M_s V H \cos\varphi, \quad (2.14)$$

where  $\varphi$  is the angle between the magnetization and the applied magnetic field direction,  $\theta$  is the orientation of the easy axis, and  $K_u$  is the magnitude of the uniaxial anisotropy constant. A schematic diagram of the SW particle with the relevant vectors is shown in Fig. 2.4. The stable orientation for the magnetization at any value of  $H$  is determined by calculating the value of  $\theta$  at which  $\partial E/\partial\varphi = 0$  for each value and then analytically solving for  $\varphi$ .

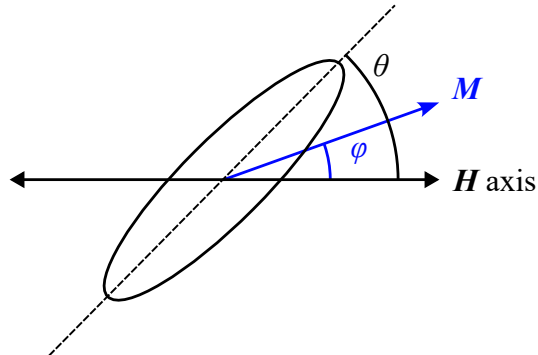


Figure 2.4: Stoner-Wohlfarth particle with the variables used in the model to describe the energetics labelled.

A useful result of this simple model comes from minimizing the energy with respect to the  $\theta$ , obtaining the hard-axis anisotropy field,  $H_K$ :

$$H_K = \frac{2K}{\mu_0 M_s} \quad (2.15)$$

This is a powerful result; from this simple model we can relate hard axis hysteresis loops to the magnitude of the anisotropy in a magnetic system and this will be used in the thesis. In the SW model, the anisotropy field is the same value as the coercivity along the easy axis. In more complex systems this is not usually the case. Nonetheless the results of this model are extremely useful for describing magnetic systems with uniaxial anisotropy.

## 2.4 Magnetic Domain Walls

One of the interesting properties of materials with domain structures is the domain walls themselves, regions in which the order parameter (magnetization) transitions between different orientations between the two domains. We will only explain the case of magnetic domain walls. The simplest case is a reversal by  $180^\circ$  from an ‘up’ to a ‘down’ magnetization (whether that be in the  $x$ ,  $y$  or  $z$  orientation).

The most relevant part of the domain wall is the rotation of the magnetization and so we use polar coordinates and consider the orientation of the magnetization. The magnetization rotates from a value of  $\varphi = 90^\circ$  to  $\varphi = -90^\circ$ . From Fig. 2.5, there are two possible pathways for the magnetization to rotate, the Bloch pathway which is a

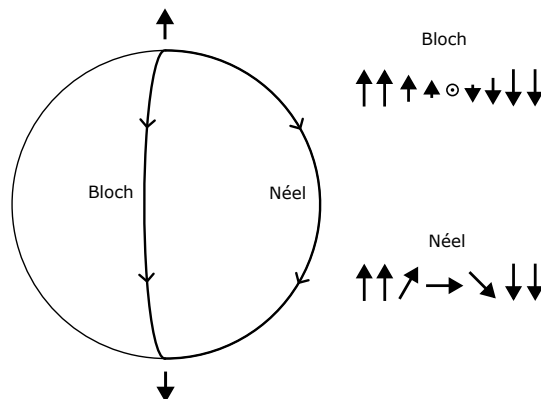


Figure 2.5: Example pathways of magnetization reversal. Shown are the Bloch and Néel pathways corresponding to a rotation in the plane of the domain wall or perpendicular to it, alongside a 2D representation of the domain wall structure.

rotation in the plane of the domain wall and a Néel pathway which rotates perpendicular to the domain wall. Of these two, the lowest energy pathway is the Bloch-type domain wall as this introduces no magnetic charge at the domain wall and so this minimizes the stray field at the domain wall [86]. A more detailed cross-section of each domain wall can be seen in Fig. 2.6 in which the orientation of the magnetization at various points in the domain wall are shown. For a Bloch domain wall, the domain wall energy  $\gamma_w$  can then be expressed as,

$$\gamma_w = \int_{-\infty}^{\infty} [A\varphi(x)'^2 + K \cos^2 \varphi(x)] dx, \quad (2.16)$$

where  $\varphi$  is the orientation of the magnetization and as a function of  $x$  perpendicular to the domain wall,  $K$  is the anisotropy constant and  $A$  is the micromagnetic exchange stiffness. Far from the domain wall, at  $x = \pm\infty$ , the magnetization takes a value of  $\varphi = \mp 90^\circ$  and does not vary in space so there is no contribution to the domain wall energy.

By solving for the function  $\varphi(x)$  that minimizes the domain wall energy it is possible to understand two useful quantities about domain walls: the domain wall energy  $\gamma_w = 4\sqrt{AK}$ , and the domain wall width,  $\delta_b = \pi\sqrt{A/K}$  [87]. The values obtained from this simple model are frequently used as estimates even in more complicated magnetic systems [32].

In this model it is possible to derive the spin profile of the domain wall,  $\varphi(x) =$

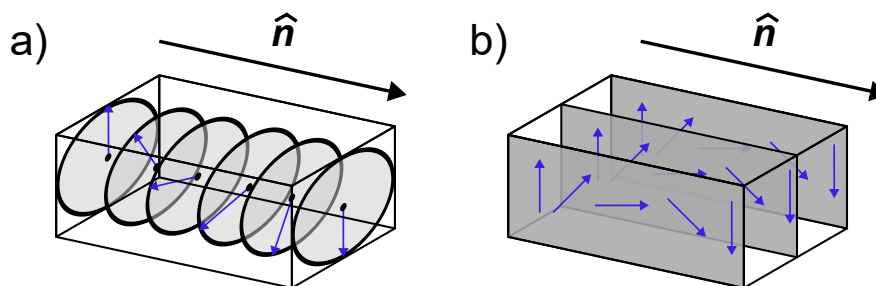


Figure 2.6: Cross-section of a) a Bloch domain wall and b) a Néel domain wall. Black arrow,  $\hat{n}$ , marks the domain wall normal and blue arrows indicate the local orientation of magnetization at each point in the domain wall.

$\tanh(x/\delta_b)$  and this is indeed useful for defining the domain wall width and particularly fitting domain wall profiles.

Stabilizing of a Néel domain wall requires an additional energy term that outbalances the additional cost associated with the magnetic charge, and so stray field, that exists at the domain wall. This can come from an anisotropy term of sufficient strength [88], such as an in-plane stress, or from a Dzyaloshinskii-Moriya interaction in perpendicularly magnetized systems [89].

In the case of anisotropy within the system, it is also possible to reduce the angle of the domain wall if there are multiple competing anisotropy directions. Indeed, this will also be seen in systems in which the demagnetization energy dominates and flux closure domains become significant. Consider the typical flux closure domain of a bar magnet - the magnetization will rotate by  $90^\circ$  at the ends of the bar magnet leading to domain walls with a reduced angle of  $90^\circ$ . In fact, it does not overly complicate things - we can define a reduced angle of magnetization [90],

$$\varphi' = \left( \varphi - \frac{|\varphi_{\frac{\Delta}{2}} - \varphi_{-\frac{\Delta}{2}}|}{2} \right) \frac{180}{|\varphi_{\frac{\Delta}{2}} - \varphi_{-\frac{\Delta}{2}}|}, \quad (2.17)$$

where  $\varphi'$  is the reduced magnetization angle and  $\varphi_{\pm\frac{\Delta}{2}}$  are the angles of magnetization far from the domain wall, effectively the angle to which the magnetization is pinned away from the domain wall that leads to the reduced domain wall angle.

This is useful with a more generalized definition of the domain wall for use with domain walls in which there is a significant magnetic charge at the domain wall. The

integral definition put forward by Jakubovics [91],

$$\delta_J = \int_{-\infty}^{\infty} \cos^2 \varphi(x) dx, \quad (2.18)$$

has the benefit of being adaptable to more complicated domain wall structures, such as those that have a magnetic charge at the domain wall, while maintaining agreement with the result for Bloch domain walls.

## 2.5 Magnetization Dynamics

Under an applied magnetic field a magnetic moment will begin to precess around the applied field in order to reach alignment. The dynamics of a magnetic moment can be described by the Landau-Lifshitz equation [92],

$$\frac{d\mathbf{M}}{dt} = -\gamma \mathbf{M} \times \mathbf{H}_{\text{eff}} - \lambda \mathbf{M} \times (\mathbf{M} \times \mathbf{H}_{\text{eff}}), \quad (2.19)$$

with a term that describes the precession,  $-\gamma \mathbf{M} \times \mathbf{H}_{\text{eff}}$  and one that describes the damping of the precession by a torque acting perpendicular to the direction of precession which causes the magnetization to eventually align with the field,  $\lambda \mathbf{M} \times (\mathbf{M} \times \mathbf{H}_{\text{eff}})$  where  $\lambda$  is a phenomenological damping parameter. The effects of internal fields (magneto-static, Dzyaloshinskii-Moriya, etc) and external fields are combined into an effective field term  $H_{\text{eff}}$ .

There are two modifications that are made to better describe the magnetization dynamics. The first change is to the damping term, and the conversion from a phenomenological term to the Gilbert [93] damping. Starting from a Lagrangian consideration of the equations of motion, Gilbert derived the Landau-Lifshitz-Gilbert (LLG) equation as,

$$\frac{d\mathbf{M}}{dt} = -\gamma \mathbf{M} \times \mathbf{H}_{\text{eff}} - \frac{\alpha}{M} (\mathbf{M} \times \frac{\partial \mathbf{M}}{\partial t}), \quad (2.20)$$

where  $\alpha$  is the Gilbert damping. For small values of  $\alpha^2 \ll 1$  there is no change, and the two equations describe the same dynamics. This rate-dependent damping factor becomes important for large  $\alpha$  in which precession is suppressed.

The second modification is the inclusion of a Slonczewski [94] term that includes the effect of spin-transfer torque from spin currents which is useful for describing the current-driven dynamics of a magnetic system. This leads to a Landau-Lifshitz-Gilbert-Slonczewski (LLGS) equation of,

$$\frac{d\mathbf{M}}{dt} = -\gamma \mathbf{M} \times \mathbf{H}_{\text{eff}} - \frac{\alpha}{M} (\mathbf{M} \times \frac{\partial \mathbf{M}}{\partial t}) - \frac{\mathbf{M} \times (\mathbf{M} \times \mathbf{I}_s)}{qN_s M_s}, \quad (2.21)$$

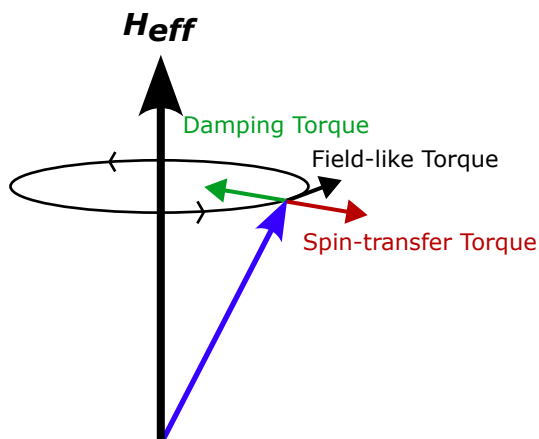


Figure 2.7: Torques acting on a magnetic moment (blue arrow) during magnetic field-driven precession.

where  $\mathbf{I}_s$  is the spin current,  $q$  is the elementary charge and  $N_s$  is the number of spins. Similar to the damping term this acts perpendicular to the direction of precession dependent upon the applied spin current. A schematic diagram representing all of the discussed torques acting on a magnetic moment is shown in Fig. 2.7.

In this way we can understand that disturbances to the magnetic state can be broken down into effective torques that act upon the magnetization and cause it to precess, driving the system's dynamics.

## 2.6 Summary

In this chapter, we have discussed the underlying physics necessary to understand this thesis. We have explained the origin of ferromagnetism and considered the origin of magnetic domains as satisfying a minimization of the demagnetization energy while balancing competition with anisotropy energy terms. We have introduced the dynamics of ferromagnetic materials by explaining the various terms of the LLGS equation that describes the precessional motion of magnetization in response to a magnetic field.

---

# CHAPTER 3

---

Experimental Methods



### 3.1 Introduction

In this chapter, we will introduce and explain the techniques used for the results presented in this thesis. We will explain the deposition techniques used in this thesis, and then detail the techniques which were used to characterize them both structurally and magnetically. Finally, we will describe the way in which micromagnetic simulations are performed in order to better explain the physics at play in the grown heterostructures.

### 3.2 DC Magnetron Sputtering

DC magnetron sputtering (“sputtering”) is a bottom-up means of growing a thin film of material from a bulk target by the ejection of ions, creating a vapour that coats the surface of the substrate. A thin film grown in this fashion can range anywhere from a few angstroms of material up to a few hundred nanometers.

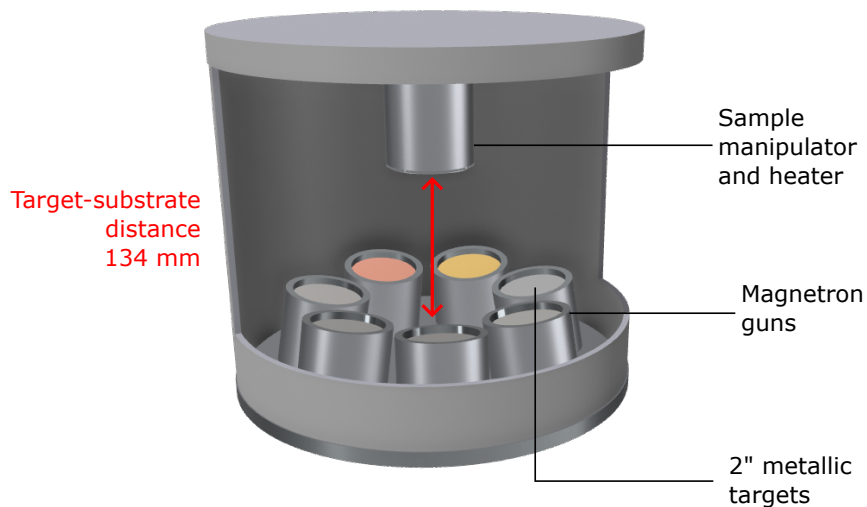


Figure 3.1: Schematic setup of the 7-target DC magnetron sputtering system used. Each magnetron gun is equally angled towards the substrate heater (top) such that each gun is, in theory, identical.

The system used consists of a 7 source chamber with the magnetron guns spread in a circle angled slightly towards the substrate-heater assembly suspended above, shown

## 3.2 DC Magnetron Sputtering

---

schematically in Fig. 3.1. The metallic target sits on the base of the magnetron gun below which there are strong permanent magnets that create a magnetic field pointing from the outer edge towards the centre of the target. A metallic case surrounds the outside of each gun with a separation distance of  $\sim 2$ mm.

To keep the main chamber at a good base pressure samples are first pumped down and outgassed in a smaller load lock chamber before being transferred into the main chamber. This limits the exposure of the main chamber to the atmosphere and importantly reduces the exposure to water which adsorbs strongly onto surfaces and requires a great deal of pumping time to remove, usually making up the greatest partial pressure fraction of most vacuum systems. Prior to growth, the entire chamber is held under a vacuum pressure of typically  $2 \times 10^{-8}$  mbar which is then improved to a pressure of  $2 \times 10^{-9}$  mbar by flowing liquid nitrogen around a Meissner trap, a coil of pipe that runs along the lining of the chamber which rapidly cools and condenses gases (most prominently water) along the surface of the chamber walls.

During growth an inert atmosphere of argon is introduced into the chamber with a flow rate of 10 sccm and a pressure of  $4.3 \times 10^{-3}$  mbar, reached by software control of an electronic gate valve position. A large potential difference on the order of 300 V is applied between the anode (the case) and the cathode (target) to ionize the argon into a glow discharge plasma that strikes the surface of the target material. The impact of the ions with the target displaces an initial set of atoms that collide with other atoms as they move further into the target and these secondary and tertiary collisions eject ions perpendicular to the sample surface which then constitutes the ionic vapour that is deposited onto the substrate.

The impact of these ions also creates secondary emission electrons which are confined by the magnetic field around the magnetron gun which locally increases the efficiency of plasma creation where the magnetic field is parallel to the target surface. This increase in efficiency allows this technique to achieve growth rates on the order of  $\sim 1 \text{ \AA}/\text{s}$  and creates a distinctive ‘racetrack’ around the target where the majority of sputtering occurs.

To ensure the growth is consistent samples are grown with a target-substrate separation of 134 mm and samples are constantly rotated at a speed of  $60^\circ/\text{s}$  to achieve uniform coverage of the film and offset the wedge effects of an angled deposition.

### 3.3 Pulsed Laser Deposition

Pulsed laser deposition (PLD) is a thin-film deposition technique making use of a high-fluence UV laser to evaporate a target material into a plasma that deposits the material onto the substrate. As a primary motivation, this technique differs from magnetron sputtering in the materials that the techniques are suitable for depositing. Sputtering in a DC mode is extremely good for metallic targets, but requires an RF source for the deposition of insulating materials which can reduce the growth rate and require more adaptation for epitaxial growth.

PLD is an alternative technique for growing insulating materials. The act of shining the laser onto the target material excites electrons within the material through a combination of inverse bremsstrahlung absorption and photoionization processes [95–97]. This rapidly ionizes the surface material creating a plasma that is in excellent agreement with the stoichiometry of the target [98]. Almost simultaneously, this evaporation of material creates an ensemble of atoms that are ejected from the target and form the deposition plume that is used to deposit material. This process requires no electrical contacts or threshold atmosphere to excite the plasma, meaning it can in principle be used on targets of any material and in practice is most commonly used in the deposition of oxide and insulating materials. This technique is commonly for growth of epitaxial thin films; single-phase crystalline thin films that exhibit only one crystal orientation chosen by the substrate.

The setup used is illustrated in Fig. 3.2. The substrate is mounted on a sample plate and is radiatively heated by the substrate heater a short distance above it, with the temperature controlled by a thermocouple attached to the heater assembly, but also tracked through a pyrometer aimed at the surface of the substrate. Targets are mounted onto a target carousel that can be rotated to switch between desired targets. A 248 nm KrF excimer laser is focused into the main chamber by a series of optics that serve to direct and focus the beam onto the target. The target is scanned along the  $x$  and  $y$  directions such that the focal point remains the same, with a rectangular spot size of  $0.94 \times 2.50$  mm, but the ablation position changes. A shutter sits between the substrate and target that can be opened or closed to control whether deposition is occurring and allow for the target to be ablated prior to deposition. In this setup, the laser is masked into a rectangular spot with a total area of  $2.36 \text{ mm}^2$  and this parameter is not changed. We assume that there is an 8% energy loss in the final window (quoted

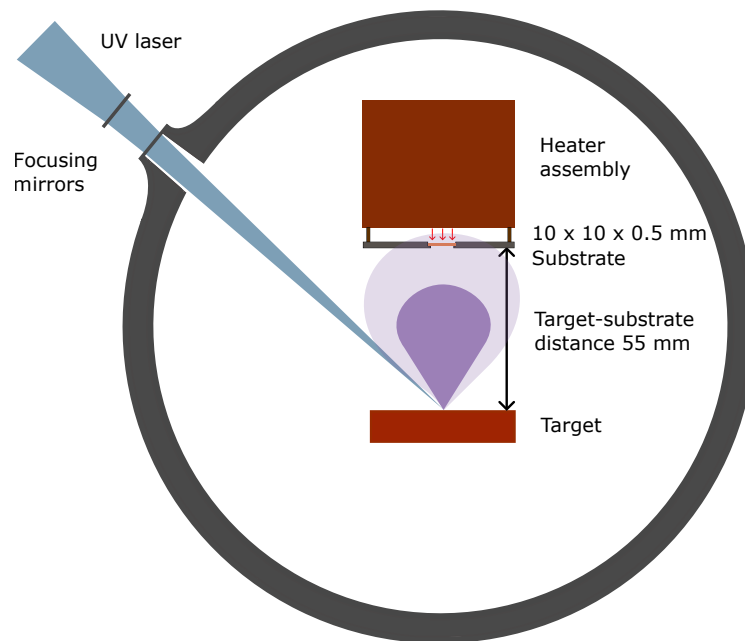


Figure 3.2: Schematic diagram of a pulsed laser deposition chamber. A series of mirrors direct the UV laser onto a focal point at the surface of the target, evaporating a plume of material that is deposited on the heated substrate.

in the specification of the equipment), which reduces the actual fluence on the target to  $f = 0.92 \times \frac{E}{A}$  where  $E$  is the energy prior to entering the chamber and  $A$  is the spot area. This is the calculation that will be used for deposition fluences.

There are many parameters that can be changed to affect the growth process. The primary deposition parameters are the substrate temperature and the laser fluence. Substrate temperature affects both the surface mobility of evaporated species that make their way onto the substrate (and consequently the surface formation process), as well as the preferred phase formation in complex materials such as perovskites. Laser fluence affects the plume dynamics, including the energy of the evaporated ions, growth rate, and can affect the stoichiometry and crystal structure of the film.

Added to this are the effects of the deposition pressure and target-substrate distance. In pulsed laser deposition, the oxygen pressure is large, typically on the order of 0.1 mbar, and a majority of the oxygen in oxide materials does not come from the target and instead is contributed by the atmosphere in the chamber - as shown in a study by Chen et al. [99] by using an isotope of oxygen as a growth gas. This means that the correct magnitude of oxygen pressure can be essential to form the desired phase, especially if there are a number of other oxide phases that can form. Added to this, the oxygen pressure has a direct effect on the plume dynamics, with larger pressures confining the plume significant. As such, the effects of changing this parameter can be difficult to predict. Similarly, changing the target-substrate distance affects the balance of other deposition parameters needed to obtain similar growth as this changes the energy of the atoms that land on the substrate and can require changing other deposition parameters to obtain the desired phase if changed. In this thesis, both the oxygen pressure and target-substrate distance remain fixed.

## 3.4 X-ray Characterization

X-rays are a useful tool for characterizing the structure of a material as they scatter and interfere non-destructively with matter allowing for the determination of sample parameters. We will focus only on two primary techniques: x-ray diffraction and x-ray reflectivity.

X-ray diffraction (XRD) is used to characterize the crystal structure of deposited films. This technique makes use of Bragg's law [100] to determine the spacing between lattice planes. Scans are performed in a  $2\theta - \omega$  setup in which the Cu  $K_\alpha$  X-ray

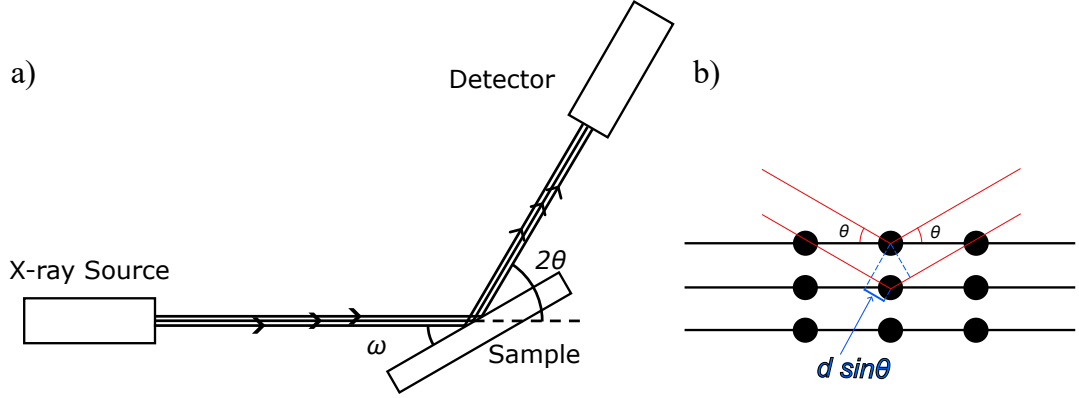


Figure 3.3: a)  $2\theta$ - $\omega$  setup for x-ray diffraction. b) Microscopic view of the Bragg diffraction at the sample surface.

source remains fixed and the sample and detector rotate to obtain the desired  $2\theta$  value, illustrated in Fig. 3.3a. When two beams with a path difference created by a diffraction grating interfere, they will interfere constructively only when the path difference (Fig. 3.3b) satisfies the relation:

$$n\lambda = 2d \sin \theta, \quad (3.1)$$

where  $n$  is an integer, representing the number of path length differences,  $\lambda$  is the wavelength of the x-ray,  $d$  is the periodicity of the diffraction grating and  $\theta$  is the angle at which the peak is observed. For crystalline materials, the diffraction grating is the lattice spacing between crystal planes and it is possible to determine this from the position of these Bragg peaks. With further information about the crystal structure, the lattice parameters can be extracted from the calculated lattice spacing.

Here  $\omega$  is not exactly  $\theta$  as it is used to compensate for any offsets by aligning to a well-defined substrate diffraction peak.

X-ray reflectivity (XRR) is used to determine film thickness and roughness. For X-rays, the refractive index of a material is, in general, complex and takes the form [101],

$$n = 1 - \delta + i\beta, \quad (3.2)$$

where  $n$  is the refractive index of the material,  $i\beta$  is the imaginary component of the refractive index which relates to the absorption of X-rays and  $\delta$  is a material-specific

parameter that describes the deviation of the refractive index from unity,

$$\delta = \frac{\lambda^2}{2\pi} r_o \rho_e, \quad (3.3)$$

with  $\lambda$  the X-ray wavelength,  $r_o$  the electron radius and  $\rho_e$  the electron density. This can be used to understand that there is a condition for which there will be external reflection of X-rays at low angles. From Snell's law,

$$\cos(\alpha) = n \cos(\alpha'), \quad (3.4)$$

a refractive index below unity leads to the condition of total external reflection, the angle for which can be estimated by taking  $\alpha' = 0$ ,  $\alpha = \alpha_c$ , the critical angle, and expanding  $\cos(\alpha_c)$  in a Taylor series:

$$\alpha_c = \sqrt{2\delta}. \quad (3.5)$$

This describes the origin of the reflectivity, but not the reflectometry patterns that would be experimentally obtained. The simplest case is for that of a thin film on a substrate. In this scenario, the sample has multiple interfaces at which the electron density changes; from the substrate to the film, and from the film to air. The intensity of a single interface can be described by calculating, for each angle with the boundary condition of the incident and exit angles being equivalent, a Fresnel reflectivity,

$$r = \frac{k_z - k'_z}{k_z + k'_z}, \quad (3.6)$$

where  $r$  is the Fresnel reflection coefficient,  $k_z$  is the incident wavevector and  $k'_z$  is the reflected wavevector. The reflectivity is then related to the reflectivity intensity by  $R = |r|^2$ . This describes the case of a perfectly smooth interface, an ideal substrate with no roughness. To calculate the reflectivity of a thin film every means of reflectivity must be considered; an initial reflection off the surface, transmission through the film followed by reflection from the substrate and transmission into the air, and the infinite higher-order series of reflections between the substrate and film that result in transmission back into the air after  $n$  bounces.

The simplified result of this is then a reflectivity of the form,

$$r_{slab} = \frac{r_{01} + r_{12}p^2}{1 + r_{01}^2 p^2}, \quad (3.7)$$

where  $r_{slab}$  is the total reflectivity of the slab,  $r_{01}$  is the reflectivity at film-to-air interface,  $r_{12}$  is the reflectivity at the film-to-substrate interface, and  $p$  is a phase factor that results from the additional distance traversed by the higher-order reflections of the X-ray,  $p^2 = e^{iQ\Delta}$  where  $\Delta$  is the film thickness. This additional phase factor is the origin of Kiessig fringes [102] in the reflectivity curve, with the oscillations relating to the in or out of phase nature of the interfering waves. This dependence of the oscillatory behaviour on the film thickness allows for information about film thickness to be extracted from XRR data.

In practice this describes the most basic case of a thin film on a substrate. The introduction of interface roughness and additional interfaces requires more complex analysis and fitting programs. In this thesis, the program GenX [103] is used to fit x-ray reflectivity data. In this program, a sample is defined by building up a set of thin film layers on top of a substrate with material parameters corresponding to the layer being simulated. These include the initial guess of the film thickness and roughness, and a scattering length density that describes the interaction of X-rays with the electron density. At each interface the magnitude of this scattering length density changes with a roughness characteristic of this interface, modelled as a Gaussian distribution. From this SLD profile of the sample a reflectivity curve is simulated using the Parrat [104] recursion formula, a method of calculating all of the possible reflection amplitudes.

From an initial simulated curve, the software can improve the fit to the data using a differential evolution algorithm in which individual parameters are changed within user-defined bounds, the new curve is simulated, and a figure of merit is calculated to determine if the change is better or worse than the previous simulation and the parameters that fit to the data best are retained. After a suitable number of iterations dependent upon the problem, this will obtain the best fit to the data within the model defined and the bounds given. There are however a large number of free parameters in these fitting models and so care must be taken to ensure the model is not more complex than it needs to be and that the final fit makes sense.

### 3.5 Polarized Neutron Reflectometry

The magnetic profile of a thin film can be probed by the use of polarized neutron reflectometry (PNR). In the same manner as with x-rays, at low angles there is a total external reflection resulting from the difference in refractive index dependent upon the



### 3.5 Polarized Neutron Reflectometry

---

combined nuclear scattering length density,  $\rho$ ,

$$n = 1 - \frac{\lambda^2}{2\pi} \rho + i\beta, \quad (3.8)$$

with  $n$  the neutron refractive index,  $\lambda$  the de Broglie wavelength of the neutron,  $i\beta$  an absorption term [105].

In neutron reflectometry there are two sources of scattering to consider: scattering due to the neutron-matter interaction between the neutrons and the atomic nuclei, and the magnetic scattering from the dipolar interaction between the neutrons and the magnetic  $\underline{B}$  field of the sample. In the absence of a magnetic field, the patterns contain the same information as can be obtained from XRR with the advantage of enhanced nuclear sensitivity. The interaction of the neutrons with the magnetic field results in a potential of the form,

$$V = -\underline{\mu} \cdot \underline{B}, \quad (3.9)$$

where  $\underline{\mu}$  is the magnetic dipole moment of the incident neutrons. The consequence of this is that the magnetic component of the SLD is then also dependent upon the dot product of the neutron moment with the magnetic field of the sample,

$$b = b_{nuclear} \pm b_{magnetic}, \quad (3.10)$$

where  $b$  is the total coherent neutron scattering length. The resulting reflectivity curve will then depend on the polarization of the neutron relative to the magnetic field of the sample, and so measurements aiming to probe the magnetic character of a sample must measure with both polarization of neutrons to obtain the full reflectivity profile. The advantage of this technique with regards to measuring magnetic properties is that the obtain reflectivity curves are depth (and equivalently, layer) dependent allowing for measurement of properties nested below the surface of multilayer structures or of magnetic structures that vary through the thickness of the sample.

The experimental setup is similar to that of x-ray reflectivity. Prior to the neutron beam interacting with the sample, the beam can be polarized into either an ‘up’ or ‘down’ beam relative to the applied magnetic field direction on the sample. This is achieved using a combination of polarizing mirrors that reflect ‘up’ and ‘down’ neutrons in different directions, one on the incident side of the setup and one on the reflected side. This allows for neutron polarization to be selected for twice, controlling the

### 3.6 Reflection High-energy Electron Diffraction

---

incident polarization and the reflected polarization measured, which is critical as there is the possibility for spin-flip scattering in which the neutron polarization changes over the course of the experiment. This allows for effectively four types of polarization scattering: non-spin flip scattering,  $R^{++}$  and  $R^{--}$ , and spin-flip scattering  $R^{+-}$  and  $R^{-+}$ .

These two types of scattering are relevant for different measurements. Non-spin flip scattering is sensitive to both the nuclear scattering and the magnetic scattering of the sample that is in the direction of the applied magnetic field. Spin flip scattering is sensitive only to the magnetic scattering of the sample, and only perpendicular to the direction of the applied magnetic field [106]. In this thesis, only the non-spin flip geometry will be used.

Analysis of PNR data is performed using Refl1D [107]. This program works similarly to GenX as described in the previous section, with a sample being defined in a similar way now including a magnetic component of the nuclear scattering, but it uses a Markov chain Monte Carlo method to sample the parameter space alongside a differential evolution algorithm. This allows it to more effectively explore a wide parameter space and be much less reliant on initial guess parameters, effectively overcoming local minimums independently with the downside of being more computationally expensive. The uncertainty in fitting parameters obtained in this way can be determined using Bayesian analysis to estimate the confidence of the final parameters obtained.

### 3.6 Reflection High-energy Electron Diffraction

Reflection high-energy electron diffraction (RHEED) is a surface-sensitive technique in which electrons are diffracted off of the surface of the sample at acute angles, typically less than  $5^\circ$ . Electrons are excited from a filament and accelerated towards the sample material by a high voltage (on the order of 20 kV) and focused using electromagnetic optics to control the beam. The electrons interfere and are diffracted (in a manner similar to x-rays discussed previously) off of the sample surface and the resulting pattern is dominated by the surface features since there is a very low probability that the electrons penetrate into the sample and are then reflected. Different to the x-ray experiments mentioned previously, the detector used in this experiment is a phosphorescent screen that is imaged using a camera. As a result this technique directly images the reciprocal  $k$ -space of the electron scattering.

### 3.6 Reflection High-energy Electron Diffraction

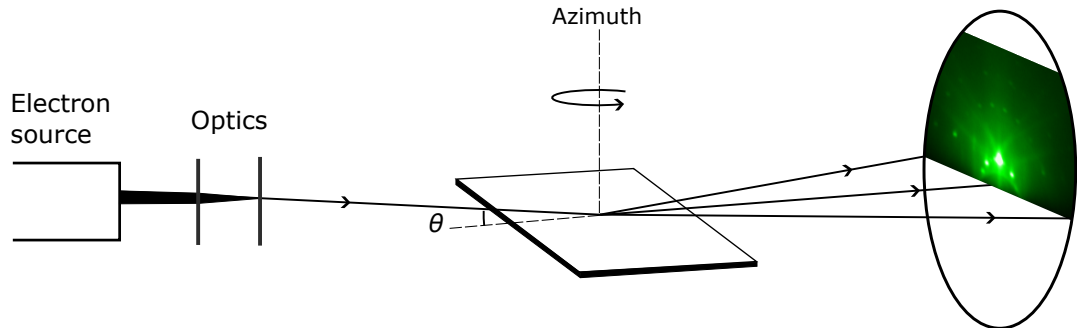


Figure 3.4: Schematic diagram of a RHEED setup, with the sample surface face up. Electrons are focused at a shallow angle onto the surface of the sample and the resulting 2D diffraction pattern is detected through a phosphorous screen. The pattern shown here is for a  $\text{SrTiO}_3(100)$  substrate (not to scale).

To understand the effects of surface features on the resulting pattern it is useful to visualise the feature first in reciprocal space. Several features are shown in Fig. 3.5 as examples. Starting from the simplest surface, a completely flat single crystal can be represented as a series of diffraction rods in reciprocal space. To reconstruct the resulting RHEED pattern the Ewald sphere [108] is drawn through the rods and a pattern of 3 spots in an arc can be obtained. This corresponds to Bragg diffraction off adjacent atoms and an ideal pattern like this is generally expected for single-crystal substrates. The spacing between the spots along the Ewald sphere relates to the lattice parameters and the crystal axis along which the electrons are incident, and so it is possible from ideal patterns such as this to obtain information about the crystal structure at the surface. Usually, this involves some measurement of spacing between spots relative to a substrate pattern or buffer layer pattern and additional measurements performed *ex situ* to verify these measurements [109].

Also common in epitaxial growth is the emergence of streaks. These result from small domains on the surface of the film, typically grains or islands that occur during thin film growth, which broaden the reciprocal rod and leads to a streak feature with a width and length dependent upon the size of the surface domains.

Satellite spots (and streaks) result from atomic terraces within the surface of the film. Resulting from the additional atomic step between the two surface levels, there is an additional Bragg condition where electrons can interfere constructively or de-

### 3.6 Reflection High-energy Electron Diffraction

---

structively. In reciprocal space this creates additional rods with spacing related to the terrace spacing and there is a resulting RHEED intensity related to the proportion of each level.

A rough substrate or film can be represented as a multilevel stepped surface. This surface is essentially a combination of the previous two scenarios and combines the broadening of lattice rods with the additional Bragg condition to allow streaks that vary in intensity related to the intensity of the additional Bragg condition.

For 3D islands, the resulting pattern is effectively a result of transmission through the islands rather than reflection off the surface. The pattern is then a transmission diffraction pattern. These patterns are exceptionally difficult to interpret, and irregular transmission patterns can be indicative of other factors such as contamination on the surface or a highly disordered surface. Knowledge of these features is useful in the verification of substrate and film quality and in diagnosing issues with growth.

Not shown in these diagrams is the effect of inelastic scattering. Unlike x-rays, there is a high probability of the electron losing energy while interacting with the sample surface and losing momentum. The effect of this is the emergence of Kikuchi lines, visible in the pattern shown in Fig. 3.4, which form bands that connect Bragg diffraction spots and are indicative of good surface ordering.

Due to the technique using electrons, the entire apparatus must operate under a vacuum. For this reason, most setups are designed to operate as an in-situ technique for a vacuum deposition system such as a PLD chamber. Based on the understanding we have explained so far, this initially makes it a good technique for verifying substrate quality at all steps prior to growth and for measuring immediate film quality after growth. From this alone, it serves as an excellent diagnostic tool purely by operating in situ.

However, the system can operate at higher base pressures if the main electron source is differentially pumped to maintain a lower pressure than the main growth chamber. The benefit of this is that we can obtain information about the surface of the substrate as the film is in the process of being deposited. Tracking the intensity of diffraction spots in a well-aligned RHEED pattern retrieves information about the surface roughness over time, with rough surfaces reducing the intensity of the spot and smooth surfaces increasing it. In a 2D growth mode, this directly corresponds to the layer formation process in which a completed layer is perfectly smooth and growth of

### 3.6 Reflection High-energy Electron Diffraction

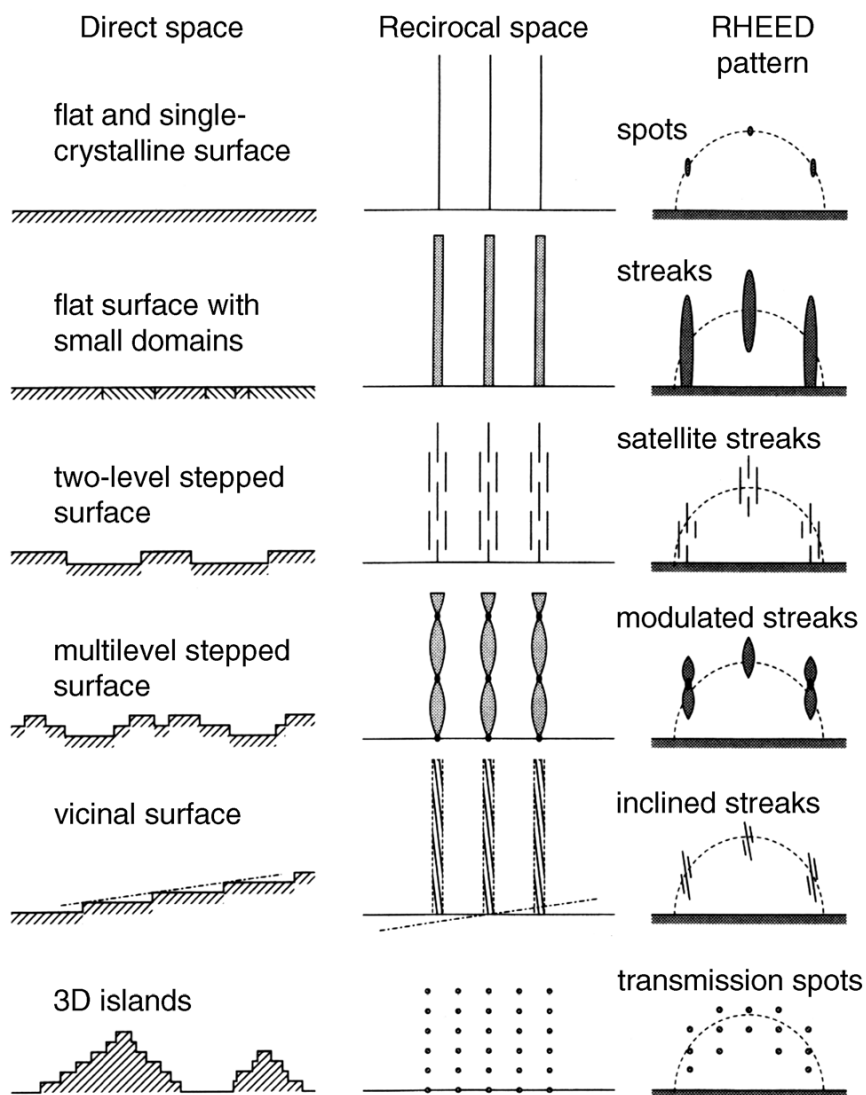


Figure 3.5: Expected RHEED patterns for various surface features shown in steps; the feature as it appears in real space, the reciprocal space equivalent, and the resulting pattern obtained by intersecting a Ewald sphere with the reciprocal pattern. Figure reproduced from Ref. [110].

a new layer increases the roughness. Tracking this over time can produce oscillations that correspond to the growth rate of new layers of material.

### 3.7 Kerr Magnetometry & Wide-field Microscopy

Magneto-optic effects are extremely useful for probing the magnetic behaviour of a sample non-destructively, particularly in the case of thin films where moments can be quite small. There are two methods by which the magnetic state can be probed optically: the Faraday effect, in which polarized light is rotated while travelling through a magnetic field, and the Kerr effect in which polarized light is rotated upon being reflected by a magnetic material [111]. These correspond to transmission and reflection measurements respectively and for thin film materials the Kerr effect is generally the most useful and the only one that will be discussed in detail.

The origin of the Kerr effect is an effect known as magnetic circular dichroism. Consider a magnetic material in a purely saturated state. The material has a net magnetization and can be described by a mean free field, and there will be a spin-orbit interaction between electrons and this field that splits the energy levels of the electrons. When circularly polarized light is incident on the material it causes electrical charge to rotate which generates a magnetic field that can be either aligned with the magnetic field or against it. The effect then is that the circular components of light become birefringent with the difference in the refractive indices leading to a phase-lag between the two circularly polarized components of light. For a linearly polarized light source, this results in a conversion of linearly polarized light into elliptically polarized light, with the major axis of the elliptically polarized light rotated from the axis of the initial linearly polarized light.

The basic setup of a magneto-optic Kerr effect (MOKE) experiment is shown in Fig. 3.6. A polarized light source is directed at the magnetic sample and reflected through a polarizer with a perpendicular orientation to the initial beam. With no magnetic field, or in a non-magnetic sample, the light will remain in the original polarization which would result in zero signal for perfectly polarized light in 100% efficient polarizers, and realistically no significant change in the signal at a detector under an applied magnetic field. With a magnetic material, the light will be rotated by an amount relative to the magnetization of the sample which will rotate the polarized angle away from the initial position resulting in a larger signal. By setting up the polarizers close

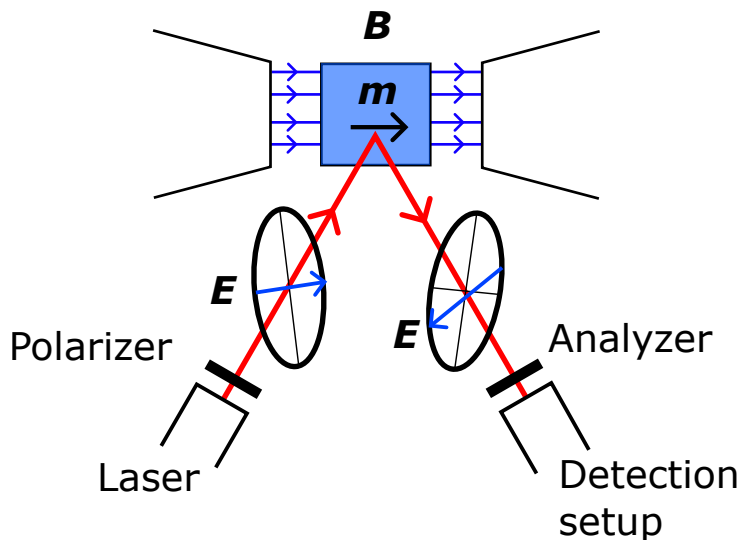


Figure 3.6: Schematic diagram of a laser MOKE setup. A polarized laser incident on a material with a magnetic moment experiences some rotation of the polarization angle, measured after a cross-polarized analyzer.

to extinction, we can reduce the output signal by rotating the polarization closer to extinction and increase the signal by rotating it further away allowing us to track the magnetic behaviour under an applied field.

When considering MOKE experiments performed in this way, there are three geometries that relate to different effects that can be measured. The geometry shown in Fig. 3.6 describes the longitudinal Kerr effect: in-plane component of the scattering plane of the light is parallel to the applied magnetic field, and so contrast is sensitive to changes in the magnetization along this direction. If the magnetic field was rotated by  $90^\circ$  such that the field and scattering plane are perpendicular, the resulting signal would be sensitive only to changes perpendicular to the applied magnetic field and this describes the transverse Kerr effect.

For tracking the sample-wide behaviour only a 1D detector is required. With a 2D detector, a camera CCD, we can also track the magnetic behaviour at various points within the sample corresponding to each pixel of the detector. This can be used to obtain images of the magnetic microstructure, that is the magnetic domains within the sample. A typical MOKE microscopy setup is shown in Fig. 3.7. Instead of using a laser

### 3.7 Kerr Magnetometry & Wide-field Microscopy

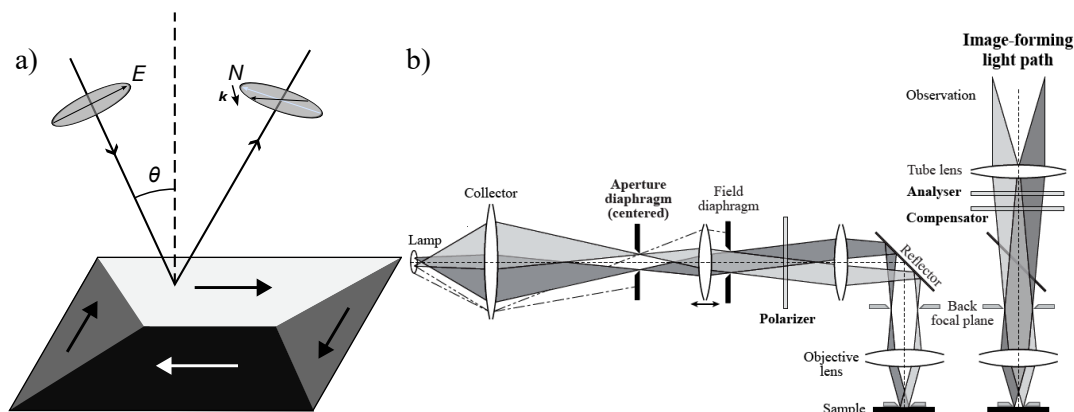


Figure 3.7: a) Wide-field Kerr microscopy illustrated for an in-plane flux closure domain. The lens focuses the beam path onto microscopic parts of the sample and the incident polarized light,  $\mathbf{E}$ , is rotated by a vector  $\mathbf{k}$  away from the initial reflected position,  $\mathbf{N}$ , allowing for contrast to be obtained on the other side of an analyzer. Magnetization direction within a domain is indicated by the arrows. b) Schematic diagram of the beam path that the light follows (reproduced from Ref. [112]).

source, a white light source is used and focused through a lens onto the sample. The light is polarized close to parallel to the sample surface and rotated by the Kerr effect as explained above and reflects light with some elliptical polarization. The reflected light is then passed to the back focal plane through a compensator which linearizes the incoming light, and then an analyzer which acts as a cross-polarizer to select out magneto-optic contrast. The camera outputs the final signal as a greyscale image.

By itself, the contrast obtained from the Kerr effect is fairly weak and would restrict this imaging to only materials with a particularly high magnetic moment. However, we can enhance the contrast using post-processing techniques. In a saturated state free of domains a background image is obtained; in this state the change in light levels should correspond only to changes in magnetic behaviour. From each image, we subtract this background which restricts the resulting contrast to only changes in magnetic character.

Contrast is selected by the angle of incoming light relative to the sample surface. Under uniform illumination, a 2D detector has an extinction cross rather than a single extinction point shown in Fig. 3.8. The bands of this cross correspond to light incident on the sample at different angles and so can select out different regions of contrast.



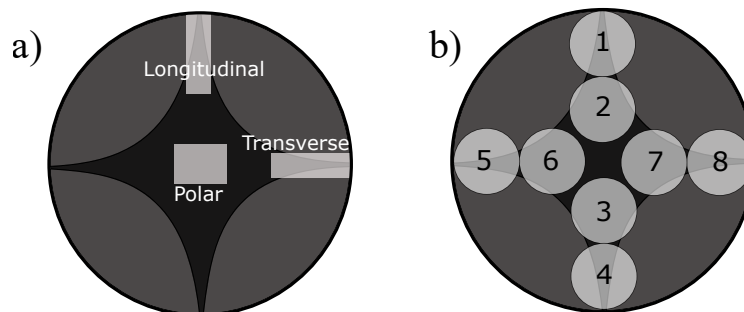


Figure 3.8: a) Extinction cross obtained on the back focal plane. Highlighted are the three regions corresponding to the three standard contrast directions. b) Position of LEDs within the extinction cross which can be illuminated selectively to highlight contrast regions from a).

The central extinction region corresponds to light that is reflected at or close to normal incidence to the sample and obtains out-of-plane (polar) contrast. The sample is illuminated by 4 pairs of LEDs with two leds illuminating each ‘arm’ of the extinction cross making it possible to rapidly swap between different contrast directions by toggling active LEDs [113]. This is useful to obtain vector images of magnetization direction by rapidly switching between transverse and longitudinal contrast, or to enhance the contrast through further image subtraction between opposing pairs (e.g. top and bottom) [114]. In this LED configuration, the polar signal is obtained by any of the inner ring of LEDs in opposing pairs (such as 2 and 3) to maximise the polar signal while cancelling any in-plane signal, and as such the opposing LEDs have to be equalised to ensure this remains the case.

#### 3.7.1 Imaging Ferroelectric Domains

This technique of using taking advantage of changes in refractive indices to measure contrast using polarized light is extensible to other sources of birefringence. Relevant to this thesis is the imaging of ferroelectric domain structures on the microscale. In ferroelectric crystals, as discussed previously, the axes of the crystal unit cell are elongated leading to short and long axes with differing refractive indices. Imaging a crystal with polarized light then, through a similar experimental setup as for the Kerr effect, can introduce a phase lag that results in a signal dependent on the orientation of light

relative to the orientation of the crystal. Imaging across ferroelectric domains it is then possible to pick up a contrast between the two domain structures if they are oriented at different angles to the incident plane of the polarized light. The contrast resulting from this can be many times greater than for the ferromagnetic domains and does not typically need subtraction techniques to enhance the contrast.

Imaging on a bare ferroelectric substrate this crystal birefringence will be the only source of contrast. However it is typically possible to image through a thin metallic film on the surface of a BaTiO<sub>3</sub> substrate as the substrate is transparent. It is then possible to pick up some ferroelectric contrast and ferromagnetic contrast simultaneously. This is typically not a concern for magnetic imaging: these techniques use a post-processing subtraction technique to eliminate any static background, so any contribution will be purely due to mechanical drift. For ferroelectric imaging of these samples, one has to be sure that there is no Kerr contrast. This involves adjusting the polarizer-analyzer setup such that there is no significant change in overall light level under an applied magnetic field, and that a ‘magnetic domain’ image taken via a subtraction technique is pure noise. It can then be said that the unsubtracted image will display contrast purely due to the ferroelectric domains.

### 3.8 XMCD-PEEM

For higher resolution magnetic imaging we use x-ray circular magnetic dichroism (XMCD) combined with photo-emission electron microscopy (PEEM). In Kerr microscopy experiments the resolution is limited according to the Rayleigh diffraction limit,

$$\theta = 1.22\lambda/D, \tag{3.11}$$

which represents the smallest angular resolution,  $\theta$ , that is possible for a wavelength of light  $\lambda$  through an aperture size  $D$ . Below this resolution, features become indistinguishable from each other.

A higher resolution can be obtained then by using high-energy x-rays or electrons that allow us to reduce this resolution an image nanoscale features with more certainty. In XMCD-PEEM, the imaging element comes from photoemission electrons and so the resolution is limited by the photoemission electron microscope resolution.

The x-rays act as an element-specific illumination source. The X-ray absorption spectrum is element-specific, and so the magnetic sensitivity can be tuned to specific

elements (e.g. Fe or Co) by selecting the illumination X-ray energy that corresponds to the absorption edge of that element [115]. Contrast is then obtained by the difference in magnetic circular dichroism. The magnetic dichroism works much the same as in Kerr microscopy, with left and right circular polarizations of x-ray being absorbed (rather than refracted) in differing amounts dependent upon the orientation of the magnetic state to the applied orientation of polarization. The sample will typically be illuminated twice with opposing orientations of circular polarization and the two images will be subtracted to obtain a magnetic contrast image. This post-processing removes any non-XMCD signal.

The absorption of X-rays stimulates the emission of secondary photo-electrons which can then be focused by typical electron microscope optics onto a detector. The intensity of electrons detected then becomes the signal in this technique, with regions where the X-rays are more strongly absorbed stimulating more electron emission leading to a bigger signal. The combination of these two allows us to use this technique for higher resolution magnetic domain imaging than could be obtained by Kerr microscopy, with the added ability to select for elemental sensitivity. The resolution of this technique is limited primarily by the focusing optics and the spherical and chromatic aberration effects introduced by them, but resolutions are typically quoted as being on the order of 20 nm [116].

### 3.9 SQUID-VSM Magnetometry

Measurements of the absolute magnetic moment of samples are performed using a vibrating sample magnetometry (VSM) technique. The advantage of this technique is that the saturation magnetization of the sample can be obtained quantitatively with a high resolution that is necessary for thin film systems, as opposed to an inferred signal such as can be obtained in MOKE techniques which cannot generally be used to calculate the saturation magnetization. Additionally, the temperature of the sample space can be controlled by the use of a heater and cryogens to measure the response of a sample at different temperatures.

The sample is placed inside a pair of pick-up coils under a weak vacuum and vibrated at a fixed frequency. The vibration of the sample creates a change in magnetic flux that induces a current in the coils proportional to the magnetization of the sample which is picked up as a signal. A magnetic field is applied by a superconducting magnet allowing

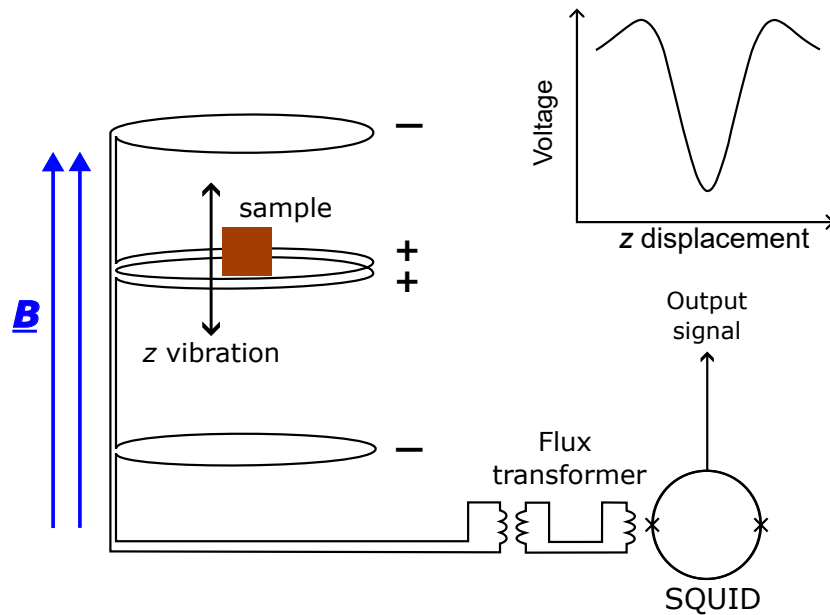


Figure 3.9: Schematic diagram of a SQUID-VSM Magnetometer. The sample sits between the pickup coils and vibrates along the  $z$  axis, producing a current that is converted via the flux transformer and SQUID circuit into an output voltage. An example response function is sketched in the top right.

for fields up to 7 T.

The arrangement of the pick-up coils is chosen such that they act as a second-order gradiometer, meaning that it is sensitive to the second derivative of the magnetic field  $\partial^2 B_z / \partial^2 x$  only, removing any contributions from uniform magnetic fields and linear field gradients. A simple schematic view of this setup is shown in Fig. 3.9. The magnetic moment is calculated by assuming that the sample acts as a magnetic dipole. The response of a magnetic dipole as it moves through the pick-up coils, shown in the top right of Fig. 3.9, is non-linear and can be fit to a response function to obtain the dipole magnetic moment.

A superconducting quantum interference device (SQUID) converts the induced current into a voltage which can then be amplified. The SQUID component is used as it has a very high resolution of one flux quantum,  $\phi_0 = \frac{h}{2e}$  [117], intrinsic to the design of the device. Combined with lock-in amplifiers set to the frequency of the sample vibration, this allows for a high resolution signal which results only from the sample.

Performing hysteresis loops in this setup includes non-ferromagnetic contributions

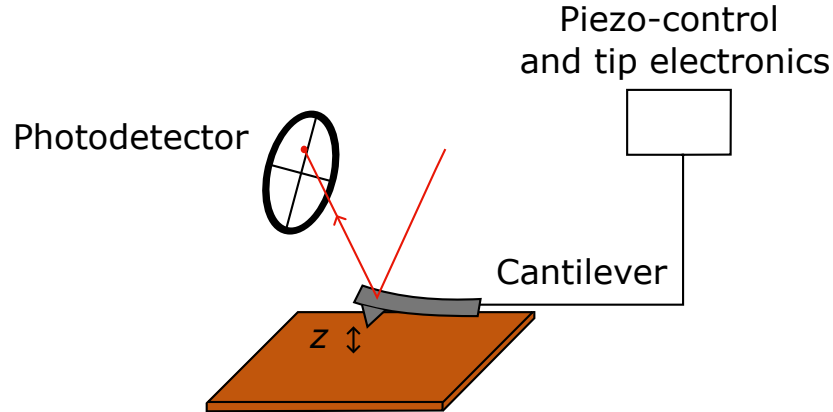


Figure 3.10: Schematic atomic force microscopy setup. The cantilever is brought close to the sample and experiences tip-surface interactions that deflect the laser and produce an output signal. Tip oscillation and height are controlled by piezoelectric motors.

from material in the space - the sample holder and the sample stick being the main contributors. These materials are either diamagnetic or paramagnetic and contribute a linear background which can be subtracted as a linear fit from the loops. The resulting hysteresis loop with this background subtracted then has a saturation moment that is used to calculate the saturation magnetization of the sample.

### 3.10 Atomic Force Microscopy

Atomic force microscopy (AFM) is used to investigate surface topography. The instrument used was a Bruker Multimode 8 AFM.

When an atomically sharp AFM tip attached to the end of a cantilever is brought into contact with the surface of a sample, the tip interacts with the surface and is displaced from the initial position. In the simplest case, illustrated in Fig. 3.10, the tip interacts repulsively and is deflected away from the surface. The deflection of the cantilever can be tracked optically using a laser focused on the centre of the tip. The laser is reflected onto a 4-quadrant photodetector which measures the position of the laser as a voltage based on the difference in signals between the quadrants. When the tip is deflected, the laser is moved and the change in height can be measured by the change in photodetector voltage.

The interaction force on the tip is depends on the distance between the tip and the sample as shown in Fig. 3.11. From this two regimes can be defined on either side of the force minima; the contact regime in which the tip is repulsed from the surface and the non-contact regime in which the tip is attracted [118]. Both regions are equally valid routes to attaining surface information, and the choice of which regime to use is dependent on the requirements of the experiment and modified techniques such as magnetic force microscopy or piezoresponse force microscopy.

The experiments in this thesis use an intermittent contact (‘tapping’) mode. As the cantilever behaves as a stiff spring, its motion in response to an applied force is well described by a simple harmonic oscillator and it has a resonant frequency dependent upon the specific materials used to make the cantilever. If the cantilever is driven by a sinusoidal force at the resonant frequency, it will undergo oscillatory motion with an amplitude that is maximised at this frequency. This driven harmonic motion has the general form,

$$\frac{d^2z}{dt^2} + \beta \frac{dz}{dt} + \omega_0^2 z = A \cos(\omega t), \quad (3.12)$$

where  $z$  is the displacement of the cantilever,  $\beta$  is the damping parameter,  $\omega_0$  is the resonant frequency of the cantilever, and  $A \cos(\omega t)$  is the driving force.

When the tip is then lowered into contact with the surface of the sample additional interactions are introduced that change the resonant frequency of the oscillating cantilever. This results in a drop in the amplitude that the cantilever is currently oscillating at, signalling that the cantilever is “in contact” with the surface. When the cantilever is in contact in this way, the amplitude of the oscillation is very sensitive to small changes in the  $z$ -position. To measure the deflection across the sample a feedback loop is used to keep the amplitude of the oscillation constant with the  $z$ -piezoelectric motors adjusting the tip height to maintain a constant amplitude. The change in the position of the piezoelectric motor is then recorded and used to determine the deflection of the tip from the surface.

### 3.11 Micromagnetic Simulation

Simulations of magnetic materials are performed using the micromagnetic package MuMax3 [120].

The program implements a finite discretization method, meaning that the entire

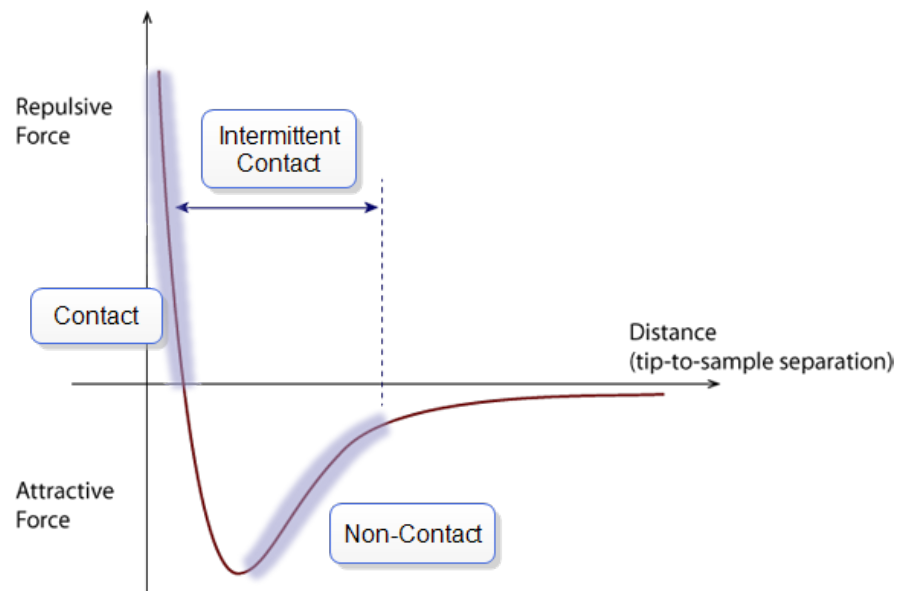


Figure 3.11: Force-distance diagram for AFM tip-sample interactions. Shown are the regimes corresponding to the contact and non-contact modes. Figure reproduced from Ref. [119].

simulation is broken into smaller cells defined by the user. Cell sizes are typically on the order of a few nanometers. The simulation space is then defined by the number of cells in each of the  $x$ ,  $y$  and  $z$  directions to obtain the desired simulation volume. Each cell has constant magnetization. The simulation geometry is, by default, cuboidal but can be defined to be various shapes; only a cuboid geometry will be used in this thesis. Periodic boundary conditions can be set to define the number of repetitions in the  $x$ ,  $y$  and  $z$  directions. At the onset of the simulation, the magnetostatic interactions are calculated numerically from the initialized geometry and periodic boundary conditions to determine the demagnetizing field.

Cells can be assigned to regions specifying the material parameters relevant to the magnetic behaviour of a simulated material: Saturation magnetization ( $M_{sat}$ ), exchange stiffness ( $A_{ex}$ ), the damping parameter ( $\alpha$ ), and the uniaxial anisotropy constant ( $K_{u1}$ ) among others that relate to modules which will not be used in the course of this thesis. This allows the material properties to vary spatially within the simulation dependent on how the user has defined things; in our simulations, we will often describe regions in which the director of  $K_{u1}$  changes. This is done by first defining a region as a range of  $x$ , and then explicitly setting the micromagnetic parameters of that region as desired.

The effect of magnetic interactions, such as exchange and the Dzyaloshinskii-Moriya interaction, are included by the calculation of an effective field term at each cell which is then used to calculate the effective energy density of an interaction. These effective field terms are then used to calculate the effective field term in the Landau-Lifshitz equation, which is solved using the Runge-Kutta method of numerically solving differential equations to obtain an effective torque on each unit cell. The simulation can then be run for either a set time, after which point it will stop, or until the system has effectively relaxed defined by the effective torque falling below a threshold ‘*MaxErr*’ parameter.

With parameters corresponding to the material (obtained experimentally), it is possible to model the magnetostatics and domain structure of magnetic thin films by calculating the torque resulting on each micromagnetic cell, which results from a Landau-Lifshitz torque encompassing intrinsic (exchange, Dzyaloshinskii-Moriya, magnetostatic, etc) and magnetic field interactions, and the Slonczewski [94] and Zhang-Li [121] torques that relate to spin transfer induced by electrical currents. This micro-



### **3.11 Micromagnetic Simulation**

---

magnetic method is a powerful tool to extend experimental measurements and aid in the interpretation of results.

---

# CHAPTER 4

---

Pattern Transfer in BaTiO<sub>3</sub>(111)/CoFeB Films

## 4.1 Introduction

In this chapter, I describe the work done to investigate the domain pattern transfer of a BaTiO<sub>3</sub> (BTO) (111)-oriented substrate onto a CoFeB thin film which is coupled via strain at the interface. Results are presented in the room-temperature tetragonal phase of the BTO substrate and focus on the changes in the ferromagnetic properties. In these heterostructures, the ferromagnetic domains are strongly coupled to the ferroelectric domains as a result of the large strain associated with the ferroelectric order which imprints a magnetostrictive anisotropy.

As the ferroelectric substrate has domain structure and the polarization changes orientation across ferroelectric domains, this means that the imprinted anisotropy has domain structure and at each ferroelectric domain wall the anisotropy will rotate between domains. The magnetization is strongly pinned to the axis of magnetoelastic anisotropy, leading to either head-to-tail domain walls or head-to-head charged magnetic domain walls [122] in which the magnetization points into the domain wall from both sides at non-180° angles. The change in orientation of these magnetoelastic anisotropy directors leads to a reduction in the angle by which the magnetization rotates within a domain wall, reduced from the 180° rotation of a typical domain wall to instead the angle between the adjacent magnetoelastic anisotropy directors.

This chapter details the effects of strain-coupling between (111)-oriented BaTiO<sub>3</sub> substrates and sputtered CoFeB thin films. On this cut of the substrate, the rotation of polarization between adjacent ferroelectric domains will be either 60° or 120° which will in turn be reflected in the rotation of the imprinted magnetoelastic anisotropy axes. Wide-field Kerr microscopy was used to study the imprinted domain structure which consists of two components: elastic pinning of ferromagnetic domain walls to ferroelectric domain walls and a transfer of local anisotropy dependent upon the polarization direction within the stripe domain. The former effect gives rise to magnetic stripe domains and is responsible for the pattern transfer that are observed. The effect of the latter is very dependent upon the two strain states that are imprinted from these substrates, leading to differences in the reversal domain patterns and changes in the magnetic field response of the magnetic domain wall width.

This chapter is adapted from work reported in Ref. [123] which details the work attributable to the author. XMCD-PEEM imaging was performed on the I06 beamline at Diamond Light Source with the assistance of D. Backes and F. Maccherozzi.

## 4.2 The Tetragonal Phase

At room temperature, the crystal structure of barium titanate belongs to the  $P4mm$  crystal space group which is tetragonal. In this phase, the lattice parameters are elongated along the  $\langle 100 \rangle$  directions, leading to 3 equally likely orientations that twinning domains can form along. In this phase, the Ti atom in the typical perovskite unit cell is displaced from its central position along the direction of lattice elongation and is the primary driving force of the polar properties in this phase.

The ferroelectric domain structure in this phase corresponds to ferroelastic switching between the equivalent  $\langle 100 \rangle$  orientations of lattice elongation/polarization. This manifests usually as long stripes of one orientation adjacent to a stripe of another repeated many times over one grain orientation. For a substrate cut along the (111) plane, the polarization directions have to be projected onto the (111) plane to understand the behaviour that will be observed in these domains. The component of a vector lying in a plane can be found by subtracting the component lying normal to the plane - that is:

$$p_{proj}^{\vec{}} = \vec{p} - \left( \frac{\vec{p} \cdot \vec{n}}{(|n|)^2} \right) \cdot \vec{n} = \begin{pmatrix} 1 \\ 0 \\ 0 \end{pmatrix} - \frac{1}{3} \cdot \begin{pmatrix} 1 \\ 1 \\ 1 \end{pmatrix} = \begin{pmatrix} 2/3 \\ -1/3 \\ -1/3 \end{pmatrix}, \quad (4.1)$$

which results in 3 equivalent directors from the  $\langle 11\bar{2} \rangle$  projections of polarization in the (111) plane.

BaTiO<sub>3</sub> has domain structure where the polarization can ferroelastically switch between the equivalent polarization directions. On a (100) surface, these result in either 90° or 180° domain walls. If these directions of polarization are projected onto the (111) surface then there are three equivalent directions  $t_1$ ,  $t_2$ , and  $t_3$  separated by 60°. To switch between, for instance,  $t_1$  and  $t_2$  the polarization can rotate through either 60° or 120° giving two distinct types of domain structure as illustrated in Figure 4.1.

There are several facts that can be understood from this that will be useful for later experiments. If we label the configurations of ferroelectric domain structure by the angle that the polarization rotates through the domain wall, that is a 60° or 120° domain configuration, then we find two useful rules about how the stripe lengths of these configurations (the ferroelectric domain wall) must orient relative to each other. First, domains of the same configuration will have stripes oriented at 60° to each other. This

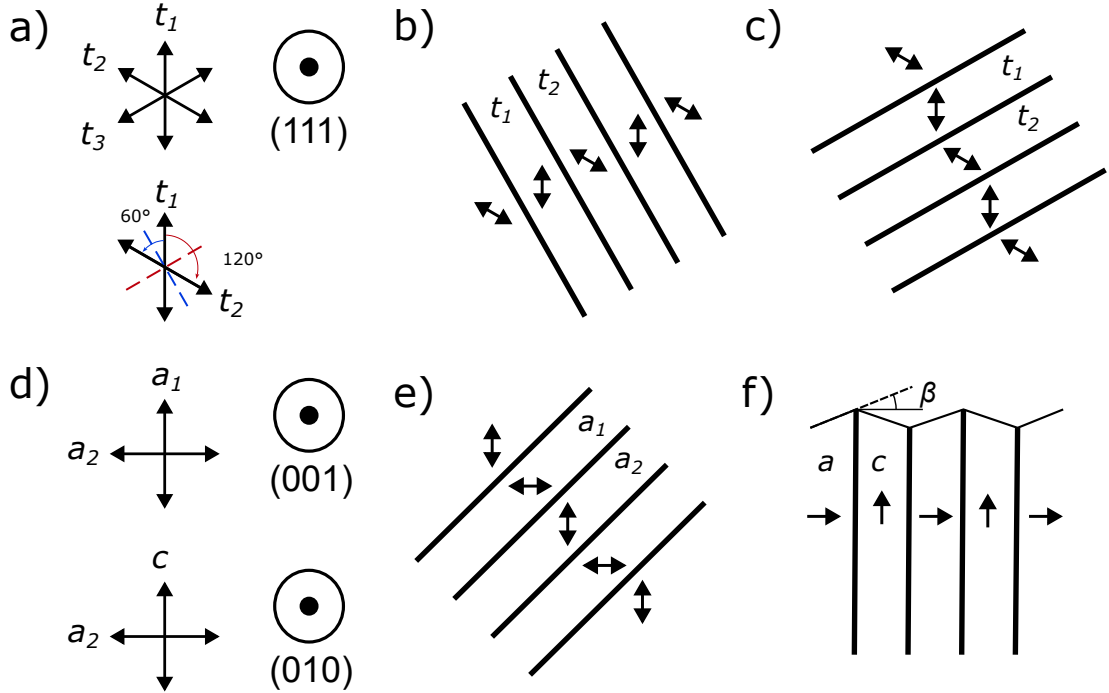


Figure 4.1: Differences in domain structure between (111) and (100) oriented BTO substrates. a) Projections of lattice elongations onto the (111) plane in BaTiO<sub>3</sub>. The orientations in which the lattice can be elongated and that the domain walls can form through either a 60° or 120° rotation. b) An example domain structure where the lattice elongation rotates through 60° between  $t_1$  and  $t_2$ . c) The alternative 120° rotation possible for a  $t_1 - t_2$  domain structure. d) Lattice elongations possible for a (100) substrate with two in-plane  $a_1$  and  $a_2$  axes and an out-of-plane  $c$  axis. e) The in-plane domain structure possible on the (100) plane. f) The  $a - c$  domain structure possible on (100) oriented substrates. The surface is canted as a result of the change in the out-of-plane thickness by an angle  $\beta$ .

is because the domain walls must form either between or along an axis of elongation and in both cases the equivalent directions are separated by  $60^\circ$ . Second, domains of opposite configurations will be separated by either  $30^\circ$  or  $90^\circ$ . This means that transitioning from a region in which the polarization rotates from  $60^\circ$  to one in which it rotates by  $120^\circ$  will be seen as a rotation in the ferroelectric stripe orientation by either  $30^\circ$  or  $90^\circ$ . This can be seen in Figure. 4.1 by comparison of Fig. 4.1b) and Fig. 4.1c) where the  $90^\circ$  case has been illustrated immediately, but the  $30^\circ$  case could also be seen if instead the  $120^\circ$  domain wall aligned along the axis of either  $t_1$  or  $t_2$ . As compared with the possible domain structures on the (100) cut of substrate (shown in Fig. 4.1e and Fig. 4.1f)) this means that there are two possible in-plane ferroelectric domain structures with two different angles of magnetoelastic anisotropy rather than the singular  $a_1 - a_2$  in-plane structure.

The substrate is made up of a large variety of ferroelectric domains in different orientations which are indistinguishable under polarized light microscopy, except by using the rules outlined above to determine relative configurations of one stripe region to another. Information about the direction of polarization could be extracted by either piezo-force microscopy or second harmonic imaging, techniques that are sensitive to the direction of polarization, but these are scanning probe microscopy techniques [124] typically used to image on the nanometer scale and this would present an issue with finding the same location in each experimental setup. At a first glance it is sufficient to use the geometric properties outlined above to locate regions of interest.

In the (111) plane the projection of the electric polarization has equivalent directions angled at  $60^\circ$  or  $120^\circ$  to each other. To minimize the static dipolar energy the ferroelectric substrate forms domains in which the polarization alternates between equivalent crystal directions. At domain wall boundaries the polarization then rotates through  $60^\circ$  either through the domain wall boundary resulting in a  $60^\circ$  domain configuration or normal to the domain wall boundary resulting in a  $120^\circ$  domain configuration. This is sketched in Fig. 4.2 where the existence of both of these types of domains is indicated at different locations in a sample. The polarization in BTO is the result of lattice elongations and for a sufficiently soft, magnetostrictive material, such as a sputtered CoFeB thin film, in which the strain is efficiently transferred, an in-plane easy axis will be imprinted into the ferromagnet with a local dependence upon the domain structure of the substrate.

### 4.3 Sample Growth

The sample is grown using DC magnetron sputtering as described in Chapter 3.2. A 20nm layer of  $\text{Co}_{40}\text{Fe}_{40}\text{B}_{20}$  is deposited at 300 °C, measured from the thermocouple attached to the heater, onto a 5x5x0.5mm  $\text{BaTiO}_3(111)$  substrate exhibiting ferroelectric domains at room temperature under polarized microscopy, and a 5nm Pt cap is deposited at room temperature. No seed layer is used between the substrate and the CoFeB layer. Ferroelectric domains were imaged in the manner described in Section 3.7.1.

The ferroelectric Curie temperature of BTO is 130°C, dependent upon the sample quality and the direction of temperature change, so a heater temperature of 300°C ensures the substrate is well above the Curie temperature. By cooling through the phase transition, the goal is to maximise the chance that strain is transferred efficiently to the thin film and ensure that the ferromagnetic domains couple to the ferroelectric domains.

The BTO(111) substrate exhibits ferroelectric domains as received and no poling is performed to create the domains that are observed. This substrate has a diversity of domain structure, shown in Fig. 4.2, in which the orientation of the stripe length between adjacent ferroelectric domains (labelled  $t_1$  and  $t_2$ ) varies which, from the rules outlined above, corresponds to a change in the underlying ferroelectric configuration.

### 4.4 Kerr Microscopy

Initial imaging confirms the presence of ferroelectric domains at the surface of the substrate visible through the magnetic film and capping layer. These domains are observed using a polarized light source and contrast is obtained as a result of the difference in refractive indices of the different ferroelectric domains. This is an intrinsic property of the crystal structure of the  $\text{BaTiO}_3$  in the tetragonal phase and has been well-documented in the literature [125, 126]. Magnetic contributions to the contrast are removed by using pairs of LEDs in equal and opposite Kerr geometries to result in no net contrast from the in-plane magnetic domains.

From ferroelectric imaging, it was found that both the 60° and 120° rotation configurations shown in Fig. 4.2 exist in these substrates. Fig. 4.3 shows images from three regions (a), (b) and (c) taken under the same conditions. Each image shows

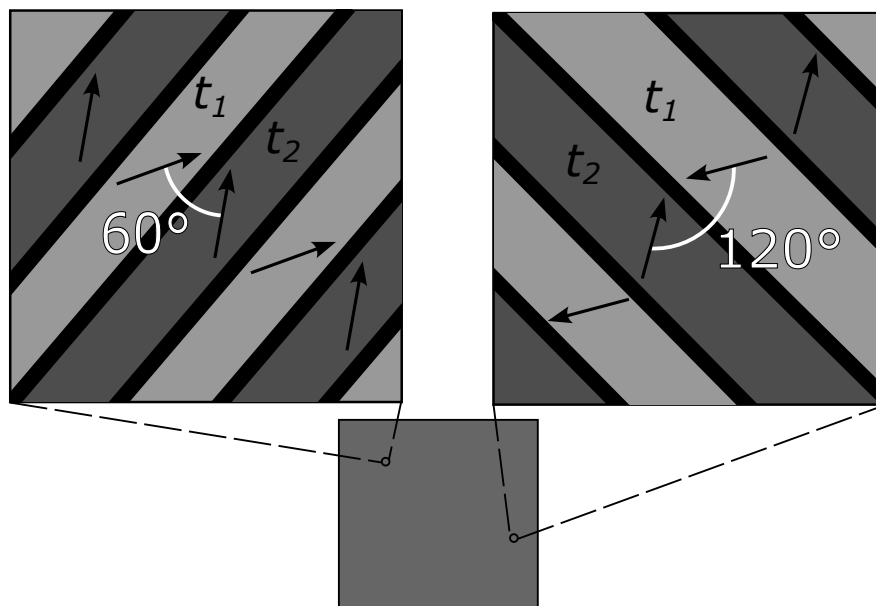


Figure 4.2: Schematic diagram of ferroelectric domains within a BTO(111) substrate. Both  $60^\circ$  and  $120^\circ$  domain walls can exist as shown in the two blown-up regions of the substrate. Arrows indicate the direction of ferroelectric polarization. Each region of ferroelectric domains contains many ferroelectric domains that alternate between two vectors with all domain walls in the same orientation. Different regions with a different set of underlying polarization vectors are then identified by a change in the orientation of ferroelectric domain walls.



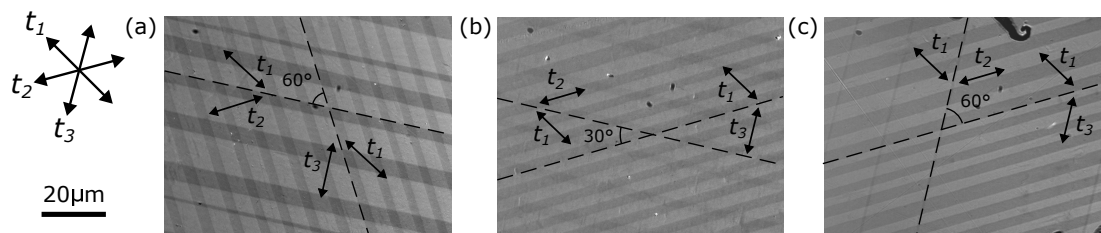


Figure 4.3: Polarised light microscopy of ferroelectric domains in BTO(111) in three distinct regions, A, B and C, illustrating different orientations of ferroelectric domain walls. Dashed lines indicate the ferroelectric domain walls, and double headed arrows represent possible directions of lattice elongation. In each of these regions it is possible to see two distinct ferroelectric domain structures through the penetration depths of the light into the substrate which is the origin of the two sets of domains with different domain wall orientations.

regions in which it is possible to view two sets of ferroelectric domains that overlap through the depth of the substrate as the substrate is optically transparent allowing for a significant penetration of light into the substrate. Represented alongside this are the three possible directions of lattice elongation,  $t_1$ ,  $t_2$ , and  $t_3$  within the same frame of reference that are offset from each other by  $60^\circ$ . The orientation of domain walls is highlighted by dashed lines.

Given the domain structures that are possible, the orientation of the ferroelectric domain walls is constrained such that domain configurations of the same type ( $60^\circ$  or  $120^\circ$ ) will have domain walls oriented at  $60^\circ$  to each other, whereas configurations of opposite type will have domain walls oriented at  $30^\circ$  or  $90^\circ$  from one to the other. If we make the assumption that in Fig. 4.3 (a) that both domains are  $60^\circ$  domains then we know from the angle between domain walls in (b) that (c) must correspond to a  $120^\circ$  configuration, and the opposite would be true if (a) was instead a  $120^\circ$  configuration and we thus show that all ferroelectric configurations and polarizations exist within the substrate.

Magnetic contrast is obtained using a subtraction technique to amplify the changes in light due to Kerr rotation and this is used to confirm the strain coupling between ferroelectric and ferromagnetic domains in Fig. 4.4. By comparing the ferroelectric and ferromagnetic images it is observed that the positions of the domain walls match exactly, one of which is highlighted by the dashed line in both images representing

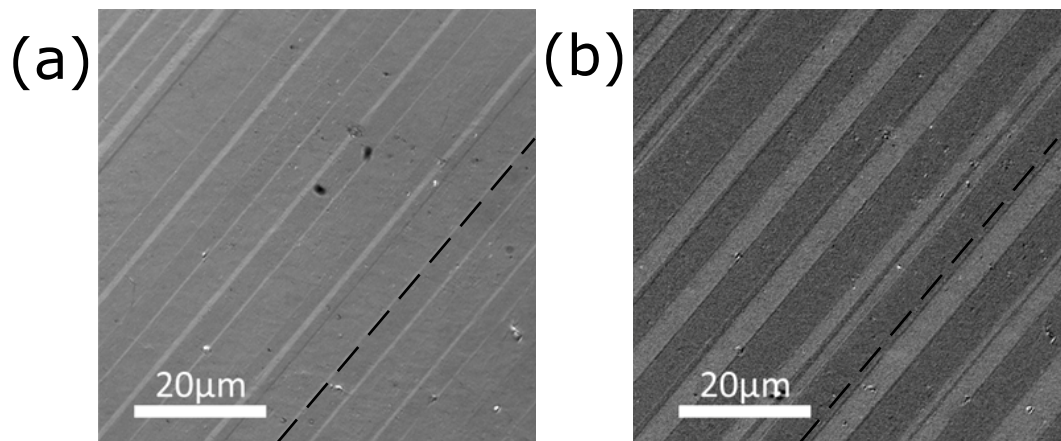


Figure 4.4: Coupling between a) ferroelectric and b) ferromagnetic domains in BTO(111)/CoFeB. Changes in magnetic contrast line up exactly with ferroelectric domain walls. The dashed line indicates the position of the same domain wall in each image.

the same domain wall. In these experiments, the contribution from the ferroelectric domains does not change under an applied magnetic field and can be subtracted as a constant, with any contribution towards magnetic images being an artefact of the sample position drifting from the point where the background image was taken.

Hysteresis loops are taken at varying angles with respect to the ferroelectric domain wall length, with a magnetic field applied parallel to the stripe length being defined as  $0^\circ$ . The behaviour is shown for two adjacent domains in one of the anisotropy configurations in Fig. 4.5, where ‘A’ and ‘B’ are the stripe domains on either side of the same ferroelectric domain wall. The presence of a significant in-plane anisotropy is apparent given by the strong angular dependence of the hysteresis loops, with a transition from an easy-axis response to a hard-axis one purely from a change in the angle at which the magnetic field is applied. Given that the film should be amorphous and no magnetic field was applied during growth, there should be minimal magnetocrystalline anisotropy and so it is concluded that this must be from the substrate and relates to the magnetoelastic coupling. It can also be seen from these loops that the hard axes in the adjacent domains are oriented at approximately  $60^\circ$  to each other, based on the  $A60^\circ$  and  $B120^\circ$  loops which are close to the exact hard axis.

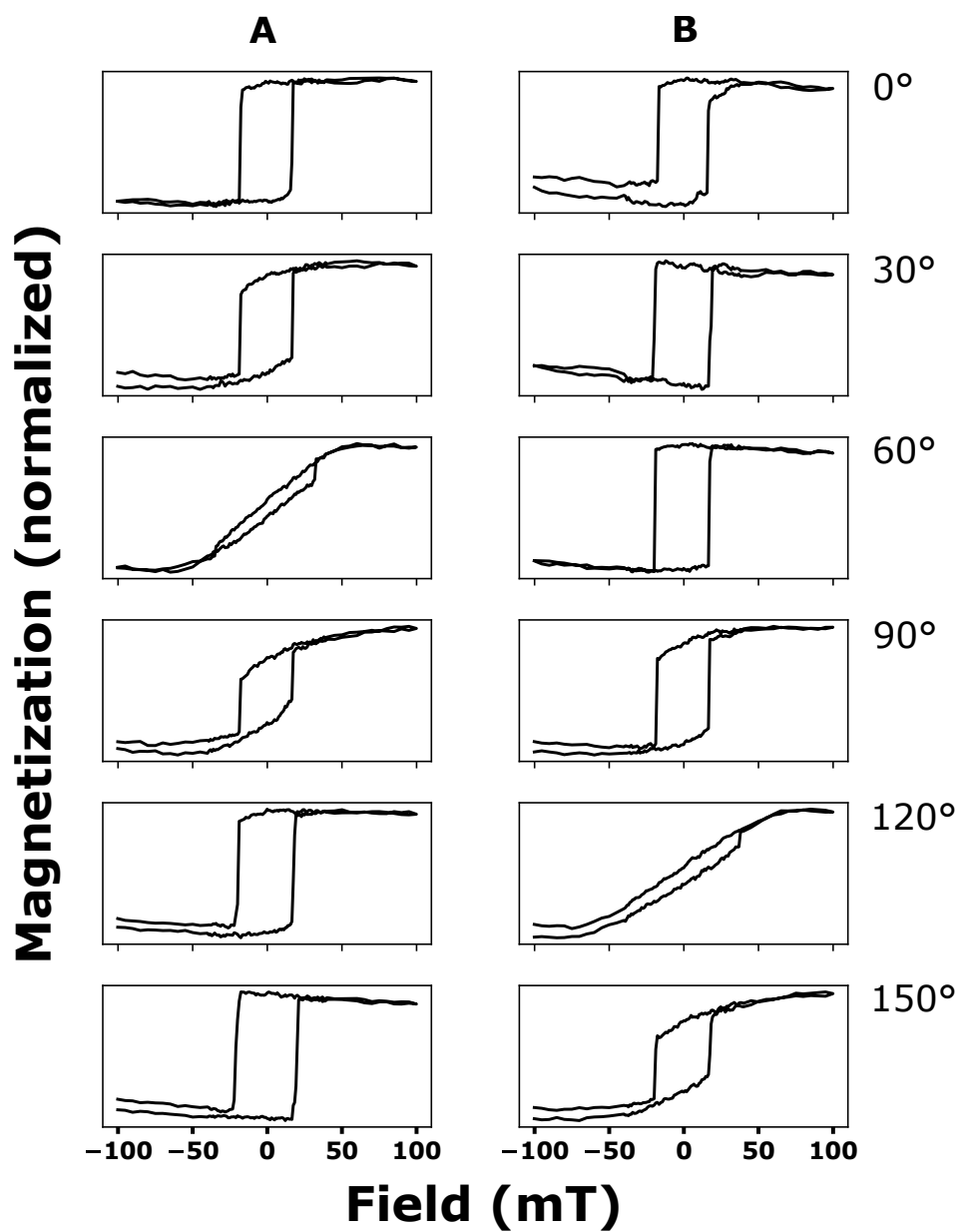


Figure 4.5: Kerr effect hysteresis loops taken at varying angles for two adjacent stripe domains labelled 'A' and 'B'. The angle at which the magnetic field was applied is indicated. Drift and Faraday effects have not been compensated for in these hysteresis loops.

The domains are further investigated by taking polar plots of the remanent magnetization which acts as a representation of how close to the easy axis each direction is, with a remanence close to 1 (in normalized units) representing a purely easy-axis aligned hysteresis loop and a remanence close to 0 being the hard axis. Angles are measured relative to the ferroelectric domain wall so that comparisons can be more easily drawn between different configurations. In Fig.4.6 the results are shown for two different regions of the film corresponding to the 60° and 120° configurations. The data is fit to a  $R \cos^2(\theta - \theta_0)$  function where  $R$  is an arbitrary scaling parameter (nominally 1) and  $\theta_0$  is the offset from zero that represents the orientation of the in-plane easy axis from the inverse magnetostriction. For both configurations, the angle between the easy axes in adjacent domains,  $\Delta$ , agrees well with a rotation of 60° and 120° for the respective configurations.

From the hard axis loops, the in-plane anisotropy field is measured and used to calculate the corresponding anisotropy constant from  $H_k = \frac{2K_{eff}}{\mu_0 M_s}$  by making the assumption that  $K_{eff} = K_{me}$  to obtain a value of  $K_{me} = 3.0 \times 10^4$  J/m<sup>3</sup> for the 60° domain configuration and  $K_{me} = 2.5 \times 10^4$  J/m<sup>3</sup> for the 120°. In these samples the 120° domain regions are generally much smaller by up to an order of magnitude, typically in the region of microns, while the 60° regions can be 10s of microns in scale. This could explain the difference in the magnitudes of  $K_{me}$  as it has been shown previously [47] to decrease with reduced ferroelectric domain width, with a more pronounced effect in thinner films.

Using the previously identified regions a 40mT magnetic field was applied parallel and perpendicular to the ferroelectric stripe direction and the sample was imaged with longitudinal and transverse contrast [113] to obtain images corresponding to the charged and uncharged domain wall states. Fig. 4.7 shows the charged and uncharged 60° (Fig. 4.7a) and 120° (Fig. 4.7b) configurations. For both configurations the application of a magnetic field along the length of the stripe produces a magnetically uncharged domain wall type in which the magnetization smoothly rotates from one domain to the other, and application perpendicular to the stripe produces a magnetically charged domain wall. The presence of both is in agreement with similar experiments in BTO(100) substrates where the charged and uncharged domains form in the same alignment as in these experiments [127], as well as previous experiments performed during deposition of Pd/Co onto BTO(111) substrates [128].

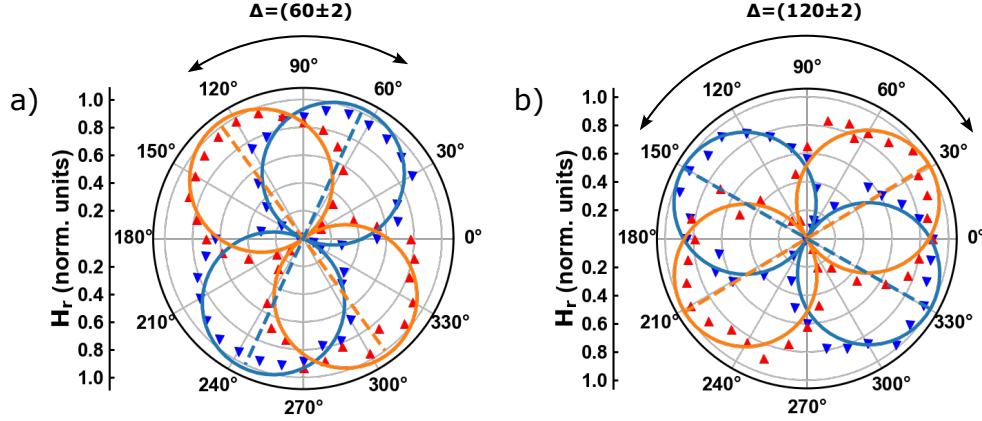


Figure 4.6: Remanent magnetization taken from hysteresis loops in individual magnetic domains for a)  $60^\circ$  and b)  $120^\circ$  configurations, with the orientation of the easy axes marked by dashed lines. Red and blue triangles represent adjacent magnetic stripes from which data is obtained.  $\Delta$  is the change in angle through the domain wall boundary, here oriented at  $90^\circ$ .

The charged and uncharged domain walls in the  $60^\circ$  and  $120^\circ$  configurations are distinct and distinguished by the change in magnetization angle from one domain to the other. Based on the directions of the easy axes in adjacent stripes and the contrast shown in Fig. 4.7 the spin rotation through the magnetic domain wall for each domain wall type can be deduced. In the  $60^\circ$  configuration the charged domain wall has a spin rotation of  $60^\circ$  and the uncharged domain wall has a spin rotation of  $120^\circ$ , and the opposite is true for the  $120^\circ$  configuration. This results in a total of four unique domain wall structures in these BTO(111)-based heterostructures as shown in Fig. 4.7. This concept was also discussed for BTO(111)-based heterostructures by Franke et al. [128] as ‘quasiparallel’ and ‘quasiperpendicular’ domains which corresponded to the acute and oblique angles of magnetization rotation respectively, regardless of the angle between the imprinted magnetoelastic easy axes. However in the experimental setup described here it was possible to freely rotate the sample and apply a magnetic field allowing for further investigation.

The type of domain wall was found to have an impact on the propagation of magnetic domains in both of these regions. The domain propagation follows the elongation axis set by the ferroelectric domains which makes for visually distinct domain patterns

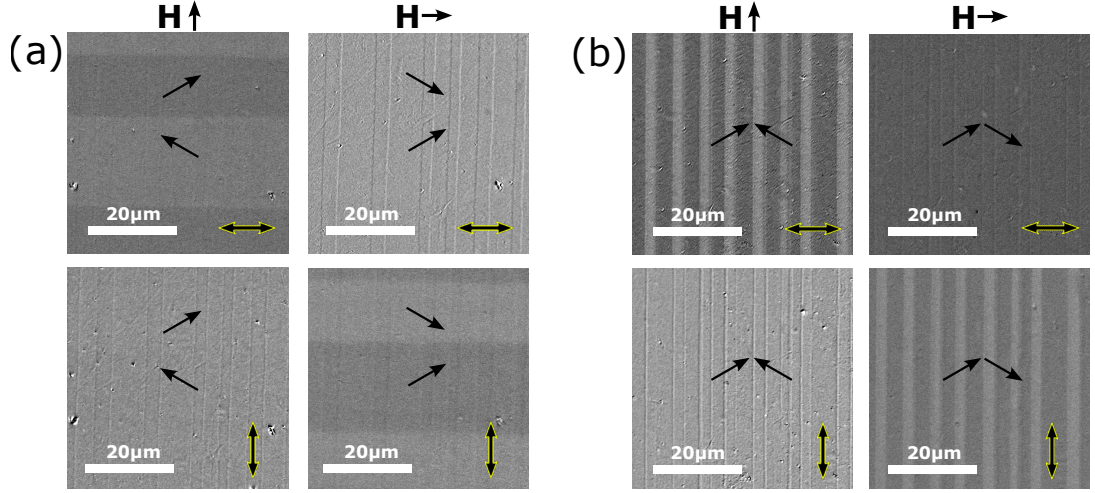


Figure 4.7: All four field-contrast combinations for a) 60° and b) 120° domain patterns. Black arrows indicate the local direction of magnetization, black and yellow double-headed arrows show the direction of magnetic contrast and the direction of applied field is shown at the top of the column.

dependent upon the ferroelectric domain configuration. For a 60° domain wall the acute angle results in arrow-head domains and for 120° domain walls the magnetic domains propagate over long distances in a staircase pattern, both of which can be seen in Fig. 4.8 a) and b) respectively for the  $\theta = 0^\circ$  case. The angle of the magnetic domain wall to the ferroelectric domain wall agrees well with the angles between the easy axes found in Fig. 4.6, although there is some deviation as a result of defects in the magnetic film, magnetic domains joining, and various other effects that cause the magnetic domains to bend and change as they propagate particularly over long distances in the very wide ferroelectric domains where this deviation is more pronounced.

The reversal domain patterns have a strong dependence on the angle of applied magnetic field with respect to the domain wall. To show this the film is saturated under a negative magnetic field and domains are nucleated with a field of 17 mT, close to the coercivity, for different field directions. The change in domain formation pattern is summarized in Fig. 4.8 with the field angle shown for each domain image produced. If the field is applied perpendicular to the ferroelectric domains, the domains form in a co-operative manner in which domains can easily propagate from one stripe to the next. This gives rise to the arrow-head and staircase domains previously mentioned.

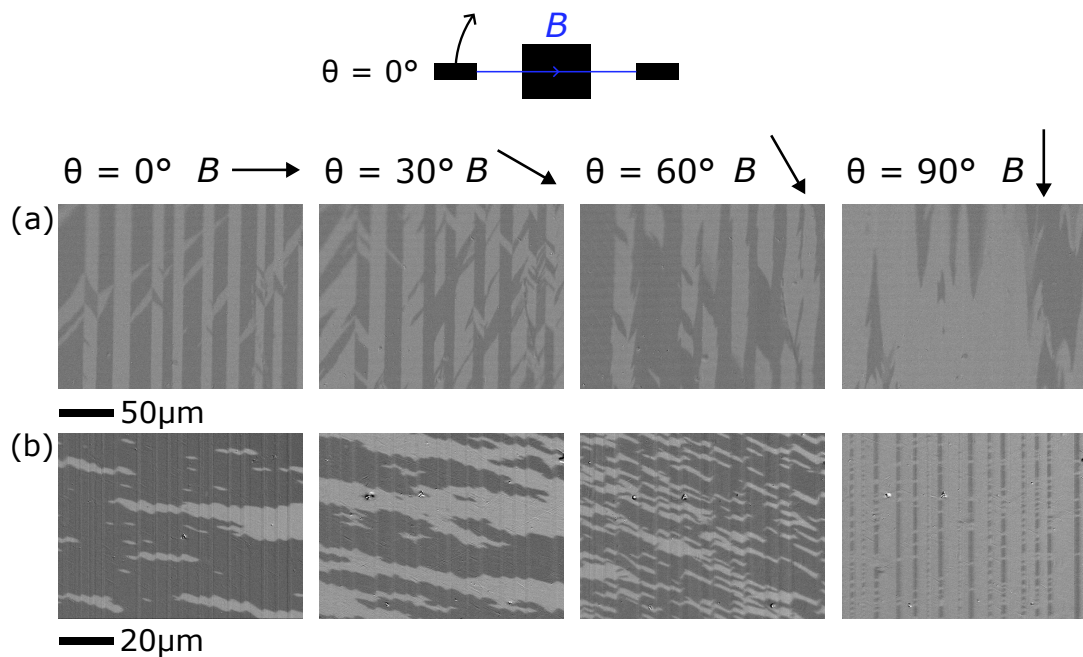


Figure 4.8: Magnetization reversal at an applied field of 17 mT for a)  $60^\circ$  and b)  $120^\circ$  domain configurations as a function of field angle. Direction of the magnetic field is indicated above the images and scale bars are indicated below. Each of the eight reversal processes defined by domain wall configuration and field angle is represented by a single image. A schematic representation of the experiment is shown above, with the pole pieces rotating around the sample to achieve the angles specified in a) and b).

As the angle increases and approaches the direction of lattice elongation the density of domains nucleated increases and eventually when the angle exceeds the magnetoelastic easy axis of one of the ferroelectric domains then domains are nucleated preferably in one set of ferroelectric stripes. In this state the domains nucleate along the length of one set of stripes first and then the other set of stripes switch. Qualitatively, this agrees with results obtained previously for BTO(100)/CoFeB heterostructures [47] where it was found that applying a magnetic field parallel to the domain wall results in one set of stripes switching preferably before the other set, and applying the field perpendicular showed no such behaviour. The transition agrees well with the results shown in Fig. 4.6 with the transition for the 60° state in Fig. 4.8 a) occurring at 30° and the transition for the 120° state in Fig. 4.8 b) occurring at 60°.

## 4.5 Photo-emission Electron Microscopy

The domain wall profile is further investigated by x-ray magnetic circular dichroism photo-emission electron microscopy (XMCD-PEEM), a high resolution x-ray imaging technique which is sensitive to the local magnetic texture. The experiment was performed at the Diamond Light Source on the I06 nanoscience beamline using the PEEM end station. An obtained image is shown in Fig. 4.9a) in which the contrast has been enhanced in post-processing by subtracting images taken with opposite circular polarizations of incoming x-rays.

This experiment was performed on a separate sample to the one measured in the prior experiments but with nominally the same material structure. The sample was prepared in the 60C domain wall state, verified in the Kerr microscopes, prior to measurement in the PEEM system which was employed to measure the domain wall profile.

In this experiment it was only possible to prepare the sample in a 60C domain wall state, that is the anisotropy axes rotated by 60° between adjacent domains and the magnetization rotated in a head-to-head or tail-to-tail fashion through the domain wall. The field of view used was 10  $\mu\text{m}$ .

We find that this technique is extremely suitable for measuring the profile of these charged domain wall textures. The profile shown in Fig. 4.9b) is well-defined fit to a generic  $y = A \tanh\left(\frac{x-x_c}{\delta}\right)$  domain wall profile, where  $\delta$  is the domain wall width which is obtained in this measurement to be (260±20) nm with the error based on the stated resolution for the XMCD-PEEM.



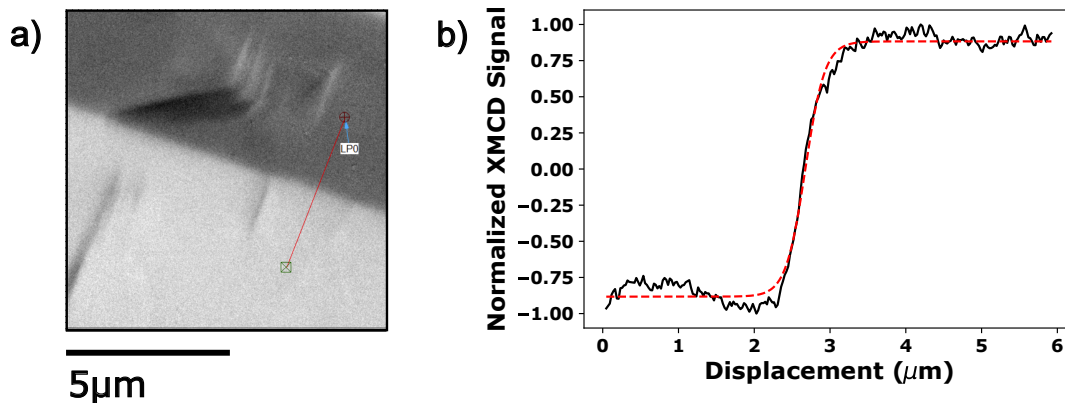


Figure 4.9: a) Magnetic domain image taken using XMCD-PEEM for a 60C domain wall state. b) The result profile of the XMCD signal taken along the LP01 line, with the red dashed line being a fit to the data.

## 4.6 Micromagnetic Simulations

This section will now demonstrate several further properties of these films using the results obtained from prior experiments to simulate the system in a micromagnetic framework MuMax3 [120]. This has previously been used to simulate very similar heterostructures and has been shown to be in good agreement with experimental results. For these simulations the micromagnetic parameters used were a saturation magnetization  $M_{sat} = 854 \times 10^3$  A/m, exchange stiffness  $A_{ex} = 2.1 \times 10^{-11}$  J/m, magnetoelastic anisotropy  $K_{u1} = 3 \times 10^4$  J/m<sup>3</sup> for the 60° configuration and  $K_{u1} = 2.5 \times 10^4$  J/m<sup>3</sup> for the 120° configuration. The values of saturation magnetization and anisotropy strength have been obtained from experiments in this chapter while the exchange stiffness is taken from previous work [127].

The system is divided into two regions with uniaxial anisotropy vectors corresponding to the direction of in-plane lattice elongation in adjacent ferroelectric stripes dependent upon which of the two domain types is being simulated. As the domain wall width of a ferroelectric material is typically on the order of a few unit cells [129, 130] it is assumed that the change in the direction of the uniaxial anisotropy vector is abrupt and there is no transition region. Within this setup I have investigated the change in the spin rotation, with angles taken relative to the orientation of the magnetoelastic

easy axis, and domain wall width defined as:

$$\delta = \int_{-\infty}^{\infty} \cos^2(\phi'(x)) dx \quad (4.2)$$

where  $\phi'$  is the reduced magnetization angle as a function of displacement normal to the domain wall defined as,

$$\phi'(x) = \left( \phi(x) - \frac{|\phi_{\frac{d}{2}} - \phi_{-\frac{d}{2}}|}{2} \right) \frac{180}{|\phi_{\frac{d}{2}} - \phi_{-\frac{d}{2}}|} \quad (4.3)$$

and the angles  $\phi_{\frac{d}{2}}$  and  $\phi_{-\frac{d}{2}}$  are the angles of the magnetization far from the domain wall on either side, here best represented by a distance of  $d/2$  which is half the defined stripe width,  $d$ . The quantity  $|\phi_{\frac{d}{2}} - \phi_{-\frac{d}{2}}|$  is the total spin rotation across the domain wall. This reduced magnetization angle will then be  $-90^\circ$  on one side of the domain wall and  $+90^\circ$  on the other such that the contribution to  $\delta$  will be 0 far from the domain wall where the magnetization is not longer varying spatially.

This method of calculating the domain width has been used previously [90, 127] and encompasses the entirety of the spin rotation in a reduced domain wall angle system much better than fitting to a *tanh* function as would normally be performed for a Bloch type domain wall. The resulting four micromagnetic domain wall structures are shown in Fig. 4.10, for an excerpt around the domain wall.

In these simulations, a saturating field is applied at a variety of angles and the system is then allowed to relax in zero field. The domain wall reliably forms at the boundary between adjacent easy axes and it is around this point that the spin rotation is calculated and domain wall profiles are obtained. The angle of the applied field is rotated from  $\theta = 0^\circ$  along the normal of the domain wall and the polar plots in Fig. 4.11 are produced. Domains produced in this way reliably relax into only the charged or uncharged state, with the domain width for the charged state being up to 5 times greater. Surprisingly, the domain width has no angular dependence close to the transition angle which is different for each configuration, but instead sharply transitions from an uncharged domain wall to a charged domain wall when the field aligns with one of the magnetoelastic anisotropy axes. This agrees well with the results in Fig. 4.8 in which it is shown that crossing a magnetoelastic easy axis changes the way in which domains propagate through the film - this is the result of the applied field changing from producing an uncharged or charged domain wall state.

The spin rotation in both of the charged domain wall states is reduced, from  $60^\circ$  or  $120^\circ$  to  $53^\circ$  and  $111^\circ$  for the 60C and 120C states respectively. This is a result of the

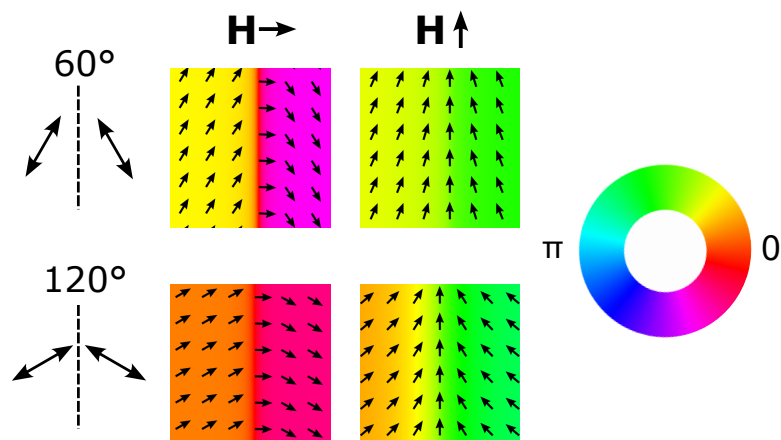


Figure 4.10: Micromagnetic simulations of the four domain wall configurations. Local direction of magnetization is shown by the black arrows. The underlying uniaxial anisotropy configuration is shown by the cartoon graphic on the left, and the initializing field direction is indicated above. HSV colour also represents the angle of magnetization as indicated by the colour wheel.

Domain Wall configuration	Domain wall width
60C	192 nm
60U	47 nm
120C	238 nm
120U	48 nm

Table 4.1: Relaxed domain wall widths for all four domain wall configurations

value of saturation magnetization used in these simulations. For charged domain walls the saturation magnetization has a large impact on the domain width [128], and this leads to a suppression of the spin rotation. The spin rotation of charged states is also much more heavily dependent on the thickness of the film than the uncharged state and this will also contribute to the suppression of the rotation [131]. In the relaxed state, the calculated domain wall widths for these domain walls are collated in Table 4.1. There is some discrepancy between the charged domain wall widths due to the difference in anisotropy measured in the individual regions, but the values calculated are on a similar order of magnitude as that obtained in the PEEM experiments previously.

The dependence of the spin rotation and domain wall width under an applied mag-

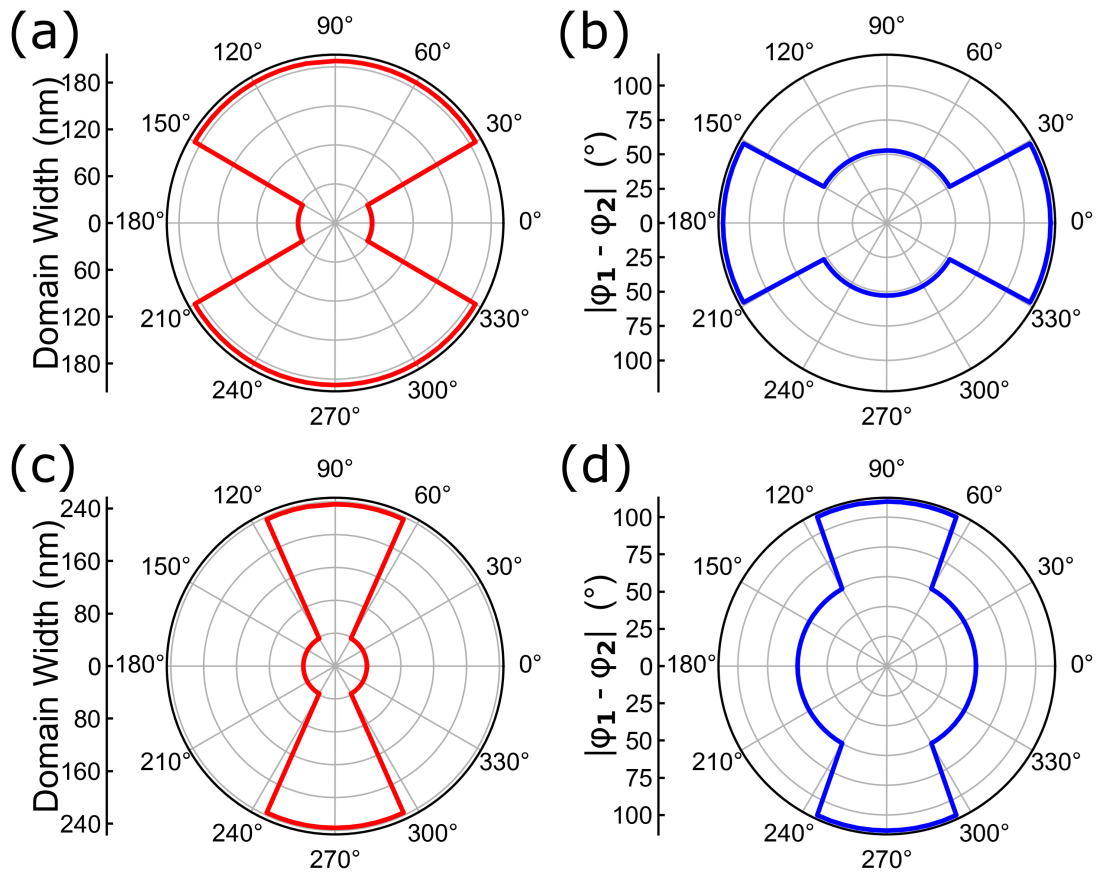


Figure 4.11: Micromagnetic simulations of the domain width (a), (c) and spin rotation (b), (d) for 60° and 120° configurations respectively as a magnetic field is rotated with respect to the ferroelectric domain wall.

netic field is investigated in all four domain wall configurations. For ease of reference, I choose to label configurations by assigning them a number defined as the angle between magnetization in adjacent domains and the uncharged/charged nature of the domain wall, 60U, 60C, 120U and 120C. In all instances, the spin rotation behaves the same under an applied magnetic field, with a decrease in amplitude that corresponds to the gradual realignment of spins from the easy axes to the field direction. The domain width however shows two characteristic behaviours. In Fig. 4.12a the 60C configuration follows the realignment of spins while the 60U domain wall is initially more resistant to change and mirrors the realignment of spins. In Fig. 4.12b the behaviour is inverted with the 120C wall showing a similar trend to the 60U domain wall, and the 120U and 60C also being similar in character. From this it can be understood that the behaviour of the domain wall depends on the rotation of magnetization between adjacent domains more so than the charged or uncharged nature. There is a discrepancy in the observed behaviour between the  $60^\circ$  and  $120^\circ$  sets of states, namely that both the 60U and 60C states reorient smoothly as compared to the  $120^\circ$  states. This is most likely due to the reduced value of anisotropy used in the simulations for the  $120^\circ$  states which, as discussed previously, is believed to be measured smaller than the bulk value as a result of the ferroelectric stripe width.

The four different configurations have different responses that have important implications for any applications that could make use of domain wall width. The percentage change of domain width as compared to the initial state is greatest in the 60C (38%) and 120U (35%) where the spin rotation drops off from  $60^\circ$  and follows the realignment of spins to the field. Conversely in the states the relationship is a mirror of the spin rotation and is much more resistant to the effects of an applied field demonstrating a smaller reduction in the domain width for both the 120C (28%) and 60U (20%) states.

## 4.7 Summary

In this chapter I have investigated the pattern transfer from ferroelectric stripes in BTO(111) substrates to a CoFeB thin film obtained via strain coupling at the interface and shown that there are four unique magnetic domain wall configurations that can be initialized in these heterostructures corresponding to rotations in the easy axes of either  $60^\circ$  or  $120^\circ$  and their charged or uncharged variations. These regions behave differently with entirely different domain patterns and switching mechanisms controlled purely by

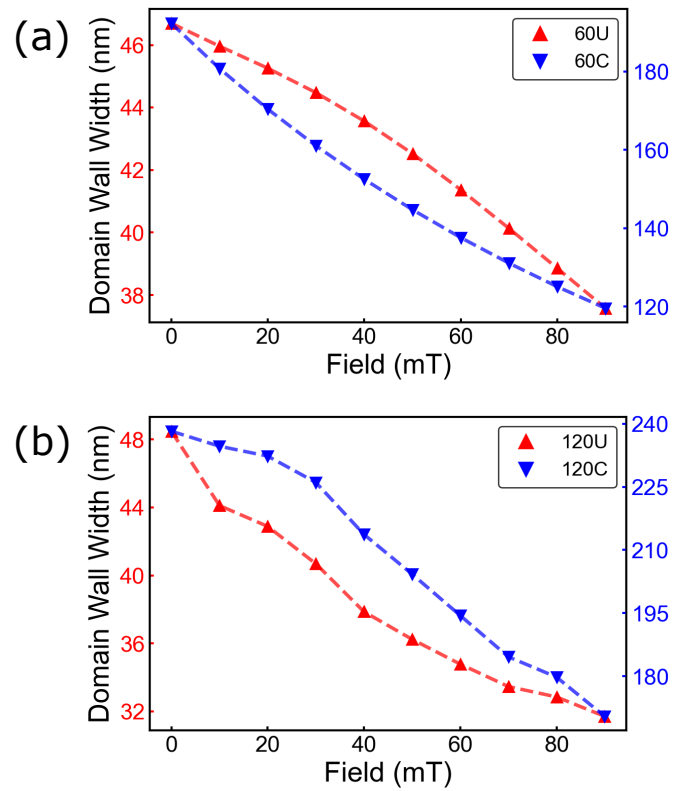


Figure 4.12: Magnetic field dependence of domain width in (a) the  $60^\circ$  configuration and (b) the  $120^\circ$ . Left and right axes correspond to the uncharged and charged domain wall widths respectively.

the angle between adjacent magnetoelastic anisotropy axes in adjacent domains.

Using micromagnetic simulations I was able to confirm the experimental observations by calculating the angular dependence of the domain wall width showing that the transition from uncharged to charged wall happens abruptly as the field direction crosses the orientation of the lattice elongations in-plane. The results predict that the response of the domain widths to an in-plane field for each of these states is unique, with the charged  $60^\circ$  state presenting the best case for domain wall width tunability both in terms of absolute change and in terms of the response type with this case exhibiting the most linear change. This presents an additional option for the control of devices in which a magnetic domain wall could be the core component.

---

# CHAPTER 5

---

Temperature Control of Magnetic Properties in  
BaTiO<sub>3</sub>(111)/CoFeB Films



## 5.1 Introduction

In the previous chapter, I have shown that growing a ferromagnetic film of  $\text{Co}_{40}\text{Fe}_{40}\text{B}_{20}$  on a (111)-oriented  $\text{BaTiO}_3$  substrate couples the magnetic domain structure to the ferroelectric domain structure and leads to two in-plane magnetoelastic anisotropy configurations. The impact of these two in-plane strain-coupled configurations was explored with attention placed on the magnetic domain wall textures and on the magnetic domain structure we might expect beyond the ideal head-to-head and head-to-tail domain structures. The ways in which these states could be manipulated was not explored.

In this chapter, I will focus on the temperature response of the heterostructure system. The BTO substrate has a diverse temperature response, with 2 phase transitions below room temperature into different polar crystal phases and one above room temperature into a cubic non-polar phase. I will explain this in detail and with specific reference to the (111) plane and the strain that can be expected from lattice elongations on this plane.

The temperature response of coupled BTO(111)/CoFeB films was investigated across the whole sample and at the individual domain level. Samples are grown in the manner previously explained in Chapter 4. Variable-temperature measurements are carried out using a SQUID-VSM for bulk magnetometry and magnetic imaging is performed using Kerr microscopes with either an optical cryostat or heater stage with optical access (for low-temperature and high-temperature measurements respectively) using a 60 $\times$  lens. By varying the temperature through these crystal phase transitions it was possible to access these different polar phases with large changes in lattice elongation and assess the viability of strain-dependent devices based on BTO(111) substrates, measured by the response of the properties of the ferromagnetic film deposited on top.

This chapter is adapted from the paper in Ref. [132] (under review). Low-temperature Kerr microscopy was performed at the EXTREMAG facility in Exeter with the assistance of P. S. Keatley.

## 5.2 Temperature Dependence of Crystal Phases

Barium titanate has a rich temperature response. It contains all of the prototypical perovskite ferroelectric phases, with a high-temperature non-polar cubic phase that becomes tetragonal at 130 °C, orthorhombic at 5 °C and rhombohedral at -90 °C. Each

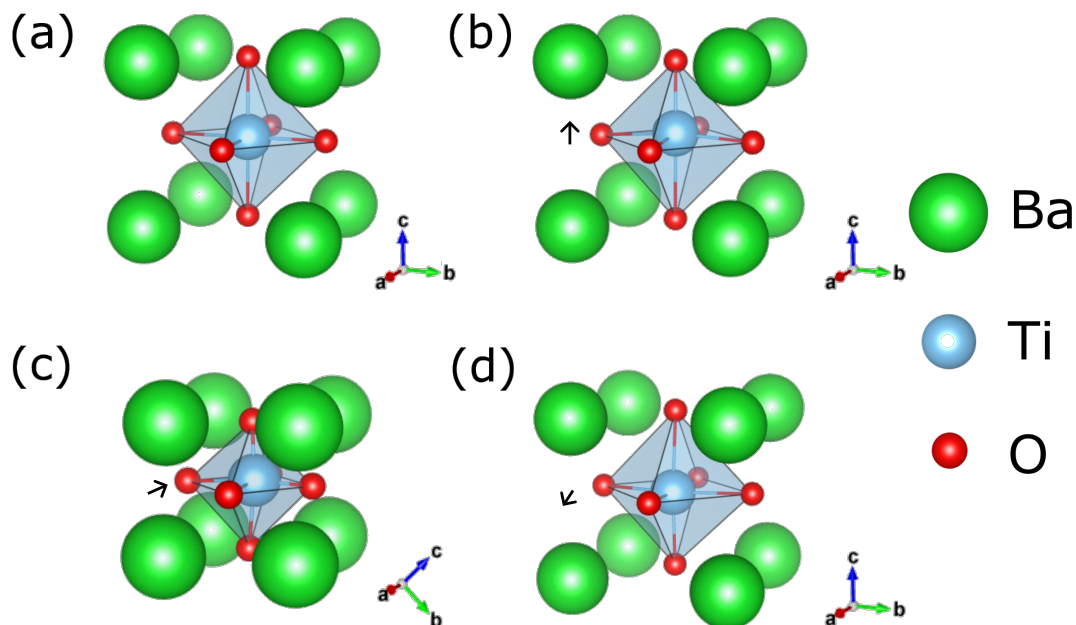


Figure 5.1: Crystal phases of  $\text{BaTiO}_3$  plotted using Vesta [136] Presented in order from high-to-low temperature, a) the cubic phase, b) the tetragonal phase, c) the orthorhombic phase and d) the rhombohedral phase. The bonds of the oxygen octahedron are highlighted to show the movement of the  $\text{Ti}^{4+}$  ion within the octahedron. Black arrows indicate the direction along which the  $\text{Ti}^{4+}$  ion is displaced from the centre of the unit cell, seen also in the change in the Ti-O bond angles. Orientations of the cubic  $a$ ,  $b$  and  $c$  axes are shown in the bottom right of each structure.

of these is represented in Fig. 5.1, recreated from lattice parameters reported in the literature [133–135] and the crystal modelling software VESTA [136]. I have shown the oxygen octahedron to better display the change in the displacement of the  $\text{Ti}^{4+}$  ion between the crystal phases. In the tetragonal phase, the lattice is elongated along one crystal axis only, and the Ti ion has a large displacement along the  $c$ -axis in this consideration. In the orthorhombic and then rhombohedral phase the lattice is elongated along 2 and then 3 crystal axes, and the Ti ion displacement is correspondingly translated along two and then three axes.

Here I will discuss the lattice elongations of each phase in more detail. As mentioned in the previous chapter, the lattice elongations on the  $(111)$ -plane for the tetragonal phase lie in  $(11\bar{2})$ -like directions. The magnitude of these lattice elongations can be

## 5.2 Temperature Dependence of Crystal Phases

---

found by finding the projection of the lattice constants on the (111) plane. This is done by calculating and comparing the distance between Ba atoms. Fig. 5.2 shows the distribution of Ba atoms on the (111) plane. The distance between Ba atoms on the (111) plane in the cubic phase is defined as  $a' = \sqrt{2}a$ , and the perpendicular distance  $a'' = \sqrt{\frac{3}{2}}a$ , where  $a$  is the lattice constant. In the tetragonal phase, one axis is elongated and there is a special  $c$  axis and the unit cell is defined by the  $a$  and  $c$  lattice constants. The distance between barium atoms is greater along this  $c$  axis and is now  $c' = \sqrt{a^2 + c^2}$ . The shorter in-plane lattice parameter remains the same as in the cubic phase. The perpendicular distance becomes  $c'' = \sqrt{c'^2 - a^2}$  and the lattice elongation in the tetragonal phase can now be defined as,

$$\Delta_t(111) = \frac{c'' - a''}{a''} = \sqrt{\frac{1}{3}} \sqrt{1 + \frac{2c^2}{a^2}} - 1, \quad (5.1)$$

where  $a''$  is the unelongated perpendicular distance in the cubic phase.

In the orthorhombic phase the lattice elongations lie along the  $\langle 110 \rangle$  directions. They can be divided into two subsets: the  $\langle 1\bar{1}0 \rangle$  and  $\langle 110 \rangle$ . The dot product of  $\langle 1\bar{1}0 \rangle$  with the (111) normal vector is always zero and so this set of polarization vectors lies in the (111) plane. For polarizations along  $\langle 110 \rangle$ , the projection in the (111) plane is,

$$p_{proj} = \begin{pmatrix} 1 \\ 1 \\ 0 \end{pmatrix} - \frac{2}{3} \cdot \begin{pmatrix} 1 \\ 1 \\ 1 \end{pmatrix} = \frac{1}{3} \begin{pmatrix} 1 \\ 1 \\ 0 \end{pmatrix}, \quad (5.2)$$

which is along the same direction as the  $\langle 1\bar{1}0 \rangle$  vectors but reduced in magnitude.

The distance between barium atoms is  $a' = \sqrt{a^2 + c^2}$  for the shorter distance and then  $c'$  or  $b'$  for the longer distance, although both  $b'$  and  $c'$  are elongations in the same set of axes. They are related to the pseudocubic lattice parameters as  $b' = 2c \sin(\alpha/2)$  and  $c' = 2c \cos(\alpha/2)$ , where  $\alpha$  is the angle between the  $a$  and  $c$  axes [133].

For polarizations along  $\langle 1\bar{1}0 \rangle$  the lattice elongation becomes,

$$\Delta_o(111) = \frac{c' - a'}{a'} = \frac{2c \cos(\alpha/2)}{\sqrt{a^2 + c^2}} - 1, \quad (5.3)$$

and polarizations along  $\langle 110 \rangle$  have a lattice elongation of,

$$\Delta_o(111) = \frac{b' - a'}{a'} = \frac{2c \sin(\alpha/2)}{\sqrt{a^2 + c^2}} - 1. \quad (5.4)$$

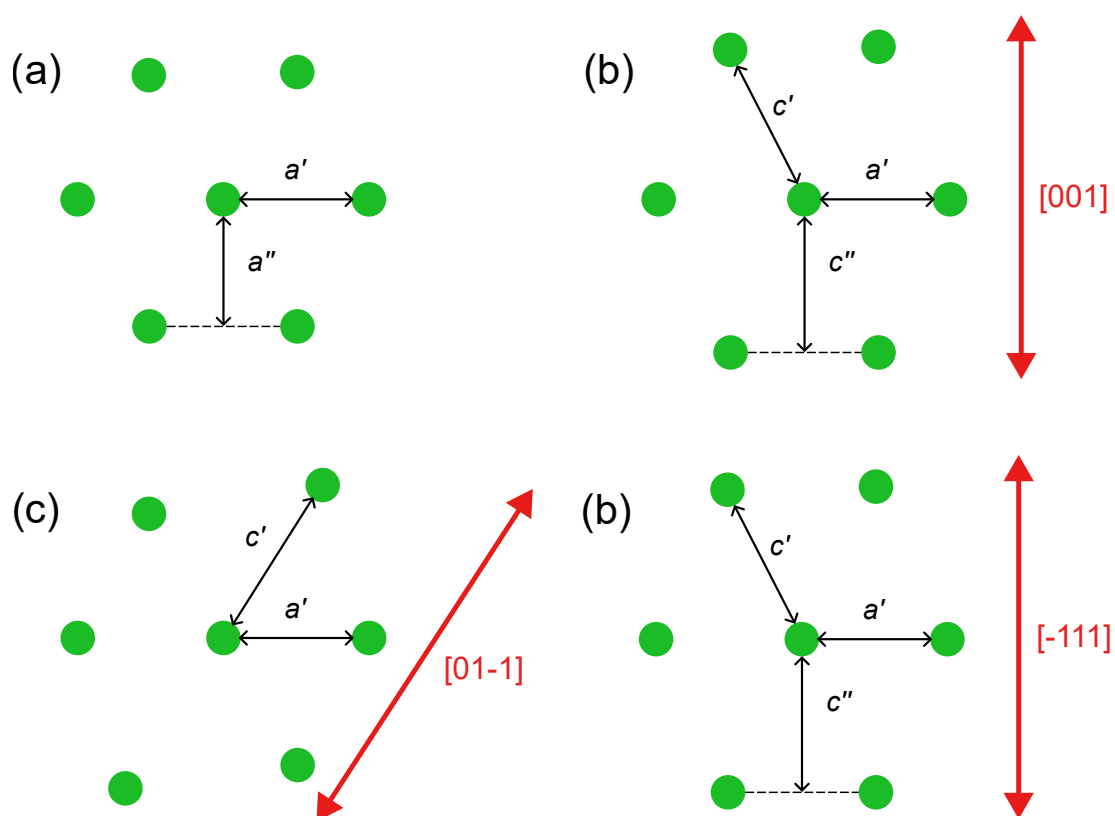


Figure 5.2: Crystal lattice structure of BaTiO<sub>3</sub> on the (111) plane for the a) cubic, b) tetragonal, c) orthorhombic and d) rhombohedral phases. Only the barium atoms are shown for brevity. One direction of elongation is shown for each phase. Red arrows indicate the axis along which the crystal lattice is distorted.

In the rhombohedral phase, the lattice elongation lies along the  $\langle 111 \rangle$  directions inherently, in which case only one direction of lattice elongation does not lie in the plane, that of the  $(111)$  direction which defines the normal to the plane. For the rest, which take vectors in the form of  $(11\bar{1})$ , the projection in the  $(111)$  plane is:

$$p_{proj} = \begin{pmatrix} 1 \\ 1 \\ -1 \end{pmatrix} - \frac{1}{3} \begin{pmatrix} 1 \\ 1 \\ 1 \end{pmatrix} = \frac{2}{3} \begin{pmatrix} 1 \\ 1 \\ -2 \end{pmatrix}, \quad (5.5)$$

which is along the same directions as in the tetragonal phase, the  $[11\bar{2}]$  directions. The values  $a'$  and  $c'$  in this phase are the same as the  $b'$  and  $c'$  in the orthorhombic phase, defined as  $a' = 2a \sin(\alpha/2)$  and  $c' = 2a \cos(\alpha/2)$ . The perpendicular distance of the elongated crystal is then  $c'' = \sqrt{c'^2 - (\frac{a'}{2})^2}$ . To calculate the lattice elongation we compare the distance  $c''$  with the equivalent distance an elongation along  $(111)$  which does not distort the crystal, which is  $a'' = \sqrt{a'^2 - (\frac{a'}{2})^2} = \sqrt{3}a \sin(\alpha/2)$ .

The lattice elongation for these directions of polarization is:

$$\Delta_r(111) = \frac{c'' - a''}{a''} = a \frac{\sqrt{4 \cos^2(\alpha/2) - \sin^2(\alpha/2)}}{\sqrt{3}a \sin(\alpha/2)} - 1 \quad (5.6)$$

As in Chapter 4, the in-plane magnetoelastic anisotropy angles will be restricted to only  $60^\circ$  or  $120^\circ$  for all phases and so all the possible magnetic domain wall configurations are illustrated in Fig. 5.3.

## 5.3 Bulk Magnetometry

The change in magnetic moment with temperature was investigated using SQUID-VSM magnetometry. The temperature response of the sample is measured in an applied field of 200 mT between room temperature and 77 K. This temperature is well below the rhombohedral phase transition at 190 K. A magnetic field of this strength, greater than the local anisotropy field measured previously at room temperature, is chosen to bias the moment towards the magnetic field direction across phase transitions. The results in Fig. 5.4 show two hysteretic changes in magnetic moment around 190 K and 280 K, corresponding to the rhombohedral-orthorhombic and orthorhombic-tetragonal phase transitions of the BTO respectively. This hysteretic behaviour is an expected property of the BTO substrates, which have been widely reported [137–139] to have

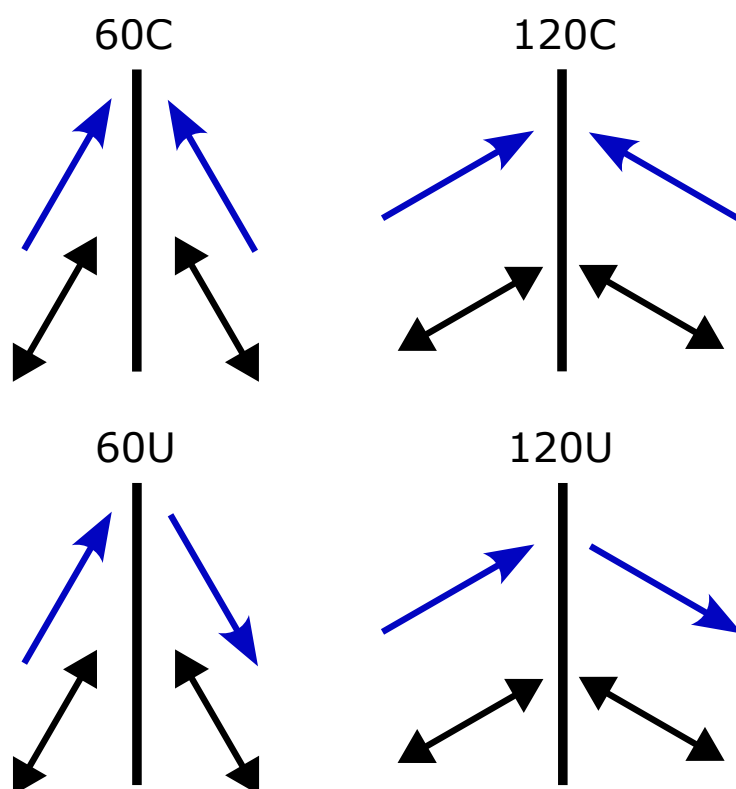


Figure 5.3: Schematic illustration of the magnetization and anisotropy configurations in the strain-coupled ferromagnet. The domain wall configurations are labelled by the underlying angle between the magnetoelastic anisotropy axes ( $60^\circ$  or  $120^\circ$ ) and the charged or uncharged nature of the domain wall structure leading to four configurations: 60U, 60C, 120U and 120C. Black double-headed arrows indicate the direction of magnetoelastic anisotropy, blue arrows represent the direction of local magnetization.

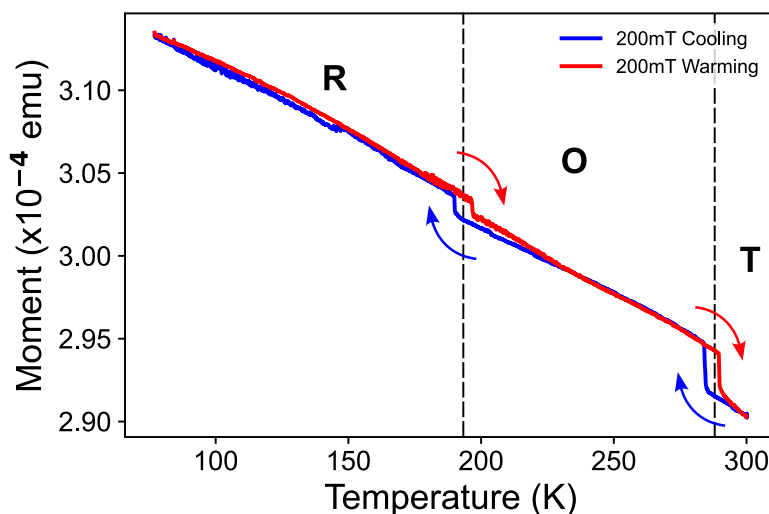


Figure 5.4: MvT measurement in an applied field of 200 mT. The blue curve corresponds to data taken during cooling, with the red curve taken while heating to room temperature. The regions corresponding to the rhombohedral (**R**), orthorhombic (**O**), and tetragonal (**T**) phases of BaTiO<sub>3</sub> are indicated. Dashed lines indicate the average phase transition temperature.

hysteretic phase transitions in a variety of properties including the lattice parameters, which are closely coupled to the lattice elongations of the ferroelectric order. Similar behaviour has been observed in epitaxial BTO-ferromagnet systems in the literature and attributed to either the change in strain [138] or the change in ferroelectric domain structure (and so, the resulting magnetic easy axes) [139] and demonstrates strong strain coupling between the substrate and film in all crystal phases.

Next the change in saturation magnetization with temperature was investigated. In Fig. 5.5 the saturation magnetization as a function of temperature is shown. The result of this is values that fit well to a standard  $T^{3/2}$  fit with no discontinuities in  $M_s(T)$  indicating that the strain is insufficient to change the saturation magnetization. This means that the temperature hysteresis observed in Fig. 5.4 most likely corresponds to the abrupt change in ferroelectric domain structure at the phase transitions of the BTO substrate. While 200mT is in excess of the coercive field at all temperatures, it is not sufficient to pin the magnetization to the field direction as the ferroelectric domain structure, and consequently the local magnetoelastic anisotropy, abruptly changes. Performing the same MvT with a larger 1T field suppresses the change in moment across

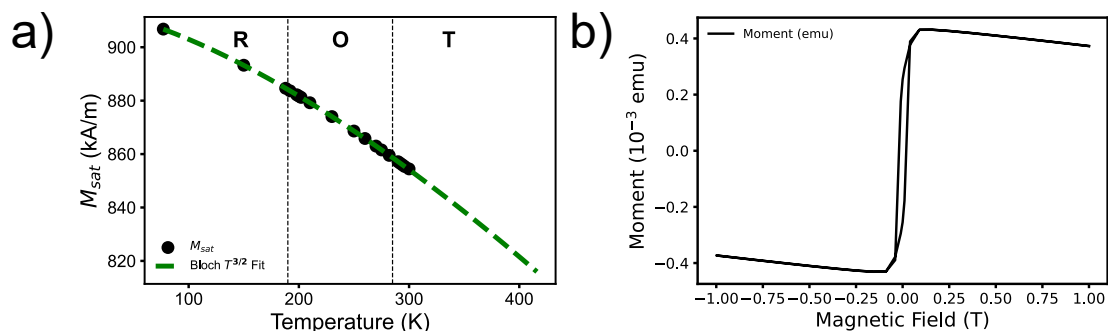


Figure 5.5: a) Saturation magnetization (points) for 20nm CoFeB thin film coupled to a BTO(111) substrate, extracted from hysteresis loops at each temperature and the corresponding Bloch  $T^{3/2}$  law fit (dashed line). Indicated are the temperatures at which the rhombohedral (**R**), orthorhombic (**O**) and tetragonal (**T**) phase transitions occur. No significant change around these points is observed. b) Example hysteresis loop taken at room temperature without the background subtracted. Hysteresis loops are taken with a maximum field of 1 T.

these transitions. In the case of these amorphous thin-film ferromagnets, it would seem that the change in domain structure is more important than the change in strain for these whole-sample measurements.

It is proven that this is not a change in saturation magnetization by varying the applied magnetic field in Fig. 5.6 on a nominally identical sample. As the substrate is not the same as the one used in prior measurements it has a different underlying ferroelectric domain structure and no poling was performed on either substrate to obtain comparable domain widths, density, etc. This results in the field being oriented at a different angle to the ferroelectric domains than for the sample shown in Fig. 5.4 which is the principle sample under investigation in this chapter. This change in domain structure leads to a difference in the transition behaviour, with the **T**→**O** phase transition leading to a reduction in magnetic moment. This effect was previously seen by Venkataiah et al. on BTO(100) based heterostructures [139]. Under an increasing magnetic field strength, the magnitude of change in moment around the phase transitions is reduced with no change being distinct under an applied field of 1 T. From previous results in Chapter 4, it would be expected that the sample is fully saturated for the 200 mT and 1 T measurements. However, those measurements are performed locally within only one ferroelectric domain region and so may only represent the ideal



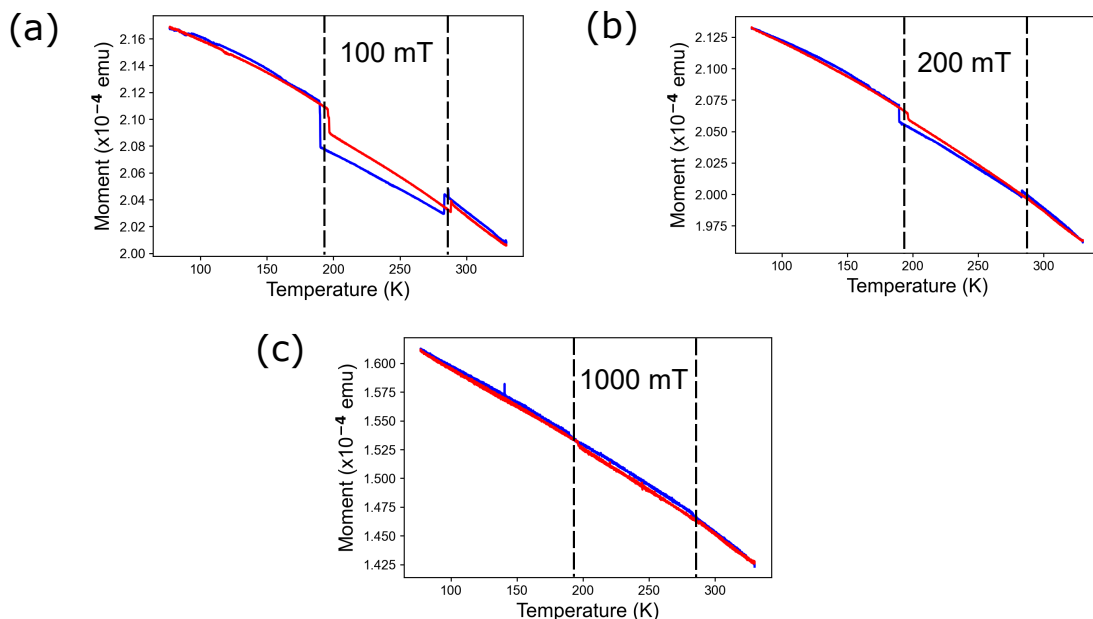


Figure 5.6: Field-cooled and field-warmed measurements of a BTO/CoFeB heterostructure under a) 100 mT, b) 200 mT and c) 1000 mT magnetic fields. With increasing field strength the change in moment around the phase transitions of BTO is suppressed. Dashed lines indicate the average phase transition temperature.

monodomain situation. The measurements here are global and it may be the case that the diversity of ferroelectric domains gives rise to moments that are not fully aligned with the field. Cooling or heating through the phase transition then changes the ferroelectric domain structure, and the magnitude of this misalignment changes dependent on the difference in ferroelectric domains between the two polar phases. However as has been seen a large enough magnetic field is sufficient to overcome these effects which ensures that it is not a signal observed from the substrate.

## 5.4 Local Magnetoelastic Anisotropy

The results from the SQUID-VSM measurements in Figs. 5.4 and 5.5 represent the volume-averaged response of the sample. As mentioned previously there are many ferroelectric domains within the sample with different orientations of lattice elongation that leads to a variety of imprinted magnetoelastic easy axes in the CoFeB film. While it was possible to infer strain coupling between the ferroelectric substrate and ferro-

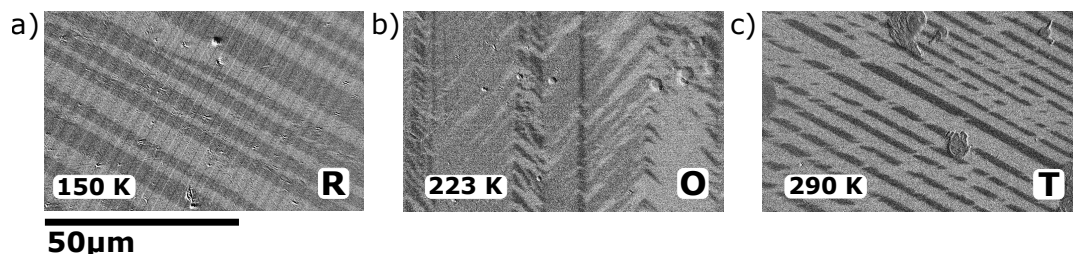


Figure 5.7: Ferromagnetic domain images taken in the same vicinity for the a) rhombohedral (**R**), b) orthorhombic (**O**), and c) tetragonal phases (**T**). The magnetic stripe orientation changes to match the ferroelectric domain structure demonstrating good coupling between films across phase transitions.

magnetic film, it is not possible to probe in detail the effect of the substrate on the ferromagnetic film as it is not deposited onto a monodomain substrate, making it more challenging to interpret the results. To understand in more detail the effect of temperature on the strength of the magnetoelastic anisotropy within one ferroelectric domain, local measurements were performed using a Kerr microscope to focus measurements down to one region of ferroelectric domain structure and coupled regions corresponding to individual ferroelectric domains.

Using optical cryostat attachments wide-field Kerr microscopy was performed on the sample in two setups, a cryo-stage with liquid nitrogen that allows cooling down to 77 K (well below the orthorhombic and rhombohedral phase transitions) and a heater-stage in which the sample is heated to above 420K (the tetragonal to cubic phase transitions). Fig. 5.7 shows the result of domain imaging in the same region across three different phases, imaged here in zero applied magnetic field. The presence of stripe domains in all three polar phases are in excellent agreement with the SQUID data presented previously and work carried out on (100)-oriented substrates in the literature [140], and shows that the strain is sufficient to couple the domains at all temperatures.

In this experimental setup, it is not possible to precisely ascertain the ferroelectric (and anisotropic) configuration of the region before and after the phase transition as the sample cannot be freely rotated so a rigorous extrapolation of the easy axes cannot be performed. However, we can gain some understanding of the configuration from the orientation of the domain walls and the angle at which  $180^\circ$  domain walls are canted relative to the stripe axis. In the tetragonal and rhombohedral phases, the projection

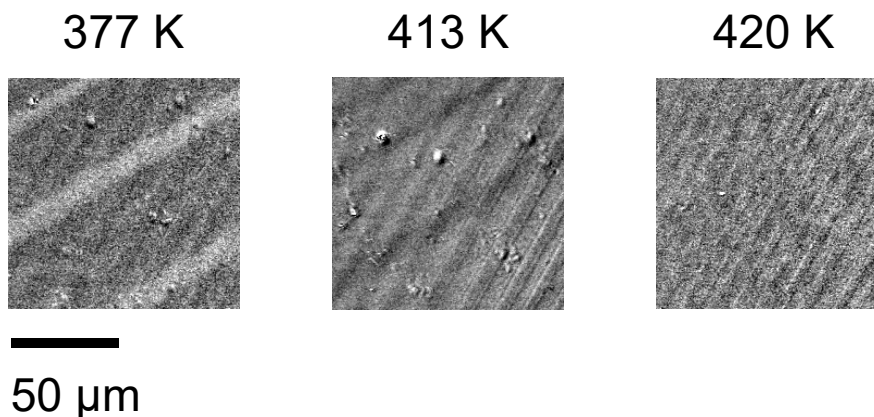


Figure 5.8: Change in magnetic domain structure around the ferroelectric Curie temperature. At 420 K, the striped ferromagnetic domains disappear indicating that the surface strain has vanished.

of lattice elongation onto the (111) surface lies in  $[11\bar{2}]$ -like directions and so stripes oriented in the same direction in both crystal phases will maintain the same ferroelectric configuration with the rotation between the easy axes remaining the same [123]. In the orthorhombic phase, the lattice elongation lies along  $[01\bar{1}]$ -like directions, which is the orientation of domain walls in the tetragonal and rhombohedral phases. As a result, a rotation of the domain wall by  $30^\circ$  or  $90^\circ$  indicates that the ferroelectric configuration remains the same, and a rotation of  $0^\circ$  or  $60^\circ$  is indicative of a change in the ferroelectric configuration from either a  $60^\circ$  to  $120^\circ$  or vice versa. For example, Fig. 5.7 displays the same stripe orientation in the **R** and **T** phases from which it is inferred that the ferroelectric configuration is the same in both phases.

In the domain images presented here, the  $180^\circ$  reversal domains within the stripe length oriented at approximately  $30^\circ$  to the stripe length indicate that the **T**-phase region has a  $60^\circ$  configuration, and that the **O**-phase image has a  $120^\circ$  configuration, and indeed the stripe orientation rotates by  $60^\circ$  as it should for a change in ferroelectric domain type. The case where the ferroelectric configuration remains the same between the **R** and **T** phases has been shown - however a rotation of  $90^\circ$  was also observed suggesting that both outcomes are equally likely. Separately, in the heater stage, it was observed that the magnetic stripe domain structure vanishes above the Curie temperature of BTO ( $\approx 420\text{K}$ ) and is shown in Fig. 5.8.

Starting from a base temperature of 77 K the value of the anisotropy field is ex-

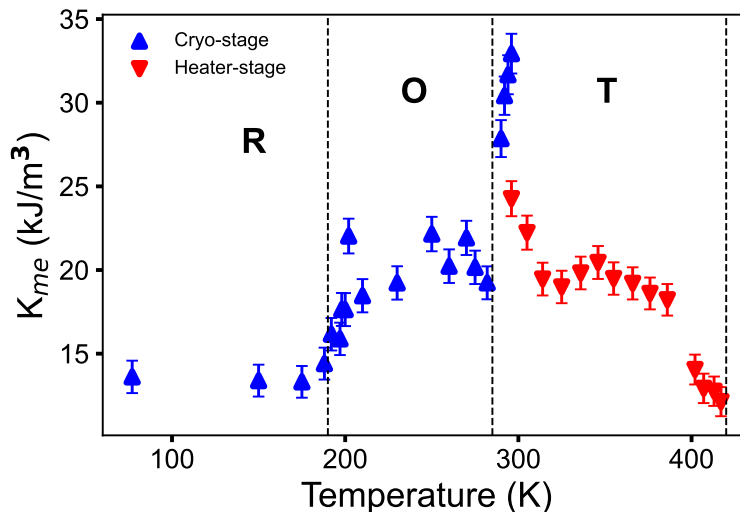


Figure 5.9: Local magnetoelastic anisotropy imprinted in the CoFeB film by the BaTiO<sub>3</sub>(111) substrate. Dashed lines indicate the phase transitions between the rhombohedral (**R**), orthorhombic (**O**) and tetragonal (**T**) phases of the substrate.

tracted from hard-axis hysteresis loops measured from individual stripe domains and the value of anisotropy calculated from  $H_k = \frac{2K_{eff}}{\mu_0 M_s}$ . Values for  $M_s$  were taken from the previously presented data where possible and the obtained fit is used to extrapolate values for high temperatures.

The results are summarized in Fig. 5.9. The change in anisotropy far from the phase transitions shows three distinct levels for the measurements performed in the cryo-stage, one for each polar phase. From the rhombohedral to orthorhombic phase there is a change in the magnitude of the magnetoelastic anisotropy from an average value of  $(14 \pm 1)$  kJ/m<sup>3</sup> in the rhombohedral phase to a value of  $(20 \pm 1)$  kJ/m<sup>3</sup> in the orthorhombic phase. In the region around the O-R phase transition the magnitude of the magnetoelastic anisotropy smoothly transitions between these two average values. Whereas, when going from the orthorhombic phase to the tetragonal the increase is sharp with presumably some saturation to a maximum value around room temperature. To examine this in more detail, the expected magnitude of the lattice elongations (relative to the in-plane lattice constant) in the (111) plane have been calculated based on the reported results from Kwei et al. [133] and is shown in Fig. 5.10. Lattice elongations in the tetragonal and rhombohedral phases use values of  $a''$  and  $c''$  calculated

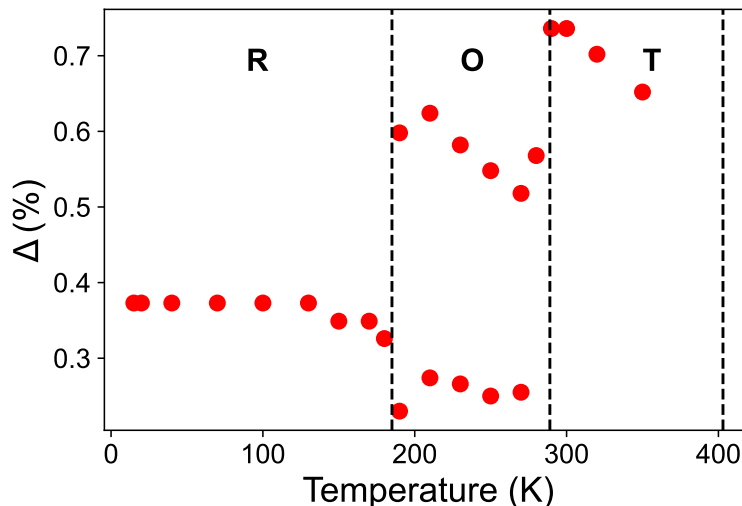


Figure 5.10: Calculated magnitude of the lattice elongations on the (111) plane using structural data obtained by Kwei et al. [133], expressed as a percentage of the in-plane lattice parameter.

based on the reported lattice parameters, while the ones for the orthorhombic phase use the calculations performed by Kwei et al.

In the rhombohedral phase, there is minimal change in the lattice parameters and there is no significant changes to the measured magnetoelastic anisotropy far from the orthorhombic phase transition. In the orthorhombic phase, there are two possible levels of lattice elongation corresponding to directions of ferroelectric polarization with either the major or minor component of the biaxial lattice elongation lying in the (111) plane. The shorter lattice elongation should show a continuous change across the phase transition, however in these results the same behaviour is instead reflected in what must correspond to the larger lattice elongation as the magnetoelastic anisotropy increases from the rhombohedral to orthorhombic phase. The discontinuous ‘jump’ in the lattice elongation at the orthorhombic-tetragonal transition is well reflected in these measurements of  $K_{me}$ .

For measurements performed on the heater stage, there is a large discrepancy that leads to a discontinuous transition between the two datasets. This was attributed to effects observed in previous work [123], where there can be a large difference in the magnitude of  $K_{me}$  between the  $60^\circ$  or  $120^\circ$  domain states, and measurements here were

performed on different regions of the sample. Regardless, it shows the changes from the initial state with an approximately linear reduction from 315-385 K corresponding to the decrease in lattice elongations and then a sharp drop off close to the ferroelectric Curie temperature at approximately 420 K (in agreement with the Curie temperature seen in the work by Lahtinen et al. [140]) where the polar order reduces. Above this Curie temperature, it was not possible to observe any magnetic stripe domains as the ferroelectric order is no longer present and there is no meaningful in-plane anisotropy.

## 5.5 Micromagnetic Simulation

Using the measured values of  $K_{me}$ , the resulting implications that the change in magnetoelastic anisotropy has for the magnetic domain wall width (DWW) has been explored. In a micromagnetic [120] framework the effect of temperature on the DWW of charged and uncharged domain wall configurations has been studied. The simulation is divided into three distinct regions of uniaxial anisotropy corresponding to different directions of lattice elongation in adjacent ferroelectric domains. This is illustrated in Fig. 5.11a. The central stripe width is set to be 2  $\mu\text{m}$  and the micromagnetic cell size is 2 nm x 2 nm x 20 nm, and periodic boundary conditions are used in the  $x$  and  $y$  directions. Values of  $K_{u1}$ , representing the parameter previously defined as  $K_{me}$ , and  $M_{sat}$  are informed from the above experiment with the assumption made that similar magnitudes of  $K_{me}$  can be expected for all ferroelectric domains. Values of  $A_{ex}$  are taken from previous work examining the temperature dependence of exchange stiffness [141] of Co which is likely to be an overestimate for a CoFeB system. This is intended not to predict the exact values of the DWW but instead to examine how it scales with temperature taking into account the relative scaling of all relevant micromagnetic parameters.

For all phases of BTO the projection of the polarization onto the (111) plane leads to an angle between adjacent lattice elongations of either 60° or 120°, depending on which axes the polarization switches between. In each ferroelectric domain, the magnetization is strongly pinned to the imprinted magnetoelastic anisotropy axis which leads to magnetic domain walls that are pinned to the ferroelectric domain walls with a reduced wall angle dependent upon how the bulk magnetization rotates between the ferroelectric domains. The magnetization can rotate in a head-to-tail or head-to-head fashion leading to charged or uncharged domain wall structures. In total, this means that there are four domain wall structures to consider by combining the possible ferro-

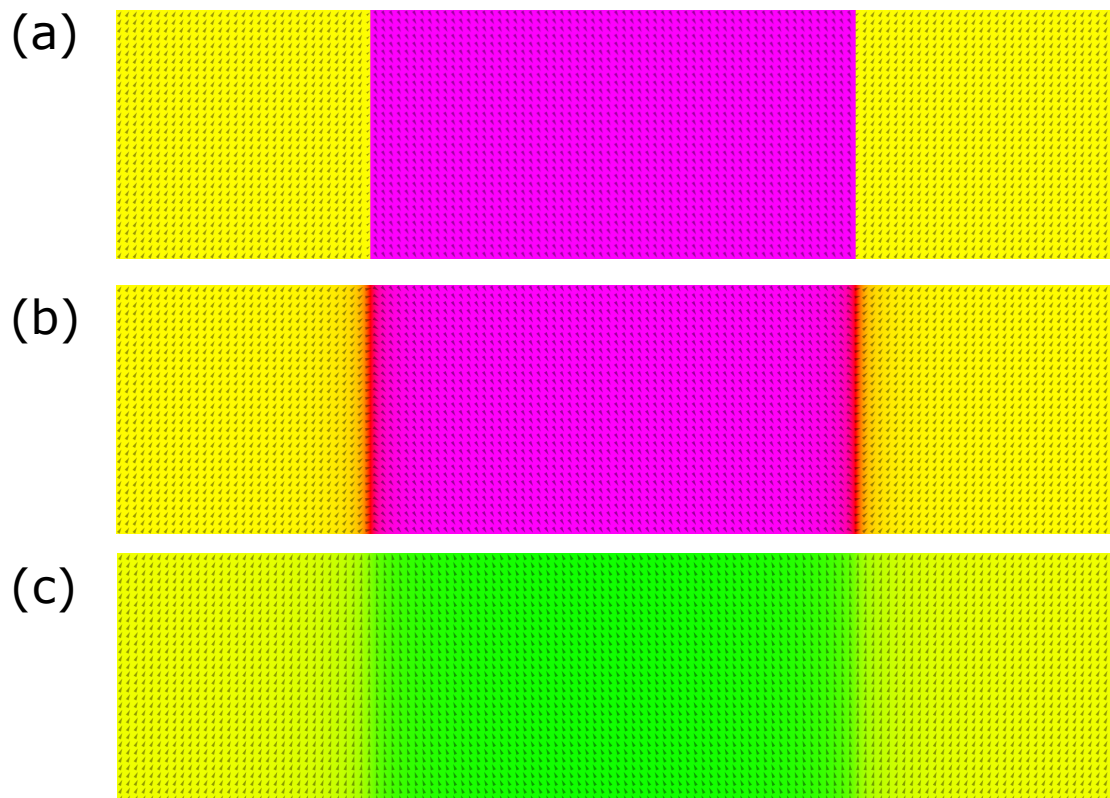


Figure 5.11: a) Representation of the spatially-varying anisotropy directors in micromagnetic simulations for the  $60^\circ$  ferroelectric domain structure, with the anisotropy axis set by a vector direction. b) Simulated magnetic domain structure initialized in the uncharged configuration. c) Simulated magnetic domain structure initialized in the charged configuration. Arrows and colour represent vector direction.

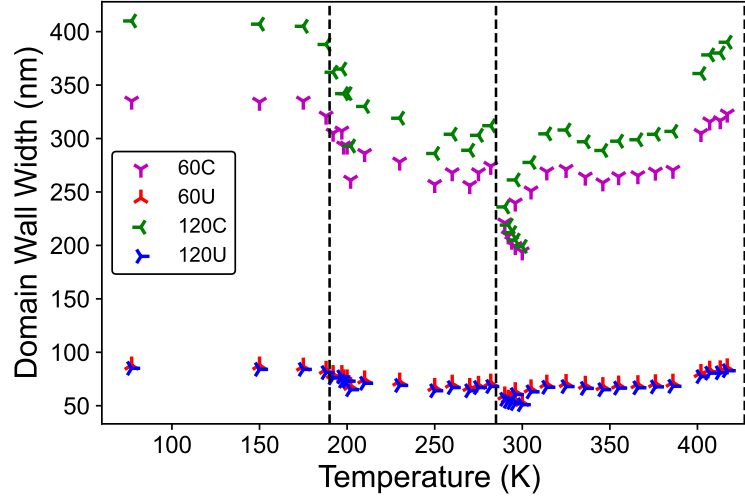


Figure 5.12: Domain wall width in the charged (C) and uncharged (U) configurations as a function of temperature. Numbers in the legend represent the total angle through the domain wall between the magnetoelastic anisotropy axes in adjacent stripe domains corresponding to the rotation of polarization.

electric rotations and charged or uncharged states: a rotation of  $60^\circ$  with charged (60C) or uncharged (60U) character and a rotation of  $120^\circ$  with charged (C) or uncharged (U) character. These were previously illustrated in Fig. 5.3.

Within each of the pre-defined stripes, the magnitude of the in-plane anisotropy remains the same but the orientation of the magnetoelastic anisotropy is varied (rotating by either  $60^\circ$  or  $120^\circ$ ). Periodic boundary conditions are used in both the  $x$  and  $y$  dimensions and the domain wall is homogenous in the  $y$ -axis. To calculate the domain wall width,  $\delta$ , the method outlined in previous work [123, 127] was used, using the integral definition of the domain wall width,

$$\delta = \int_{-\infty}^{\infty} \cos^2(\phi') dx, \quad (5.7)$$

with  $\phi'$  being the reduced magnetization angle,

$$\phi' = \left( \phi - \frac{|\phi_{\frac{d}{2}} - \phi_{-\frac{d}{2}}|}{2} \right) \frac{180}{|\phi_{\frac{d}{2}} - \phi_{-\frac{d}{2}}|}, \quad (5.8)$$

with  $\phi$  being the magnetization angle measured relative to the direction of the easy axis and  $|\phi_{\frac{d}{2}} - \phi_{-\frac{d}{2}}|$  being the change in magnetization angle between magnetic domains



measured far from the domain wall.

The variation of each of these domain wall widths with temperature is shown in Fig. 5.12. In all cases, the scaling is most strongly dominated by the change in  $K_{me}$  which has an inversely proportional change in the magnetic domain wall width. The result is a profile that shows the opposite temperature scaling to that shown in Fig. 5.9, with the very extremes of the measured temperatures (77 K, 417 K) displaying the largest values of domain wall width. The charged domain wall structures show the largest absolute change in DWW, representing something that would in principle be easier to measure using a high-resolution technique such as photo-emission electron microscopy to probe the domain wall profile.

Differences resulting from the different magnetoelastic configurations become apparent only at the temperature extremes with changes in all uncharged configurations being extremely small, on the order of a few nanometers of difference, while the difference between the 60C and 120C is on the order of 50nm at the largest. The differences at these extremes stem only from the change in angle between the easy axes, indicating that the charged domain wall width could be a useful way of measuring the two distinct states.

## 5.6 Summary

In summary, in this chapter I have studied the temperature dependence of BaTiO<sub>3</sub>(111)/CoFeB heterostructures using SQUID-VSM and Kerr microscopy and determined the change in magnetoelastic anisotropy as a result of temperature-dependent strain transfer. Strong coupling between the substrate and thin film is observed at all temperatures below the ferroelectric Curie temperature, with the local anisotropy varying as the lattice parameters of the BaTiO<sub>3</sub> change with temperature. The absolute changes in the magnetoelastic anisotropy either side of room temperature are approximately equal, and so this presents two routes by which its magnitude could be changed in a device. Following this, micromagnetic simulations were performed informed by the previous experiments to determine how this dependence dominates the domain wall width of magnetic domains. These domain wall widths were found to be most strongly dependent on the magnetoelastic anisotropy, with the low-anisotropy charged domain walls showing a large difference in domain wall widths between the 60° and 120° anisotropy rotation states - a result purely of the difference in anisotropy configuration and res-

ulting wall angles of the magnetic domain wall structure.

These measurements demonstrate two distinct regions of interest around the **R-O** and **O-T** phase transitions with the low-temperature results showing step-wise changes in the magnitude of the anisotropy, and high-temperature results demonstrating a drop off as the polar ordering weakens. Both routes to manipulating the magnetic anisotropy lead to similar absolute changes in the magnitude of the anisotropy. Control of magnetoelastic anisotropy is fundamental to devices based on multiferroic heterostructures. The anisotropy tuning that is shown here will be useful for future devices based on BaTiO<sub>3</sub>(111).

---

# CHAPTER 6

---

Effect of Magnetoelastic Anisotropy Angle on  
Magnetic Domain Walls

## 6.1 Introduction

In the previous two chapters, I have introduced the concept of magnetoelastically pinned magnetic domain walls in which the magnetic domain wall is held in place with the magnetization on either side pinned strongly to the underlying direction of magnetoelastic anisotropy. In the results presented, there have been two magnetoelastic states where the magnetoelastic anisotropy (lattice elongation) rotates by either  $60^\circ$  or  $120^\circ$  through the angle of the ferromagnetic (ferroelectric) domain wall. This led to the two states (and four domain walls) exhibiting different behaviour that resulted purely from the difference in the magnetoelastic angle of the underlying structure: the field-dependent reduction of domain wall width seen at the end of Chapter 4 in Fig. 4.12, and the difference in domain wall widths at the high and low-temperature extremes in Chapter 5 in Fig. 5.12.

To understand this, I have investigated the effect of the underlying magnetoelastic anisotropy angle on the properties of magnetic domain walls. This was done using MuMax<sup>3</sup>, as in the previous chapters, as there has been good agreement so far between the predicted results of a micromagnetic framework and the observed results.

The chapter will first explore the impact on domain wall width, which has been of interest in previous chapters, considering the effect in both the relaxed case as well as an applied-field scenario in which the domain wall width is reduced. Then the effect of different micromagnetic parameters on the domain wall structure will be explored, including the effect of an interfacial Dzyaloshinskii-Moriya interaction which has not previously been considered but which is not incompatible with these structures if the film remains sufficiently thin. Finally, the effect of the magnetoelastic anisotropy angle on the AC-driven resonant frequency of the domain wall will be presented.

## 6.2 Domain Wall Structure

First, we begin by defining an ‘anisotropy angle’,  $\theta_A$ , defined as the angle between each of the magnetoelastic anisotropy axes and the domain wall length - essentially half of the previously defined angles for the domain wall types explored in earlier chapters. For the  $60^\circ$ ,  $90^\circ$  and  $120^\circ$  configurations, the anisotropy angle will be  $30^\circ$ ,  $45^\circ$ , and  $60^\circ$ . These correspond to previously measured values of  $\theta_A$  in BTO-based heterostructures which are practical at the current time to take advantage of.

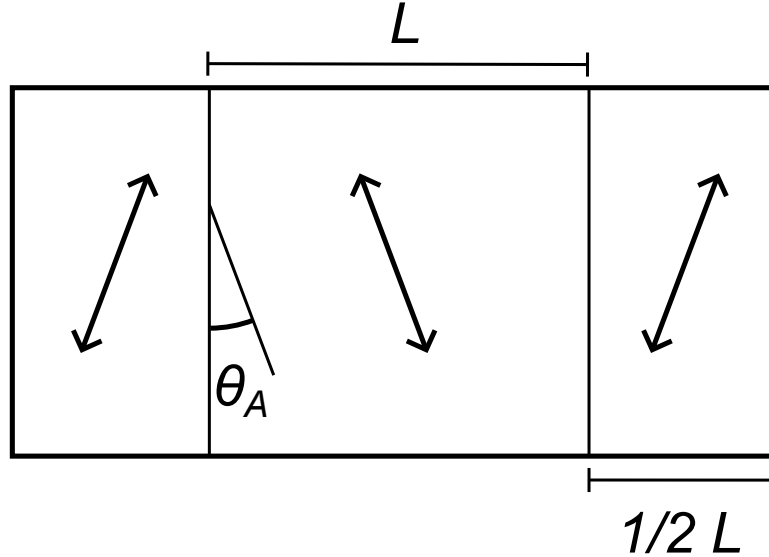


Figure 6.1: Schematic diagram of the micromagnetic setup used for this chapter. The angle indicated,  $\theta_A$ , defines the orientation of the easy axis to the domain wall. Double-headed arrows show the easy axis in each of the stripes.

These simulations will not be restricted to only these previously observed angles. In the following simulations we will explore the range from  $10^\circ$  -  $80^\circ$ , chosen as angles of  $0^\circ$  or  $90^\circ$  correspond to no change orientation of the axes and so this sets hard upper and lower limits. While it is not unreasonable to consider these other values, they represent more of a challenge in their design. Possible routes to this could be by considering other cuts of ferroelectric substrates (including significant miscut angles), or by taking advantage of some lithography processes to introduce axial anisotropies by non-magnetoelastic means [142].

For the base micromagnetic parameters, the values obtained for room-temperature CoFeB coupled to tetragonal BaTiO<sub>3</sub> were used - corresponding to the values measured in Chapter 4 with  $M_{sat} = 854$  kA/m,  $K_{me} = 30$  kJ/m<sup>3</sup>,  $A_{ex} = 21$  pJ/m, and  $\alpha = 0.1$  to improve the simulation speed. The central stripe width is set to  $2 \mu\text{m}$  and the total simulation size is  $4 \mu\text{m} \times 2 \mu\text{m} \times 20$  nm. The orientation of the uniaxial anisotropy in each stripe is defined to alternate between vectors of  $(\sin(\theta_A), \cos(\theta_A), 0)$  and  $(\sin(\theta_A), -\cos(\theta_A), 0)$ .

The dependence on  $\theta_A$  for these initial micromagnetic parameters is shown in Fig. 6.2. In both the charged and uncharged configurations the spin rotation across the

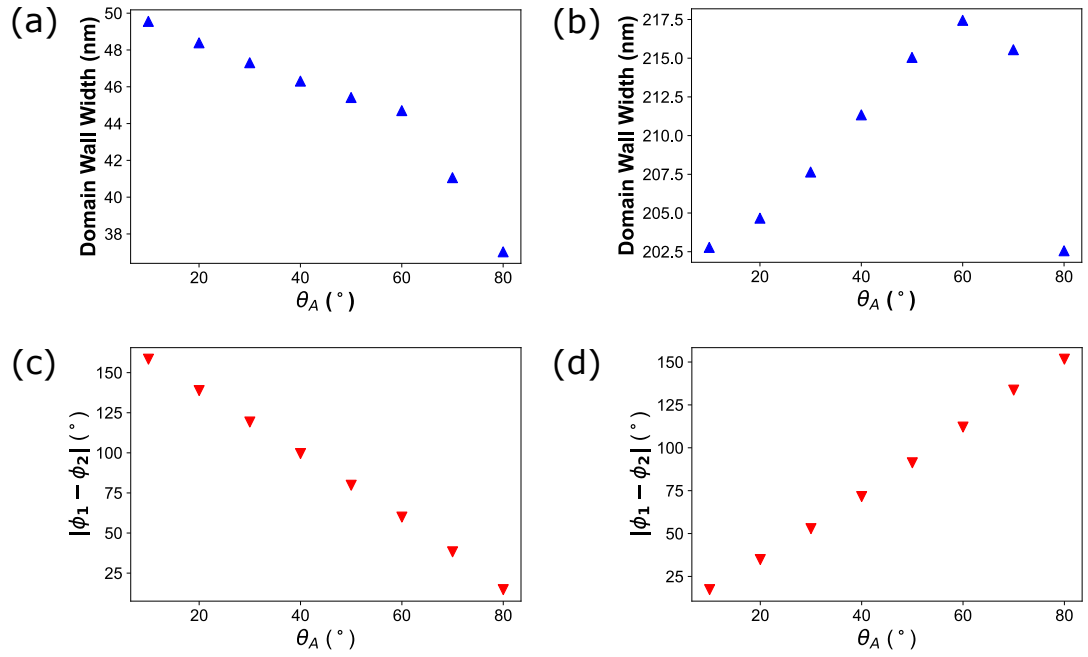


Figure 6.2: Change in the domain wall widths for the uncharged (a) and charged (b) configurations, and the corresponding spin rotation (c,d). The spin rotation remains linear, matching closely with the angle  $(180 - 2\theta_A)$  for the uncharged configurations and  $2\theta_A$  for the charged configurations.

domain wall is linear and the relationship is the opposite, with low values of  $\theta_A$  having a high rotation of magnetization in the uncharged state and a large rotation in the charged state. The corresponding domain wall width in both cases remains linear matching the change in the spin rotation until a value of  $\theta_A \approx 60^\circ$  at which point the magnitude decreases for both uncharged and charged states. It is not immediately clear why it happens at this value, but it can be understood that this represents a turning point in the balance of the micromagnetic torques resulting from the uniaxial anisotropy and the demagnetization energy. To investigate this further, we need to vary the micromagnetic parameters.

### 6.3 Applied Magnetic Field

We consider the effect of a magnetic field on the domain wall width for varying  $\theta_A$ . To investigate the magnetic field dependence, the curves from Chapter 4 were reproduced but using the same micromagnetic parameters alongside a value of  $\theta_A = 45^\circ$  corresponding to a  $90^\circ$  domain wall. The magnetic field was applied along the initializing direction of the domain wall, parallel to the domain wall for charged configurations and perpendicular for uncharged.

Shown in Fig. 6.3 is the field dependence for the three values of  $\theta_A$  corresponding to the possible, observed angles in BTO(100) and BTO(111) based multiferroics. It is immediately clear that for  $\theta_A = 45^\circ$  there is minimal difference in the scaling behaviour except for the absolute magnitude of the domain wall width - both decrease linearly with increasing applied field. This presents a special case, as in both the  $\theta_A = 30^\circ$  and  $\theta_A = 60^\circ$  situations there is a curvature that depends on the absolute magnitude of the rotation of the magnetization ('spin rotation') across the domain wall state.

With a baseline understanding this can be expanded into a phase diagram with either the domain wall width or the spin rotation as the heat-mapped parameter. This was done for a  $\theta_A$  range of  $10-80^\circ$ , as at angles of  $0^\circ$  or  $90^\circ$  there is no change in the uniaxial anisotropy in the sample, and a magnetic field range of  $5-100$  mT. A step size of  $2^\circ$  is used for the  $\theta_A$  variance, and  $1$  mT for the magnetic field. The data was then interpolated using a gaussian filter to improve the image quality. These heatmaps are shown in Fig. 6.4 for both charged and uncharged domain walls. The behaviour was revealed to be very nuanced. Within the heatmap several contours can be observed (that just so happen to match the colour map scale well) that explain some of the

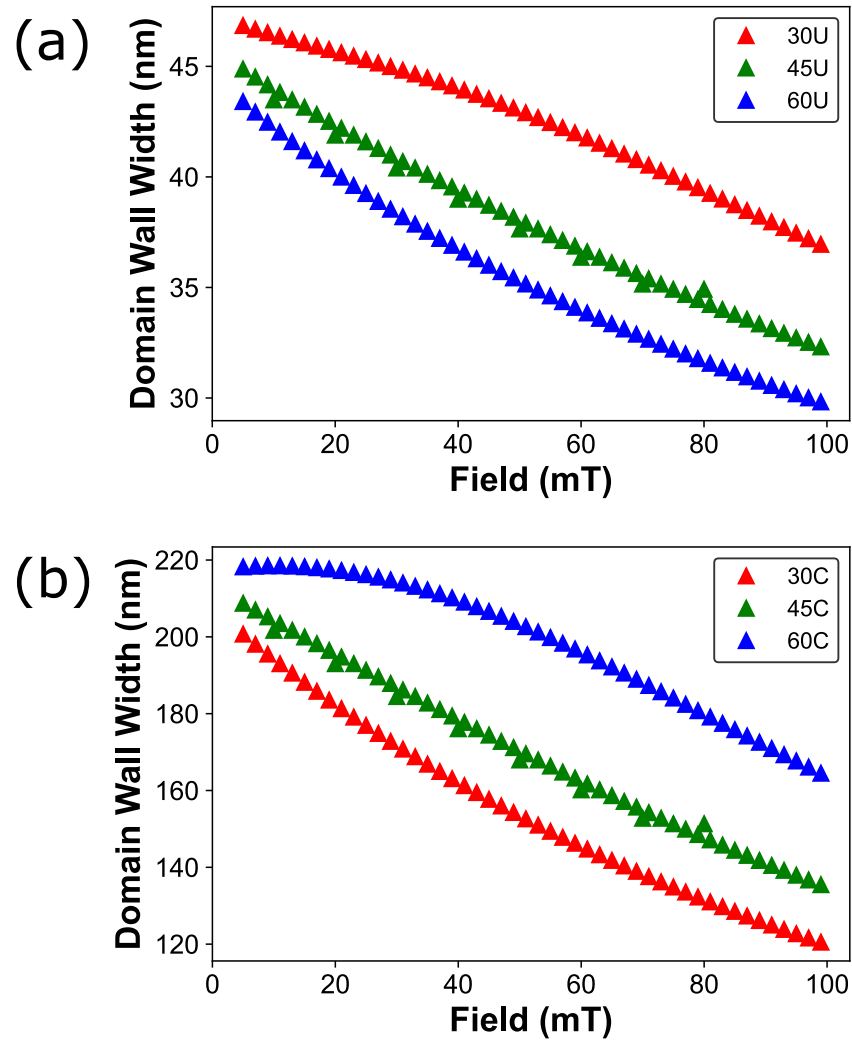


Figure 6.3: Magnetic field dependence of the domain wall width for the (a) uncharged and (b) charged domain wall states. For  $\theta_A = 45^\circ$ , the scaling is linear while for the other two cases there is some curvature that is inverted from the charged to the uncharged case.



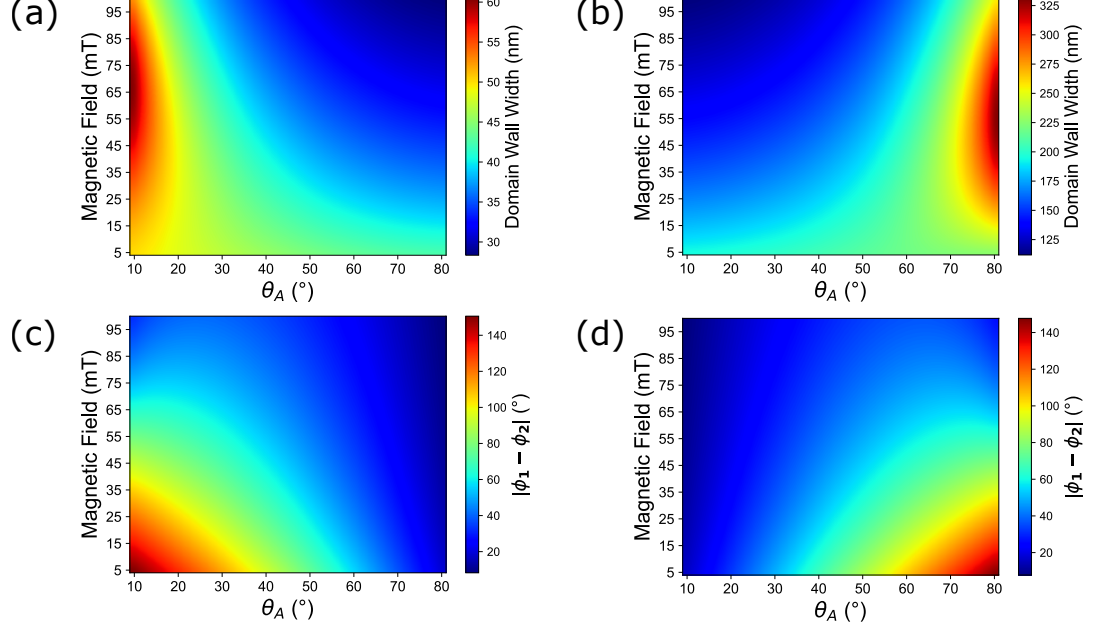


Figure 6.4: Full field-angle dependence of the domain wall width (a, b) and spin rotation (c,d) for the uncharged and charged domain wall states respectively. In both values, the charged and uncharged states appear as mirror images of each other, with some discrepancies introduced as a result of the magnetic charge accumulation at charged domain walls.

asymmetry seen in Fig. 6.3, as the three scenarios in this figure lie at different points along this contour.

To understand this we can consider the case of the uncharged domain wall under an applied magnetic field. The framework for this was introduced for the  $\theta_A = 45^\circ$  case by Baláž et al. in Ref. [143], which can be generalized to generic values of  $\theta_A$ . The application of a magnetic field leads to a torque on the magnetization,

$$\Omega_\phi = \frac{\gamma}{M_s} \left\{ -2A \frac{\partial^2 \theta}{\partial y^2} - K_u \sin[2(\theta - \theta_A)] + H_{app} \mu_0 M_s \cos(\theta) \right\}, \quad (6.1)$$

where the micromagnetic terms take on their usual meaning,  $\Omega_\phi$  is the torque acting on the magnetization, and  $H_{app}$  is the applied magnetic field strength. This leads to a change in  $\theta$  by a value of  $\zeta$  on both sides of the magnetic domain wall, with the left-hand side rotating from a value of  $\theta = \theta_A$  to  $\theta = \theta_A + \zeta$  and the right-hand side to  $\frac{\pi}{2} + \theta_A - \zeta$ . With the boundary condition of  $\partial\theta/\partial y = 0$ , this leads to the expression,

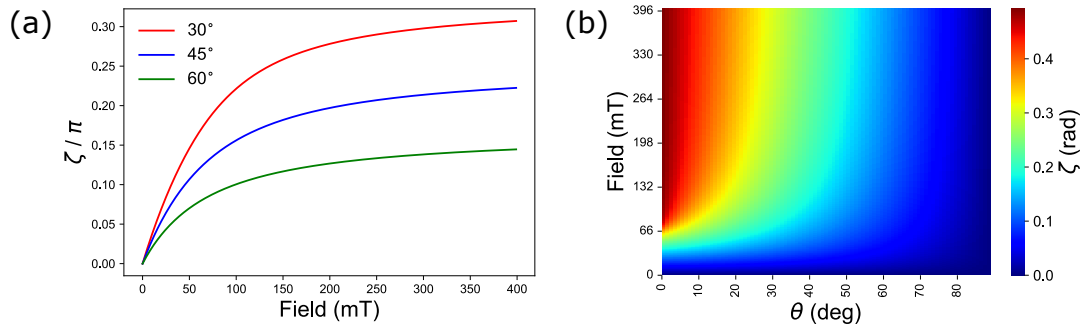


Figure 6.5: (a) Change in the field-induced magnetization deviation,  $\zeta$ , calculated numerically based on Equation 6.2 for the three realistic values of  $\theta_A$ . (b) Full field-angle phase diagram of these calculations with the rotation of magnetization,  $\zeta$ , as the ‘heat’.

$$\frac{K_u}{\mu_0 M_s} \sin(2\zeta) = H_{app} \cos(\zeta + \theta_A), \quad (6.2)$$

which we can analytically solve for a value of  $\zeta$ . This value is useful as it encompasses some balance of the other micromagnetic parameters and can be used to analytically obtain the domain wall profile (alongside a calculation of the reduced domain wall width).

In Fig. 6.5 we show the results of this calculation up to fields of 400 mT, above that which we have used in our simulations. In Fig. 6.5a) we show the individual curves for the values of  $\theta_A = 30, 45, 60^\circ$  to aid in understanding. The total reduced magnetization is  $2\theta_A - 2\zeta$  which results in a different saturating value of  $\zeta$  depending on the total spin rotation that is being suppressed by the field. In Fig. 6.5b) the heat map shows, in the same colour scheme as the previous heat maps, contouring in the magnitude of  $\zeta$  which broadly reflects the field-dependent behaviour of the spin rotation.

Through this comparison, we believe that this analytic model is a good representation of the spin-rotation driven field behaviour of the domain wall width in these magnetoelastic multiferroics. While the charged domain walls will experience some reduction in the spin rotation as a result of the demagnetizing field at the domain wall, the behaviour is still broadly a mirror image of the uncharged magnetic domain wall behaviour and so this analytic model can be used to understand the behaviour of charged domain walls also.

## 6.4 Micromagnetic parameters

The magnitude of the domain wall width will scale, approximately, as  $\delta \propto \sqrt{\frac{A}{K}}$  in all cases. For the charged domain walls there will be some scaling with the saturation magnetization as this will affect the magnitude of the magnetic charge accumulated at the domain wall, and it might be expected that a larger value of this will lead to more frustration and larger domain wall widths over which the texture relaxes. This section details the investigation of the effects of the magnetoelastic anisotropy strength, the saturation magnetization and the magnetic film thickness on the domain wall width with respect to an arbitrary magnetoelastic anisotropy angle.

The same phase diagram mapping as in the previous subsection was performed but taking the anisotropy strength (Fig. 6.6), the saturation magnetization (Fig. 6.7) and the film thickness (Fig. 6.8) as the second independent variable. As is expected from the  $1/\sqrt{K_{me}}$  dependence of the domain wall width, in both the uncharged and the charged case there is a reduction in domain wall width with increasing anisotropy strength, with the regions marked in black representing a threshold above which the domain wall is too large with respect to the stripe width and the magnetization is not sufficiently relaxed in the centre of the stripe. For the uncharged case, there is no significant dependence of the total spin rotation on the anisotropy strength. This means that small values are sufficient to reduce the wall angle at the domain wall and pin it almost exactly to the direction of the anisotropy axis.

For the charged domain walls, the spin rotation approaches the value of  $2\theta_A$ , but below  $30 \text{ kJ/m}^3$  the anisotropy strength is not sufficient to pin the magnetization to the orientation of the imprinted anisotropy axes. Below this value, we observe contouring of the spin rotation, with the shift in the contour representing a reduced rotation of the moments across the domain wall. This reduction leads to the more complex contouring of the domain wall width in the charged scenario as compared with the uncharged.

Varying the saturation magnetization in Fig. 6.7, the uncharged domain wall depends only weakly on the magnitude of the magnetic moment. The spin rotation remains constant with varied  $M_s$  and the domain wall width varies only weakly across the range of parameters observed, with the change in magnitude being dominated by the change in  $\theta_A$ .

Increasing saturation magnetization leads to larger domain wall widths in the charged domain wall situation, for all angles of  $\theta_A$ , as the accumulation of magnetic

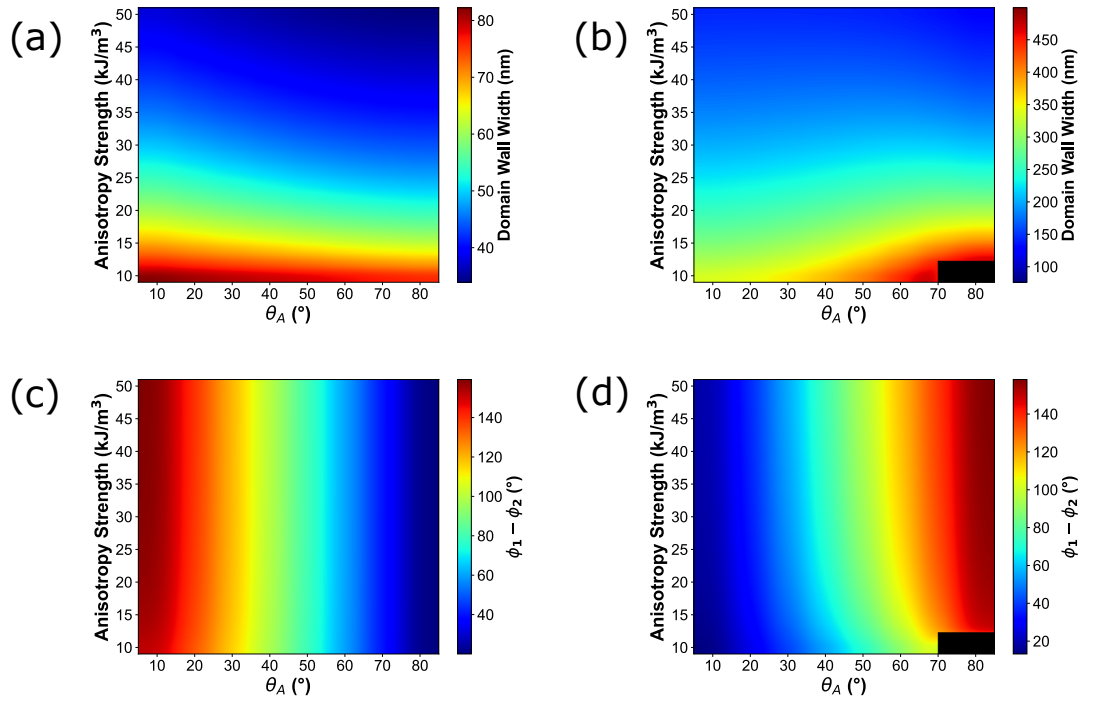


Figure 6.6: Change in the domain wall width and spin rotation with increasing anisotropy strength for the uncharged (a, c) and charged (b, d) domain wall configurations. Regions marked in black represent data points at which the domain wall becomes too large and covers most of the stripe.

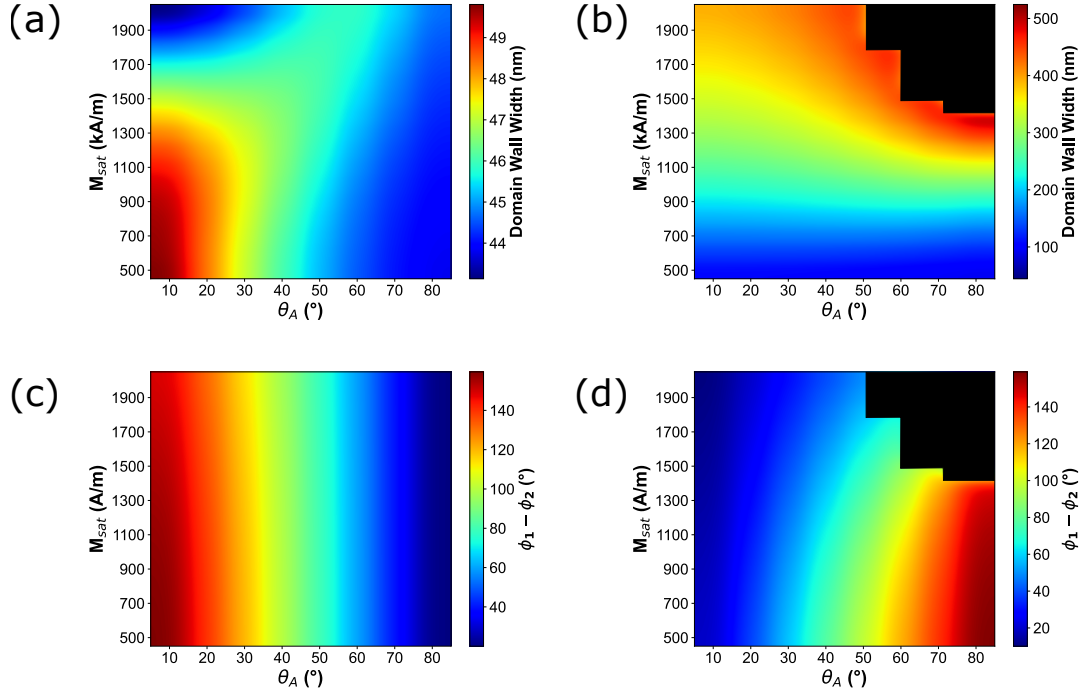


Figure 6.7: Change in the uncharged domain wall width and spin rotation with increasing saturation magnetization for the uncharged (a, c) and charged (b, d) domain wall configurations. Regions marked in black represent data points at which the domain wall did not initialize in the charged configuration.

charge necessitates larger domain wall widths to reduce the demagnetization field of the domain wall. This in part leads to a reduction of the total spin rotation at higher values of  $M_s$ . At large values of saturation magnetization and  $\theta_A$ , it becomes unfavourable to enter the charged domain wall state under the applied magnetic field which leads to the regions marked in black.

Changing the thickness results in similar behaviour as increasing the thickness has the same effect - there is a larger total moment resulting from the film and so the demagnetization field increases. The same effects on the spin rotation are observed, with the rotation for uncharged domain walls being very close to  $2\theta_A$  and the rotation for charged domain walls deviating from this with increasing film thickness which is coincidental with the increase in domain wall width.

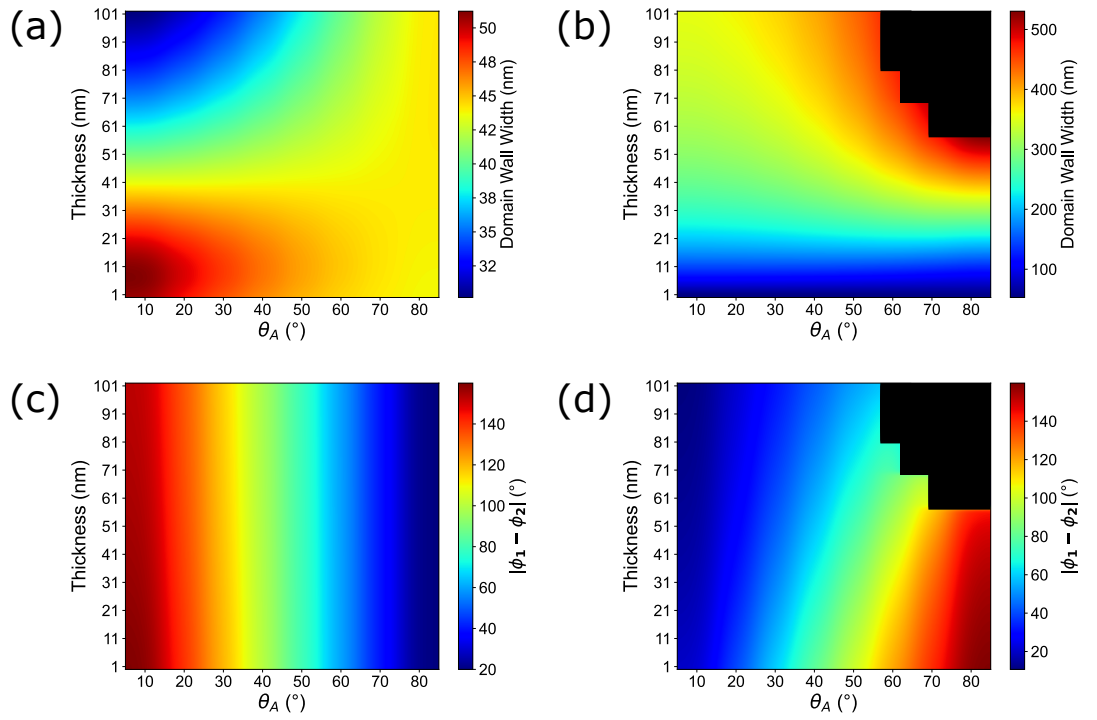


Figure 6.8: Change in the uncharged domain wall width and spin rotation with increasing film thickness for the uncharged (a, c) and charged (b, d) domain wall configurations. Regions marked in black represent data points at which the domain wall did not initialize in the charged configuration.

## 6.5 Interfacial DMI Induced Canting

Recently, in a paper by Pavel Baláz [144], the effect of an in-plane Dzyaloshinskii-Moriya interaction was considered with the  $90^\circ$  magnetic domain walls that we might expect from a BTO(100)-based heterostructure. The impact of the DMI on the domain wall profile is examined and the paper then goes on to explore the effect on theoretical pure in-plane skyrmion structures and their behaviour as they move through these systems and encounter the charged and uncharged domain walls, highlighting a potential use for such heterostructures. We choose here to focus on the effect on the domain wall profile observed. In the paper, Baláz shows that there is a canting of the magnetization out-of-plane (along the  $z$  direction) for charged domain wall structures and an up-down behaviour either side of the domain wall for uncharged domain walls that has a profile similar to a differential gaussian.

We will explore the effect of the angle on this structure. For the following simulations, the same micromagnetic parameters as in the static case were used.

From the  $m_z$  profiles, the maximum value of  $m_z$  was selected as being indicative of the canting. The effect of  $\theta_A$  on this amplitude is shown in Fig. 6.9 for a film of thickness of 1 nm (as used in the paper described earlier) and for 20 nm (as we have used in previous simulations), although we accept that an interfacial DMI of  $1 \text{ mJ/m}^2$  is not realistic for a film of this thickness. We can see from this that the uncharged domain walls are not sensitive to this change in micromagnetic conditions, essentially the product  $M_s^2 t$ , and both the magnitude and the behaviour with  $\theta_A$  are identical. For the charged case, there is a linear behaviour at a thickness of 1 nm, following well the previously observed linear regions for low  $M_{sat}$ , and a maximum around  $\theta_A = 60^\circ$  that has also been seen in the previous results.

## 6.6 Domain Wall Resonance

Another key property of interest in the concept of the resonant frequency of the domain wall. This concept was introduced by Van de Wiele et al. [145] in a micromagnetic study in which they force the elastically pinned magnetic domain walls to oscillate under a time-varying current. As with the work by Baláz discussed in the previous section, this was considered only for a  $90^\circ$  domain wall corresponding to a BTO(100)-based multiferroic. They make predictions about the resonant frequency for a model

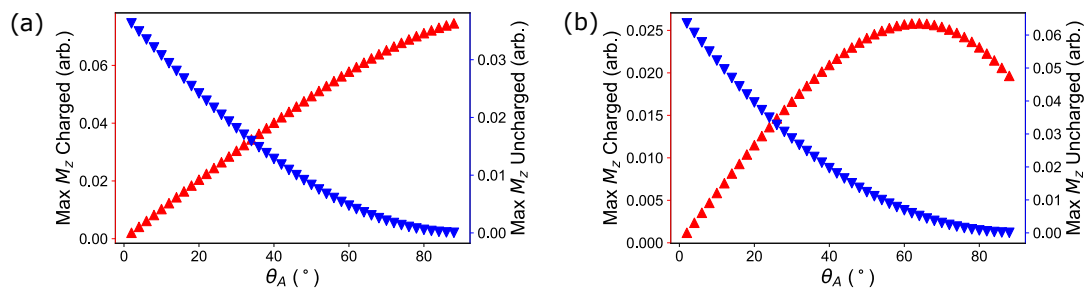


Figure 6.9: Maximum  $m_z$  vector component with varied  $\theta_A$  for an interfacial DMI of  $1 \text{ mJ/m}^2$  and a simulated film thickness of (a)  $1 \text{ nm}$ , (b)  $20 \text{ nm}$ .

structure and the spin-wave dispersion relation. This has been experimentally realized in the paper by Hämäläinen et al. [146] in which a spin-wave device based on BTO(100)-CoFe multiferroics was realized, and in the following work in the literature such as the by Qin et al. [147]. Thus, as this is interesting both from a fundamental physics point of view and a device design point of view, the effect of angle on excited domain wall resonance was examined.

In this section, we will detail the effect of an applied current and will only be concerned with the uncharged domain wall scenario. Mumax allows for current-driven behaviour through a Zhang-Li torque and is defined by the vector along which the current flows, the current density and the spin polarization of the current. Under the application of an applied pure spin-polarized current, the domain wall does not move. It is strongly bound by the spatially varying anisotropy on either side such that it is unstable far from the defect boundary that it is pinned to and will, in the first instance, snap back into position. If the domain wall is pushed off the defect by a sufficiently large current density, then this will lead to the texture collapsing and another domain wall forming at the defect. Under an oscillating current, it is possible to take advantage of this resistance to motion to lock in to the inherent frequency at which it oscillates and achieve a resonant condition. The continued motion of the domain wall in this AC state leads it to behave as a line source of magnons, with the amplitude being strongest perpendicular to the direction of the magnetization which in this case is along the  $m_z$  direction.

We are concerned here with finding what, if any, the angular dependence is. To this end, the micromagnetic parameters used in Ref. [145] were used in this study to best



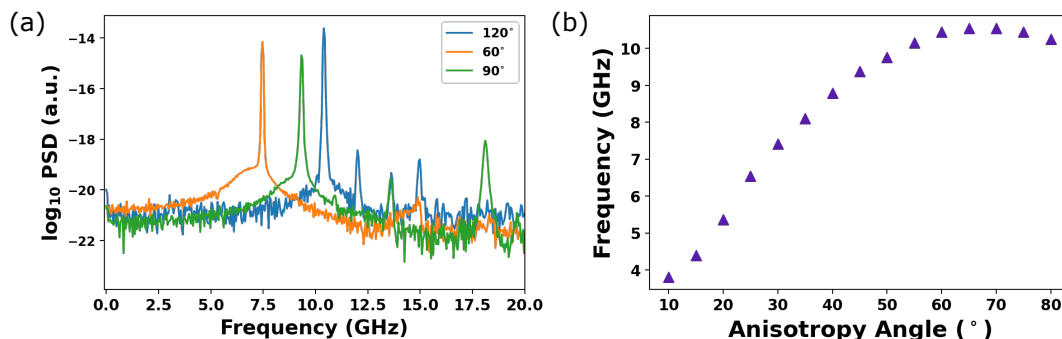


Figure 6.10: (a) Power spectrum density obtained from the relaxation of the  $m_z$  component of the magnetization for values of  $\theta_A = 30, 45, 60^\circ$ . (b) Extracted resonant frequencies as a function of  $\theta_A$ .

compare against reported results and check our observations (rather than micromagnetic parameters used in the previous sections of this chapter). The simulation is set up with the domain wall in the centre of the mesh and the edges damped by a large value of  $\alpha = 1$  such that repeated domain walls do not interact with each other. The domain wall is excited by a large pure spin-polarization current with current density  $j = 5 \times 10^{12} \text{ A/m}^2$ . The current is applied for 1 ns and the system is left to relax for 99 ns. From the time-dependent decay of the value of  $m_z$  we extract the frequency as a power spectrum density.

As before, the exact situation for the values of  $\theta_A = 30, 45, 60^\circ$  are shown in Fig. 6.10a), and the angular dependence of the peak frequency in 6.10b). The effect of changing  $\theta_A$  is significant, leading to a change of 7 GHz over the range investigated with the parameters used. As has been seen for values of the domain wall width and  $m_z$  in the previous sections, there is a maximum beyond which the frequency begins to reduce. We can expect that, like with the previous sections, the exact position of this inflexion will depend on the relative magnitudes of the micromagnetic parameters.

This will naturally have an impact on the dispersion diagrams of these domain walls. Calculation of the dispersion relation followed the methodology of Ref. [145] to produce these dispersion diagrams. An AC current with current density  $j = 1 \times 10^{12} \text{ A/m}$  is applied with an angular frequency of  $2\pi f$  where  $f$  is a frequency that is varied between 2-25 GHz and the domain wall is excited for 20 time periods, after which the final configuration is saved and used to calculate the dispersion based on the spatial

variation of  $m_z$ . A Fourier transform is performed along a line scan of the resulting final configuration and the absolute magnitude is plotted to obtain the  $f-k_x$  dispersion relation.

It is not possible to reasonably perform or show this data for all arbitrary angles of  $\theta_A$ , so the simulations were performed on three key angles: 30, 45 and 60°. These three plots are shown in Fig. 6.11. Our calculation of the dispersion relation does not perfectly replicate the accuracy and detail of the dispersion diagram presented in Fig. 4 of Ref. [145], but nonetheless, the band behaviour appears the same with a broad non-dispersion band around the resonant frequency of the domain wall and side bands that correspond to different orientations of the magnon wavevector to the local magnetization.

With increasing values of  $\theta_A$  the broad non-dispersive band increases in frequency to match the new resonant frequency of the domain wall. In addition to this, the anisotropic dispersion bands shift down in frequency and up in  $k_x$  as a result of the change in angle between the pinned magnetization and the spin wave propagation direction.

## 6.7 Conclusions

In conclusion, this chapter has detailed the investigation of the effect of the magnetoelastic anisotropy angle on the properties of both charged and uncharged magnetic domain walls. The properties of the individual domain walls have a significant dependence on the reduced domain wall angle, determined by the value of  $\theta_A$  at which the magnetization is pinned either side of the domain wall. The combined effects of micromagnetic parameters and magnetoelastic anisotropy angle on the magnitude of the domain wall width has been investigated in detail, and was found to have a complicated landscape that depends heavily on the balance of relative energy terms. This is similarly reflected in the other two cases considered, that of canted moments at the domain wall and resonant behaviour of the domain wall under applied AC currents.

This difference between the underlying magnetoelastic anisotropy angle presents an additional factor to consider when designing devices in these heterostructures, as optimizing around the value of  $\theta_A$  used will be important. For example, in structures based on BTO(111) substrates, it will be ideal to select parameters such that the maximum lies at values of either  $\theta_A = 30^\circ$  or  $\theta_A = 60^\circ$  to best contrast the two available

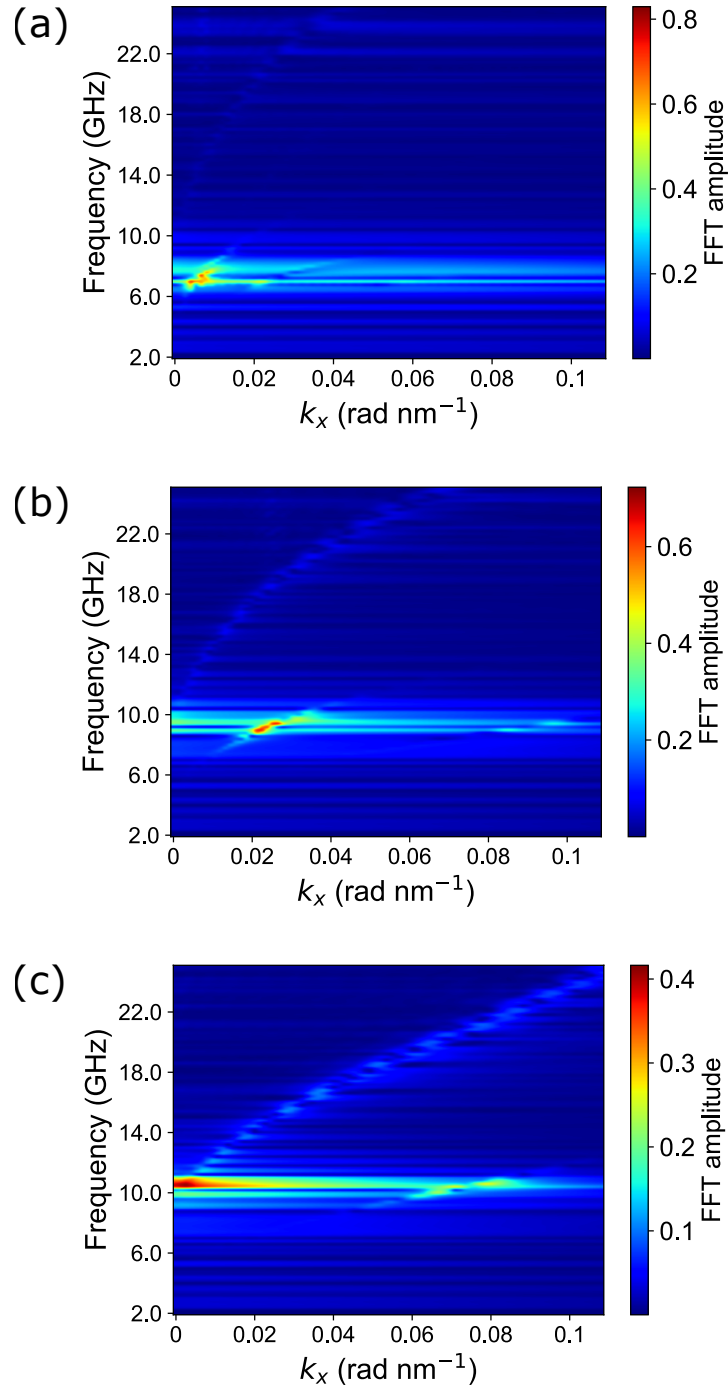


Figure 6.11: Dispersion diagrams for magnetic domain walls with (a)  $\theta_A = 30$ , (b)  $\theta_A = 45$  and (c)  $\theta_A = 60$  excited under an AC current.

domain states.

---

# CHAPTER 7

---

Growth and Characterization of BiFeO<sub>3</sub> thin  
films

## 7.1 Introduction

This chapter will detail the growth and characterization of BiFeO<sub>3</sub> thin films. The goal here is to obtain a single-phase thin-film multiferroic which can then be used as a voltage-controlled element in a more complex material stack incorporating ferromagnetic materials. Compared to the previous chapters, the motivation is to increase the complexity of our artificial multiferroics through the addition of an antiferromagnetic component of the ferroelectric which allows for an additional degree of control over the ferromagnetic layer through exchange bias that results from coupling between antiferromagnetic and ferromagnetic phases.

Based on work in the literature, we choose to investigate this using SrTiO<sub>3</sub> (STO) as a substrate. The lattice constant of STO is 3.905 Å, which is a close match to the lattice constant of BFO as compared with other commercially available substrates on which BFO has previously been grown.

The long-term goal is to use this BFO layer as a voltage-controlled element in a thin film stack and so to apply the voltage a back electrode is required. For this we choose to grow a SrRuO<sub>3</sub> (SRO) buffer layer as it is a conducting perovskite with lattice constant between STO and BFO which means it will also act to mediate the strain between the substrate and the BFO film.

We will begin by first growing single layers of SRO to verify the epitaxial quality of the buffer layer and ensure that we are growing as close to an ideal surface as is reasonably possible. Then, we shall investigate the growth of the SRO/BFO bilayer materials and how the film quality changes with different deposition conditions.

In this chapter, work attributable to the author was all sample depositions, sample optimization, RHEED characterization, X-ray characterization, AFM characterization, and analysis of the data. The bismuth ferrite target was sintered by Y. Ji. Data fitting of x-ray reflectivity data for the SrRuO<sub>3</sub> dataset was supported by L. Oliver. PNR experiments were performed at the POLREF instrument at ISIS with the assistance of C. Kinane. Fitting of PNR data was aided by C. Kinane and D. Roe.

## 7.2 Substrate Characterization

We first verify the quality of the substrate we used for these experiments. In the following experiments, all growths are performed using STO(100) substrates, the gen-

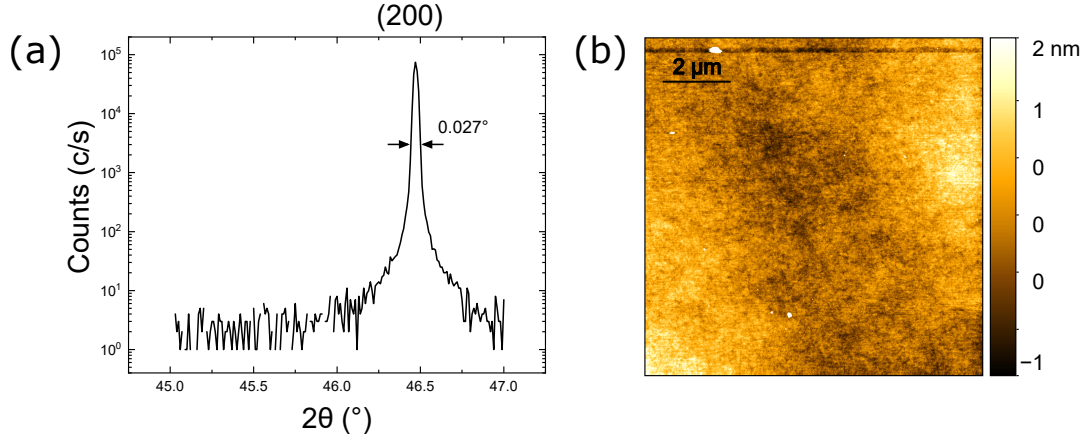


Figure 7.1: Substrate quality measured by a) XRD around the (200) peak and b) AFM for a single-side polished STO(100) substrate.

eral quality of which will be detailed here. Substrates are single-side polished with dimensions of 10x10x0.5 mm, purchased from Pi-Kem.

The substrate quality can be evaluated by two factors: the single crystal quality, measured from the FWHM of the Bragg peaks, and the surface topography. From the Scherrer equation, the FWHM can be linked directly to the single crystal quality with a larger grain size resulting in a narrower peak and a reduced FWHM. To examine this, the (200) Bragg reflection is chosen as simulations of the expected peak intensities puts this at the highest intensity (and indeed this is the case in reality). A typical (200) substrate peak at  $2\theta = 46.47^\circ$  is shown in Fig. 7.1a), where the FWHM is measured to be  $0.027^\circ$  by fitting a Gaussian function to the peak. This corresponds to a grain size on the order of 400 nm. The quoted values of the lattice parameter for STO is  $3.905 \text{ \AA}$ , and our measurements give values of either  $3.90 \text{ \AA}$  (from the (200) peak) or  $3.91 \text{ \AA}$  (from the (100) peak) with a  $0.01 \text{ } 2\theta$  angular resolution, which we take to be in good agreement with this value.

An AFM scan of the substrate surface is shown in Fig. 7.1(b), and depicts the typical as-received surface quality of the  $\text{SrTiO}_3(100)$  substrates. The surface is smooth and lacks any particular surface topography, with an RMS roughness on the order of 600 pm, although some variance is expected particularly between individual batches of substrates. Visible in the image are several dust particles that are much taller than other features on the surface, most likely dust or other contamination. This presents a

problem with the pre-characterization of substrates - doing so introduces the possibility for dust and other contaminants to settle on the surface, even with measures in place to control and limit exposure.

In the literature, it was shown that the ideal surface to grow SrRuO<sub>3</sub> on is that of a substrate with large terraces with step-edges of one lattice constant, obtained by a combination of chemical etching and annealing treatments to the substrate [148, 149]. However, good quality SRO has been grown without this treatment [150] and so we will also grow without it onto pristine substrates of the quality described here.

### 7.3 Growth of SrRuO<sub>3</sub>

Strontium ruthenate (SRO) is a conducting oxide material with a lattice constant close to that of SrTiO<sub>3</sub> that has been shown to lattice match the 3.905 Å of STO [151]. There is a wealth of literature [152–154] that has similar optimized deposition conditions for SRO - where possible we aim to keep these consistent with previous reports. We expect that temperature and laser fluence will vary somewhat, depending on the nuances of each individual deposition system, but oxygen pressure is likely to be very reproducible and so this is fixed at 0.13 mbar. Likewise, the target-substrate distance is fixed at 55 mm and the repetition rate is fixed at 10 Hz. Ablation was performed on a 2” target of SrRuO<sub>3</sub> with the correct stoichiometry obtained from Pi-Kem.

#### 7.3.1 X-ray characterization

As primary characterization techniques, we use X-ray reflectivity and X-ray diffraction to infer the properties of the deposited thin films. An example data set for both techniques is shown in Fig. 7.2. In the reflectivity data, the fitting is performed using GenX [103] with a model where STO is the substrate and SRO is a single layer on top. The densities remain fixed and the layer thickness, layer roughness, and substrate roughness are varied to obtain the best fit to the data. In the diffraction data, the largest peak to the left of the substrate peak is the principle (001) reflection of the SRO layer and the satellite peaks correspond to Pendellösung fringes which are indicative of high crystalline quality [155]. To obtain structural information from the XRD peak we fit a Gaussian function to obtain the central position and the full width at half maximum.

To determine the optimum growth conditions for SRO we vary the temperature



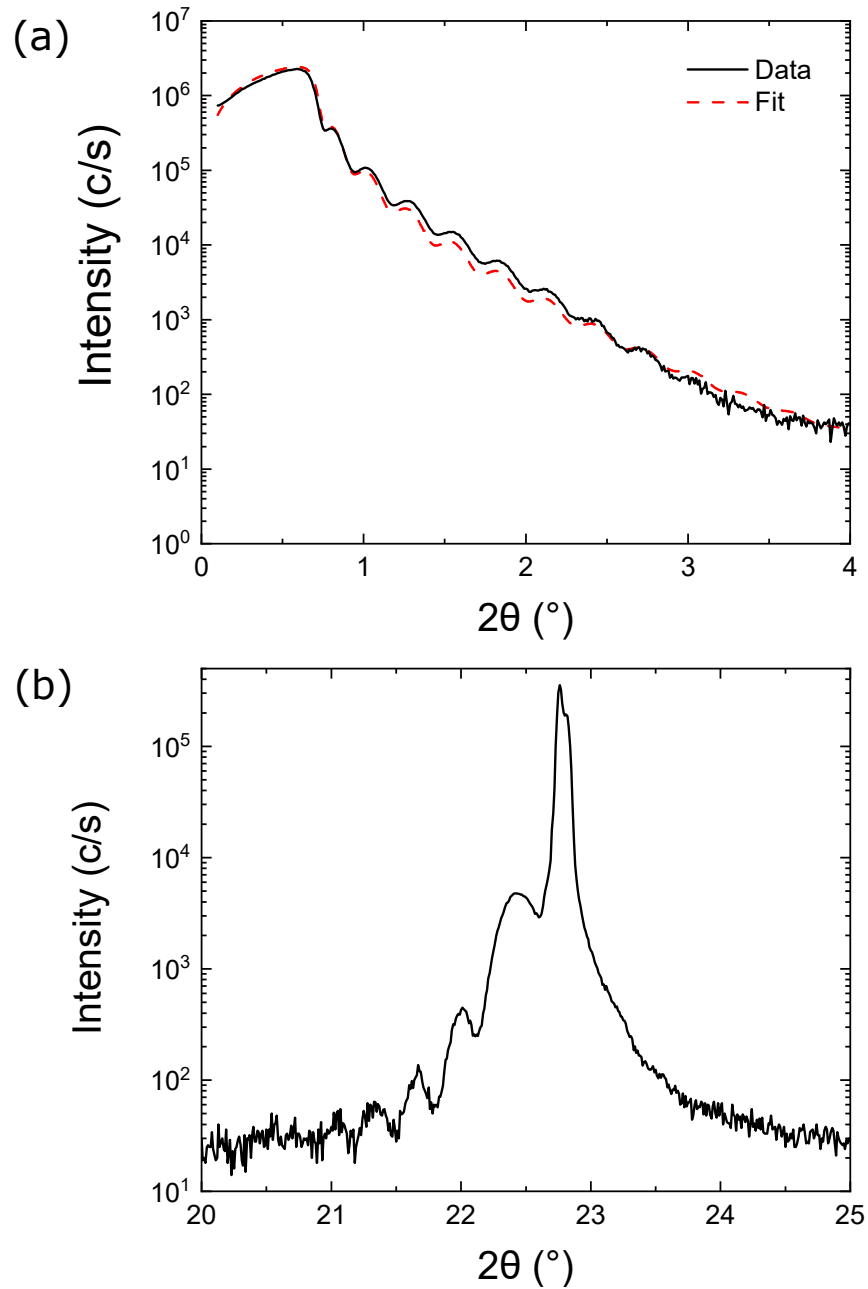


Figure 7.2: (a) X-ray reflectivity curve and (b) X-ray diffraction around the (100) substrate peak obtained from a 28 nm SRO film grown onto STO with a substrate temperature of 700 °C and fluence of 1.05 J/cm<sup>2</sup>. The fit in (a) is obtained using GenX.

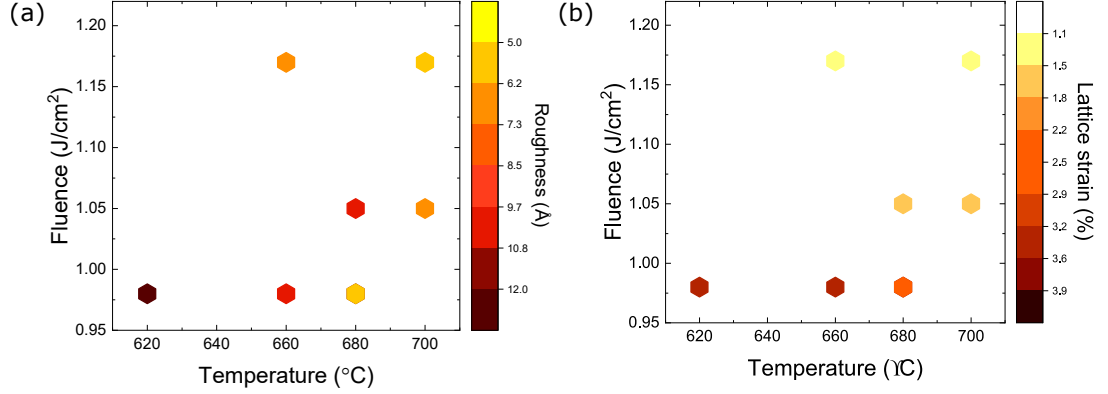


Figure 7.3: Temperature-Fluence phase diagrams for trends in (a) film roughness and (b) film strain obtained from XRR and XRD respectively. Lattice strain is calculated relative to the substrate.

between 620 - 700 °C and the laser fluence between 0.96 - 1.17 J/cm<sup>2</sup> (the bounds that were feasible at the time of the study). As we are primarily interested in this film as a buffer layer, we are optimizing for two conditions: film roughness, and lattice strain, with smoother and less strained films being ideal. Both of these are shown in Fig. 7.3. Film roughness is obtained from fitting using GenX using a simple monolayer model which, from Fig. 7.2a), may not be the most accurate model of the film structure. However, introducing additional complexity may obfuscate the results and the figure of merit for the fit does not significantly change within a 0.1Å variation of the roughness.

We can easily understand the trends at a glance. With increasing temperature and fluence the film quality increases, providing a smoother and less-strained surface on which to grow our BFO layer; from this dataset alone, we would select an ideal set of parameters to be a deposition temperature of 700 °C and a fluence of 1.17 J/cm<sup>2</sup>. However, there is some variation of the film thicknesses as a result of the change in fluence, so we need more information to draw a definitive conclusion. To interrogate this in more detail a local measurement of the surface quality is needed and will be detailed later in this chapter.

### 7.3.2 AFM Characterization

Fig. 7.4 shows the variation in surface structure obtained via AFM of the films grown at 680 °C. From the images, we can see that the SRO primarily forms as islands on

### 7.3 Growth of SrRuO<sub>3</sub>

Sample ID	$T$ (°C)	$f$ (J/cm <sup>2</sup> )	Pulses (k#)	Thickness (Å)	Roughness (Å)
PLD20220727	660	0.97	40	238	10.7
PLD20220728	620	0.97	40	160	18.6
PLD20220803	680	0.97	40	450	9.8
PLD20220824	680	1.05	10	225	10.5
PLD20220901	680	1.17	10	261	5.6
PLD20221017	700	1.13	10	282	5.7
PLD20221019	660	1.17	10	276	7.3
PLD20221021	700	1.13	12	280	6.3

Table 7.1: Sample parameters and fitting outputs (thickness, roughness) for XRR measurements modelled with GenX.

the surface and then the primary growth mode must be the accumulation of islands into complete layers, with the growth at  $f = 1.05$  J/cm<sup>2</sup> showing the least peak-to-trough variation with the layer appearing mostly complete (judged by a higher density of ‘holes’ than ‘islands’). The mode of growth does not change significantly over this range, and so we attribute the change in roughness to changes in thickness primarily.

The variation with temperature is shown in Fig. 7.5, for a deposition fluence of  $f = 0.98$  J/cm<sup>2</sup>. As the temperature decreases, the density of islands increases with the film grown at 620 °C showing a large variation in the topographic height. This is evidence that points to temperatures below 660 °C being insufficient to allow the islands to naturally coalesce into layers.

The ideal surface is obtained for deposition conditions of  $T = 700$  °C and  $f = 1.05$  J/cm<sup>2</sup> and is shown in more detail in Fig. 7.6. The SRO film grown under these conditions displays terracing with step heights of approximately 3 Å, which does not perfectly match the expected 4 Å, but is sufficient to say that this is on the order of one atomic layer. It is for this reason that a deposition fluence of  $f = 1.05$  J/cm<sup>2</sup> is chosen as ideal rather than the  $f = 1.17$  J/cm<sup>2</sup> that would be chosen from the XRR and XRD analysis alone.

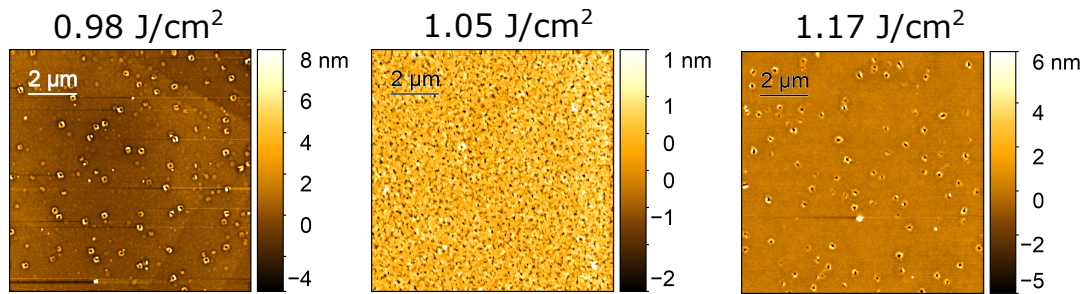


Figure 7.4: AFM scans of SRO layers grown at three different fluences in the range 0.98-1.17 J/cm<sup>2</sup> with a deposition temperature of 680 °C. The topographic character remains the same with islands visible on the surface for each fluence.

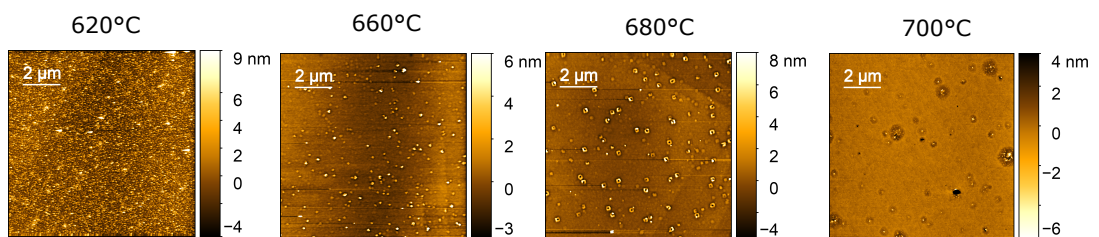


Figure 7.5: AFM scans of SRO layers grown at different temperatures in the range 620 - 700 °C with a constant deposition fluence of  $f = 0.98$  J/cm<sup>2</sup>. The surface quality changes significantly, with terrace structures becoming visible at 700 °C.

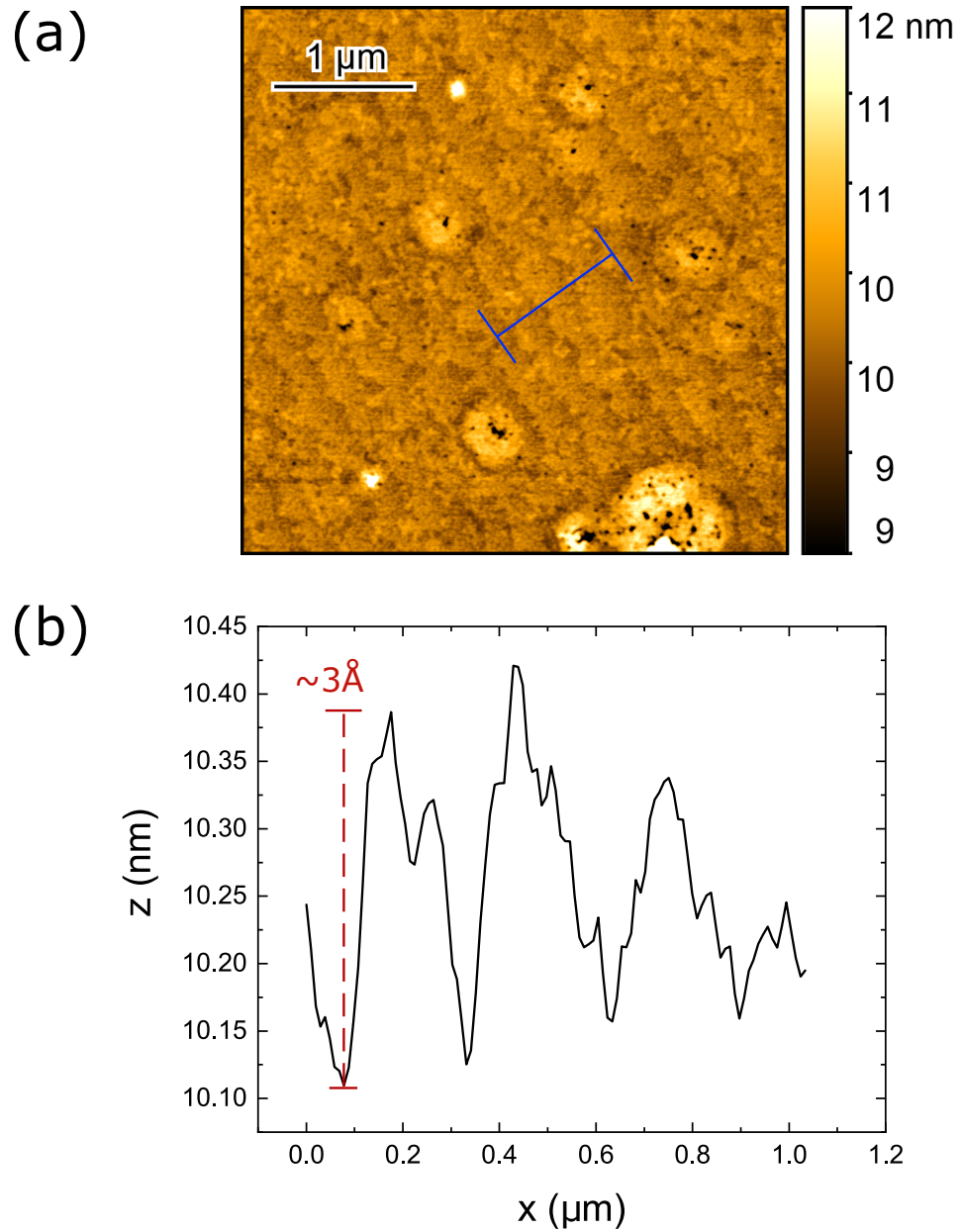


Figure 7.6: (a) AFM scan of an SRO film grown at  $T = 700 \text{ }^\circ\text{C}$  with  $f = 1.05 \text{ J/cm}^2$ . (b) Linescan taken along the region indicated in blue in (a), with the ticks representing the width of the data taken. The peak-to-trough height (step height) is on the order of  $3 \text{ \AA}$ . Large particles are dust contaminants on the substrate prior to deposition.

### 7.3.3 RHEED characterization

Here I will detail the characterization of the SRO growth and how it correlates to the film quality observed in the previous two sections, focusing on the time-dependence of the RHEED intensity during growth.

In theory, the film thickness can be well controlled with the in-situ RHEED giving an estimate of the growth rate and, with careful calibration and comparison to film thicknesses measured after growth, an immediate knowledge of the current growth rate. However, this relies on the parameters already being close to optimal to obtain RHEED oscillations corresponding to monolayer growth in a layer-by-layer growth mode, where adatoms land on the surface and preferentially complete a monolayer before nucleating the next monolayer on top. In this growth mode, the RHEED intensity change due to surface roughness is really due to the formation and completion of individual monolayers. Without this, it is difficult to gauge the growth rate in real time if multiple monolayers are forming and completing at the same time.

Example changes in intensity are shown in Fig. 7.7 for samples in which the deposition temperature is varied. In all cases, it was possible to observe some damped oscillation at the beginning of the growth which like corresponds to a layer-by-layer growth with island formation that, in the case of (a) and (b) leads to a steady-state growth mode in which the roughness remains similar throughout and no significant changes in the intensity were observed as layers likely nucleate and complete at similar rates. At the optimized deposition temperature, however, it was possible to observe a recovery of the overall RHEED intensity accompanied by RHEED oscillations late into the growth which, alongside the AFM images presented previously, is indicative of a growth mode in which atomic terraces form and layers are completed by the step-flow of these atomic terraces.

This is not necessarily the same as what might be expected from the literature. Reports on the ideal growth of SRO on STO typically use higher fluences, in the range of 1.5 - 2 J/cm<sup>2</sup> and report an initial layer-by-layer growth mode (as our experiments have observed) that then gives way to a steady step density (SSD) change in the surface [152]. While we have observed this in temperatures that are below 700 °C, this was not the case at the ideal temperature.

To investigate this in more detail we grew a comparable SRO film with a higher fluence of  $f = 1.5 \text{ J/cm}^2$ . The change in RHEED intensity over the course of the

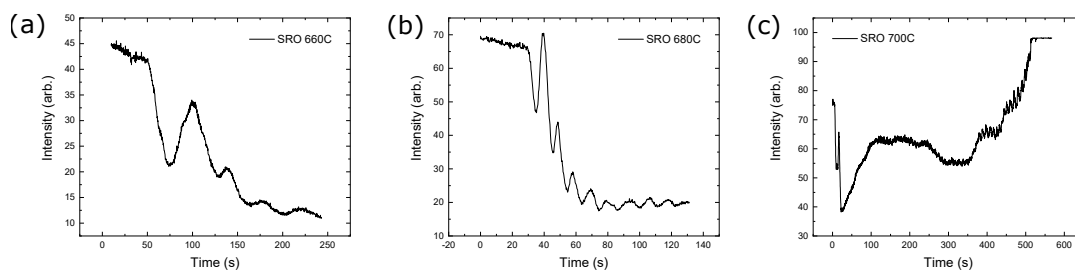


Figure 7.7: RHEED signal taken during deposition of SrRuO<sub>3</sub> layers at a) 660 °C, b) 680 °C, and c) 700 °C. All show signs of layer formation and increasing roughness at the initial stages of deposition. For the 660 and 680 the recovery of layer-by-layer growth shown in c) is not obtained.

growth is shown in Fig. 7.8. The start of the growth initially has an oscillation period of approximately 15 s, (suggesting a rate of 0.27 Å/s for a 4 Å layer thickness), but as the growth proceeds a 90s oscillation period dominates the change in RHEED intensity which would suggest a 0.044 Å/s growth rate. While this fluence is below the  $f = 2.5$  J/cm<sup>2</sup> used in the paper previously cited, it is clearly sufficiently large that there is a change in the growth mode. Also contrary to the results of this paper, they state that if the growth is interrupted at any point and left to anneal for a sufficient time (they suggest above 4 minutes), then a layer-by-layer growth mode should be obtained upon continued deposition. Our results did not show this to be the case. While there was also some time-dependent change in intensity after the deposition is interrupted, continued deposition only showed oscillations with 90 s periods corresponding to the SSD growth mode. This implies that there is a fluence-dependence of this growth mode control that was not been reported in the paper of Bachelet et al. in Ref. [152]. However, it is not possible to disentangle this from a rate-dependent growth transition, as the change in growth rate is significant between the two growths presented, with a calibrated growth rate of 0.27 Å/s for the sample grown at a fluence of 1.5 J/cm<sup>2</sup> and a rate of 0.12 Å/s for the sample grown at 1.05 J/cm<sup>2</sup>.

## 7.4 Growth of BiFeO<sub>3</sub>

With the optimized recipe for SRO, I move on to detailing the growth of the bismuth ferrite layer. Unless explicitly stated otherwise, the optimal growth conditions for the

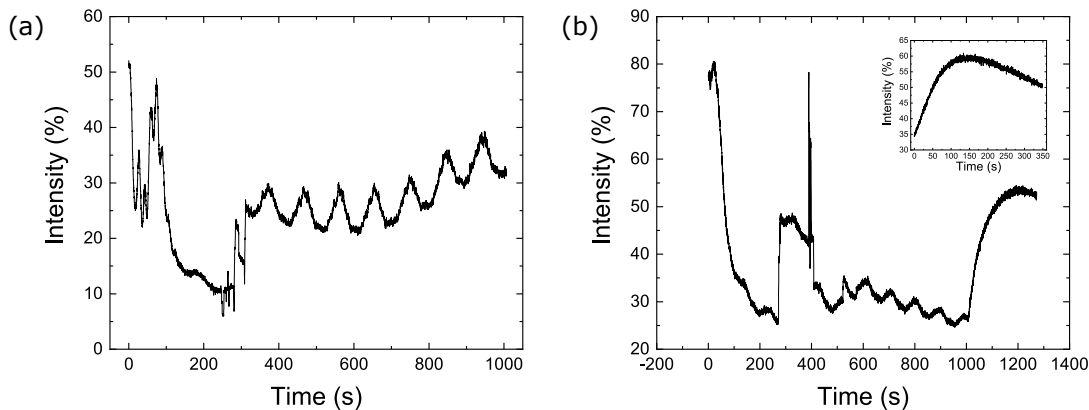


Figure 7.8: (a) RHEED intensity for the first 10,000 pulses of an SRO layer grown at  $T = 700$  °C and  $f = 1.5$  J/cm<sup>2</sup>. The RHEED oscillations have a period of 15 s up to about 120s, and then a period of 90 s from 330 s onwards. (b) The following 10,000 pulses grown after a 5 minute anneal, with the intensity change during the anneal shown in the inset. Sharp jumps correspond to a realignment of the electron optics.

SRO layer found previously were used with a deposition temperature of 700°C and fluence of 1.05 J/cm<sup>2</sup>.

We deposit from a homemade BiFeO<sub>3</sub> target with a 10% excess of Bi to account for the volatility during deposition. The goal is to obtain an ideal film surface, such as the one shown in Fig. 7.9 taken from Ref. [153] at which point it can be said that the recipe is well-optimized for our purposes. Because the effects observed in the literature can be quite small in some instances, with coercivity enhancements and exchange biases in the order of 10s of Oe, a smooth film is desirable as it would make the interpretation of results clearer without having to be concerned about roughness effects such as orange peel coupling [156].

The goal is to obtain an ideal bismuth ferrite surface with atomic terraces based upon the reports of literature, an example of which can be seen in Fig. 7.9 reproduced from the work of Jiang et al. [153].

#### 7.4.1 Deposition Temperature

We first investigate the effect of deposition temperature, using the optimal SRO recipe of  $T = 700$  °C and  $f = 1.05$  J/cm<sup>2</sup> at which we were able to obtain terraced struc-



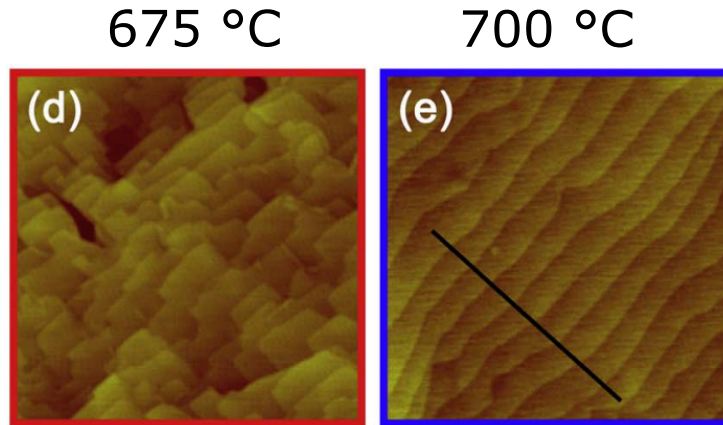


Figure 7.9: Optimized BFO surfaces grown on STO/SRO reproduced from Fig. 3 of Ref. [153]. Temperatures are indicated above each image.

tures. Substrates are placed into the substrate holders with no cleaning steps and the assumption is made that the substrate is relatively contaminant-free which is backed up by taking RHEED images of the surface. The repetition rate for the BFO is kept fixed at 5 Hz.

The deposition temperature is varied between 660 - 760 °C, with the lower band encompassing the majority of reported deposition temperatures for similar heterostructures (typically 670 - 700 °C) and the upper band being well in excess, allowing us to estimate if there is a significant substrate temperature difference based on the results. The reflectivity curves for this are shown in Fig. 7.10 in which the curves are stacked on top of each other to draw qualitative comparisons. The curve shown for  $T = 660$  °C includes sputtered metallic layers of CoFeB/Pt. It is easy to understand from this that there is a significant change in the fringe character above 720 °C in which only a single period of Kiessig fringes is observed, which would be indicative of a single layer material (or materials in which the scattering behaviour is very well matched). At and above this temperature, it becomes difficult if not impossible to fit the data well to simple models (single, double or triple layer models) and this makes it difficult to obtain information about the films. At this stage, it is not possible to understand why this is the case, but it can be said that the BFO layer is too rough to obtain a coherent XRR spectra, evidenced by the lack of nuance both expected and seen in the bilayer pattern at lower temperatures.

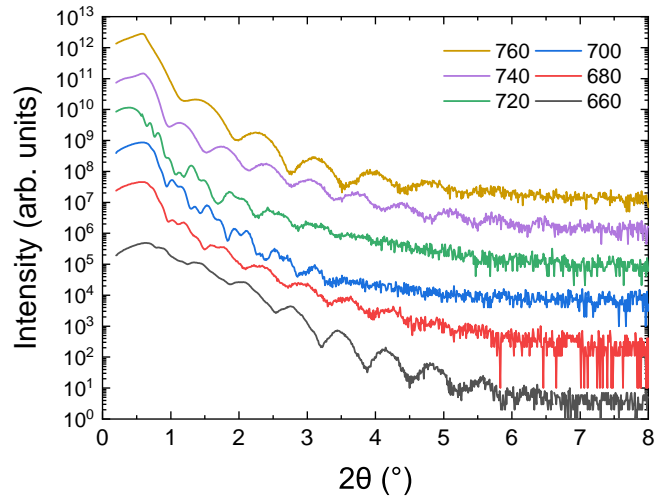


Figure 7.10: X-ray reflectivity comparison for STO/SRO/BFO films where the BFO layer has been grown at a deposition temperature varied between 660 - 760 °C. For the case of  $T = 660$ , there are additional metallic layers deposited on top of CoFeB/Pt.

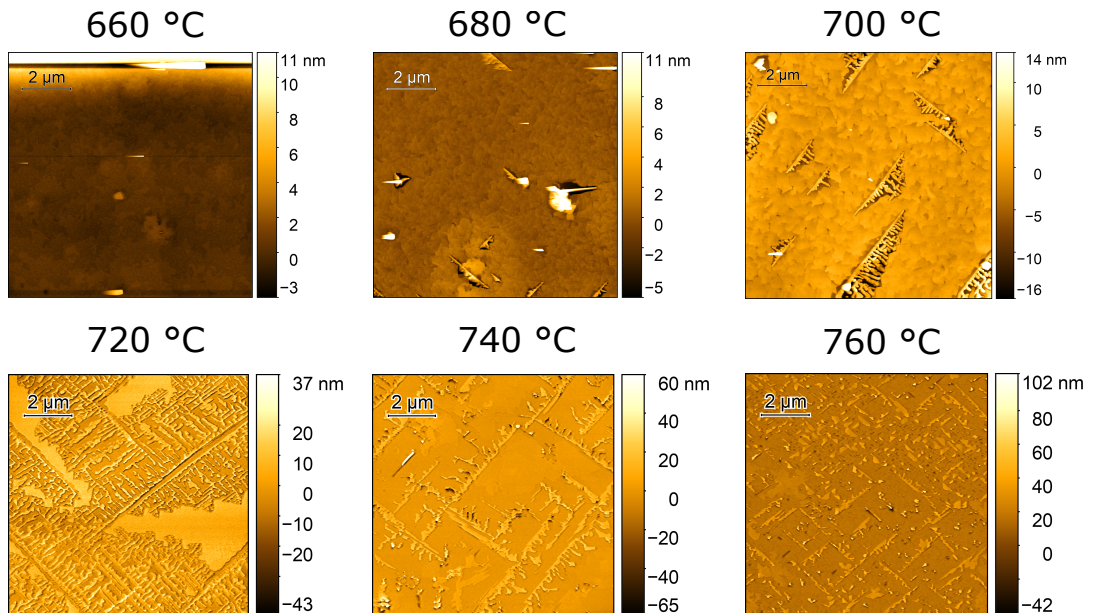


Figure 7.11: Change in surface topography of BFO layers with increasing substrate temperature in the range of 660 - 760 °C, grown onto nominally identical SRO layers underneath. Temperature is indicated above each image.

From the films that can be fitted, the rate ends up being very slow resulting in thin films on the order of 10 nm in thickness grown with a rate of 0.0125 Å/s (0.0025 Å/pulse). This means that the films are not thick enough to show any significant Bragg peaks in x-ray diffraction and so we cannot quantify film quality based on this.

The atomic force microscopy images become the most useful tool for evaluating the quality of the bismuth ferrite growth. The entire temperature range of interest is shown in Fig. 7.11. The growth is much more complex than for the SRO previously presented; instead of moving from some circular 3D islands to a terraced growth, there is a more nuanced nanostructure formation taking place. At all temperatures except for 660 °C, a tendril nanostructure begins to form during the BFO growth, potentially alongside some layer completion underneath, although this is not clear in every situation. The step height of these structures is on the order of 5 nm, except at 740 °C where there is some terracing in the structure and the total height can reach 20 nm. Higher temperatures lead to a higher preference of this formation with the step height of these features increasing with the temperature. Given that these features are on the order of or larger than the expected film thickness, it is clear that the formation of these structures becomes the primary growth mode and so with the amount of material deposited there was not a continuous layer at high temperatures making x-ray reflectivity a poor technique for measuring these films.

Interestingly, the long axis of these tendrils always forms along the (110) crystal direction - the diagonal of the substrate. If the expected polarization vector of (111) is projected onto the (001) surface then it lies along the (110)-like directions and so this may be an indicator of emerging ferroelectricity in the film under poorly optimized conditions.

Equally, nanostructured stripes on the surface were seen at high temperatures in the previously discussed work of Jiang et al. [153] and there were attributed to the Fe<sub>2</sub>O<sub>3</sub> impurity phases, with the high temperatures evaporating off the bismuth atoms and suppressing the formation of the perovskite phase. However our experiments observe these features at much lower temperatures with indication of the formation of our surface impurities beginning even at 680 °C. The character of this is also different, as the impurity stripes in their paper were square with sharp edges while ours have a more nuanced character.

From this, it was seen that between 660 - 680 °C is likely the optimal growth

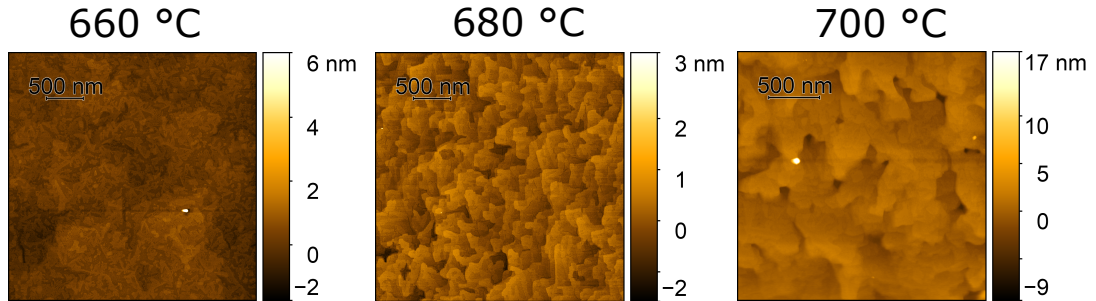


Figure 7.12: Zoomed-in AFM scans of the same regions from Fig. 7.11, with the region chosen to be away from the (110) oriented nanostructures for the 680 °C and 700 °C scans. Temperature is indicated above each image.

temperature, at least matching this fluence. We can zoom in on the smoother regions to more finely observe what the microstructure of the film is, as these regions are what we would prefer for the whole film to be like. In Fig. 7.12 the smooth regions at 680 °C and 700 °C are closer to what would be preferred for a smooth BFO film, with some rough terrace-like features. However, at 660 °C the film becomes exceptionally nanostructured. Within each of the smooth islands in the wider image there are even finer tendrill structures that have no particular preferred orientation and have widths on the order of tens of nanometers. Despite this, the film remains exceptionally smooth.

#### 7.4.2 Deposition Fluence

The deposition fluence was varied to see what effect this has on the surface quality. The growths from this point onwards were performed after a building move and with access to a higher laser fluence which was used for the growth of the SRO buffer layer. The new buffer layer is grown at a deposition fluence of  $f = 1.5 \text{ J/cm}^2$  to a thickness of approximately 40 nm, with all other parameters remaining the same. This surface should be comparable as we are able to observe similar changes in the RHEED intensity as was observed at the lower fluences, and so this is not significantly changing the SRO surface that we deposit upon. We show the result of growth at this higher fluence in Fig. 7.13 for samples grown at the previous best temperatures identified (660 °C, 680 °C and 700 °C) alongside the comparable samples grown at a low fluence.

From these new films, an increase in fluence alone is not sufficient to suppress the formation of tendrill features that dominate the surface and lead to a rough film. This

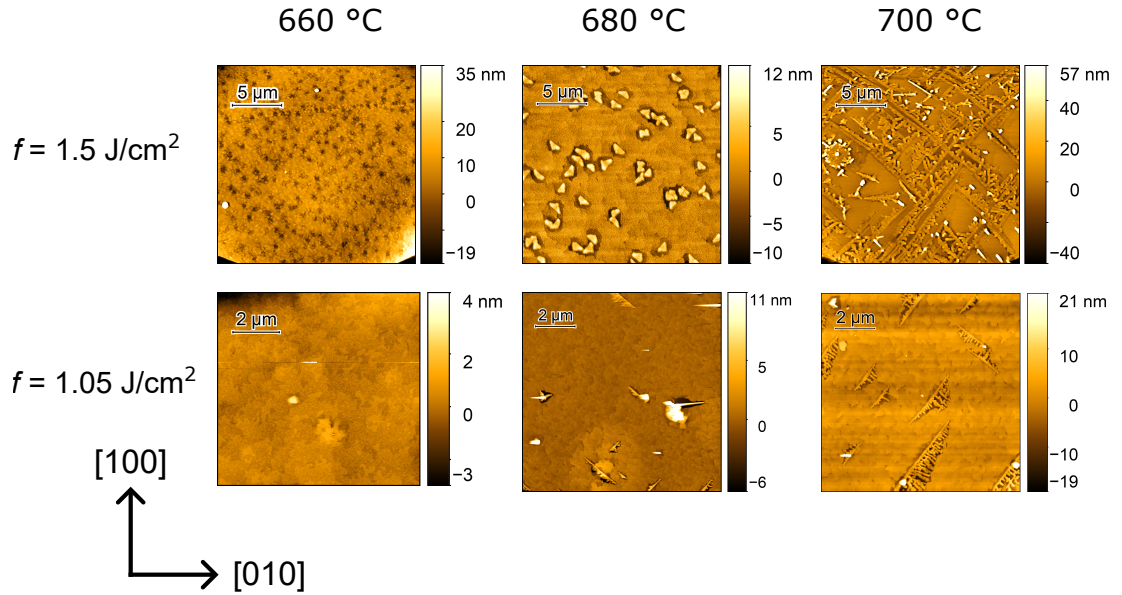


Figure 7.13: Temperature-fluence AFM phase diagram with fluence being the deposition fluence used for both the SRO and BFO layer, and temperature being the deposition temperature of the BFO only.

can however be used to understand these features in more detail. At an increased fluence of  $f = 1.35 \text{ J/cm}^2$ , the film grown is close to layer completion in which the film is mostly of the same height with the roughness resulting from pits and trenches in the film where the layer has not completed (although some islands are beginning to form above the film). The orientation of these pits are in the (110) direction of the surface and so we can understand that the origin of these features is the same as the tendrill features seen previously, and so we make the conclusion that these pits form where the tendrills have not fully coalesced into a complete layer.

It is not possible to remove the tendrill nanostructures with an increase of deposition fluence, given that the same structures appear in the film grown at  $T = 700 \text{ °C}$  with  $f = 1.5 \text{ J/cm}^2$ . However, it can also be inferred that the quality of the SRO layer is important for the BFO growth from the high-fluence film grown at  $T = 660 \text{ °C}$  where the film is much rougher than the same film grown at a lower fluence, but the island size remains small and the majority of the roughness comes from the circular dark regions of the scan.

### 7.4.3 PNR of BFO/CoFeB Heterostructure

From the previous results, the optimal BFO sample is identified with the BFO layer grown at a fluence of  $f = 1.05\text{J}/\text{cm}^2$  with a substrate temperature of 660 °C and deposit via DC sputtering a nominally 10 nm film of CoFeB with a 2 nm Pt cap to prevent oxidation. To characterise this heterostructure polarized neutron reflectivity (PNR) was used to probe the depth profile of the magnetic behaviour in both the BFO and the CoFeB layers. Hysteresis loops obtained from Kerr microscopy show that the CoFeB layer has a coercivity of 11.5 Oe and no measurable exchange bias, which is in line with reports in the literature [157] where the threshold thickness of the BFO layer to begin measuring an exchange bias is in the region of 18 nm.

PNR is performed using the PolRef instrument at the ISIS neutron and muon source and the data is fit using Refl1D [107]. The sample is measured under two biasing fields: a low field of 50 Oe and a saturating field of 7 kOe. Both are in excess of the 11.5 Oe coercivity of the sample measured from a hysteresis loop in a Kerr microscope. The obtained reflectivity data is co-fit to obtain the best fit to the behaviour of the sample.

Modelling the data obtained in this technique requires a lot of free variables associated with each layer, interface and form of scattering included and as such it is difficult to be sure that a model is truly correct [158]. The best practice, as explained well in the supplementary information of Ref. [158], is to use this technique to answer a question that can be clearly defined in contrasting models and compare the result of fitting to both models. In this case, the question to answer is: Is there magnetic ordering in the bismuth ferrite layer? By asking a simple question such as this I will compare two relatively simple models and draw a more definitive conclusion.

For the first model, the null case to consider is the scenario in which there is no detectable magnetic behaviour in the bismuth ferrite layer. Each layer in the material is modelled as a slab with Gaussian interfaces between each slab and the model fits the thickness, density, and interface roughness to determine the best structural properties of each layer. Magnetism in the CoFeB layer is modelled as a fixed value with dead layers of zero magnetism above and below the core of the layer thickness. These two quantities model regions in which the material may not be magnetic, such as at the bottom of the layer, and have their own interface that defines the transition between the region of dead magnetism and the core of the layer effectively allowing for a thinner magnetic SLD thickness that is offset from the structural interfaces. The bottom dead

Fitting Parameter	Fitted Value
STO Roughness	3.0 Å
SRO Roughness	5.4 Å
SRO Density	6.06 g/cm <sup>3</sup>
SRO Thickness	254 Å
BFO Roughness	2.4 Å
BFO Density	7.95 g/cm <sup>3</sup>
BFO Thickness	108 Å
CoFeB Roughness	14.9 Å
CoFeB Density	5.56 g/cm <sup>3</sup>
CoFeB Thickness	134 Å
Pt Roughness	11.2 Å
Pt Density	21.1 g/cm <sup>3</sup>
Pt Thickness	21 Å
CoFeB $\rho_M$	$3.51 \cdot 10^{-4} \text{ nm}^{-2}$
CoFeB lower magnetic dead layer	35 Å
CoFeB upper magnetic dead layer	0.2 Å
CoFeB lower magnetic interface	8.9 Å
CoFeB upper magnetic interface	0.1 Å

Table 7.2: Fitting parameters obtained for the model with no ferromagnetic moment fit to the BFO layer shown in Fig. 7.14.

layer allows for non-magnetic regions that may arise during the growth or through oxidation with the bismuth ferrite layer. The top dead layer allows for a reduced magnetic thickness if the capping Pt layer was insufficient to prevent oxidation of the CoFeB.

The results of this fitting are shown in Fig. 7.14. Shown in Fig. 7.14a) is the data obtained from the  $R^{++}$  and  $R^{--}$  polarized beam as well as the spin asymmetry,  $\frac{R^{++}-R^{--}}{R^{++}+R^{--}}$ , which is another way of plotting the same data. Fig. 7.14b) shows the nuclear and magnetic SLD profiles alongside the 68% and 95% Bayesian confidence intervals.

A bottom dead layer thickness for the CoFeB of 3.4 nm is obtained with an interface of 6 Å, significantly more than the approximately 0.5 nm dead layer that has been

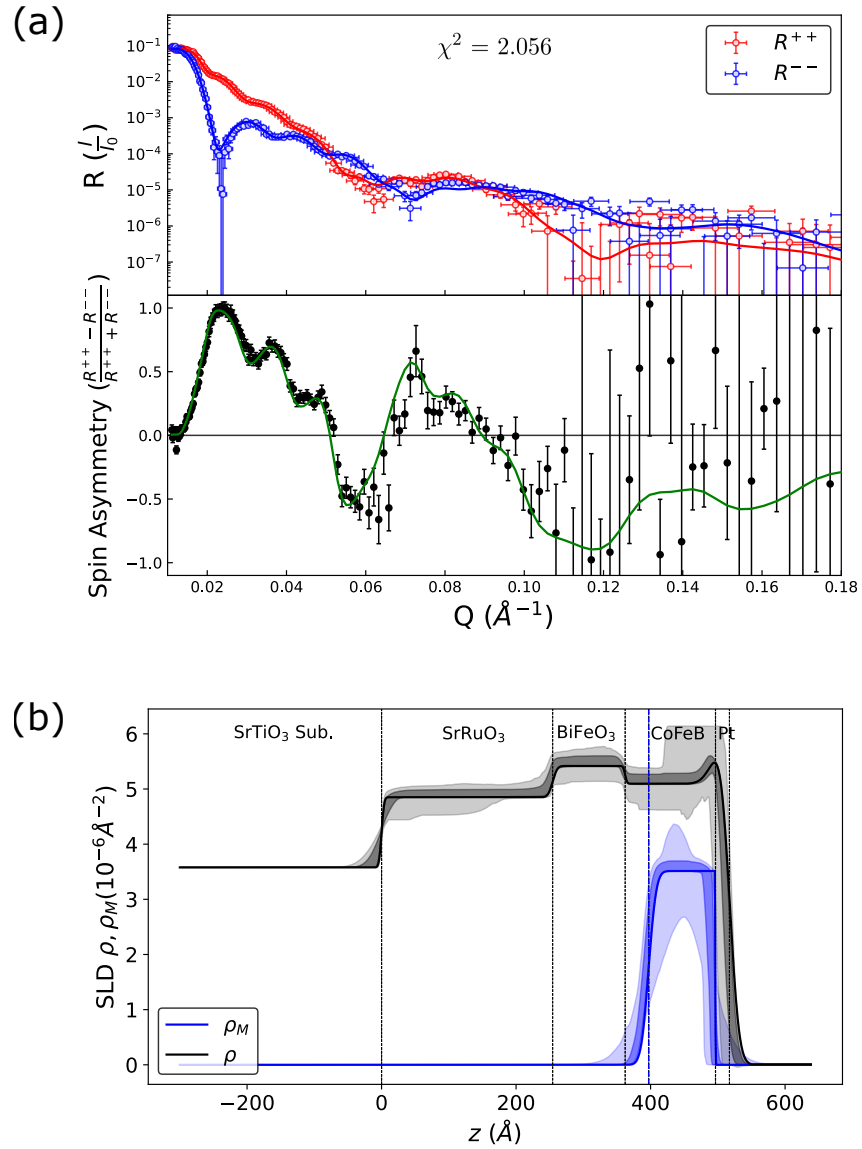


Figure 7.14: (a) PNR data obtained from the STO/SRO/BFO/CoFeB/Pt sample with raw data (points) and fits (lines) plotted above and the spin asymmetry plotted below. Fit corresponds to Model 1, where the magnetism is confined to the CoFeB layer only. (b) SLD profile corresponding to the best fit. Black dashed lines show nuclear SLD interface locations and blue dashed lines show magnetic SLD interfaces only. Data shown is for the dataset with a biasing field of 50 Oe.



reported for CoFeB grown on other materials [159] and substrates. This may be due to a difference in measurement techniques as in more rigorous studies of the magnetic dead layer the dead layer thickness is extracted by finding the thickness at which  $M_s$  extrapolates to zero in a thickness series, where here the magnetic dead layer represents the thickness at which the magnetic SLD begins to decrease with some interface smearing and so is likely a significant overestimate. If instead the dead layer is considered to be the point at which the magnitude of the magnetic SLD has dropped to 1% of the peak, then a dead layer of 1.4 nm can be obtained, which is still approximately 1 nm more than reported by Jang et al. in Ref. [159]. This larger dead layer thickness is attributed to a combination of roughness from the CoFeB growing on the BFO layer and the formation of an oxide layer at the BFO/CoFeB interface. The best fit for this data obtains a value of  $\chi^2 = 2.056$ .

To obtain a low  $\chi^2$ , there is a lack of distinction between the top CoFeB layer and the Pt cap resulting in a sharp rise in density at the CoFeB/Pt interface followed by a drop to 0 at the edge of the sample. Some level of intermixing could be expected, but it is difficult to be certain. This becomes the largest source of error in this model.

A second model is considered with a magnetic SLD added in the BFO layer. The inclusion of a small ferromagnetic moment is justified as the alignment of the uncompensated spins in the antiferromagnetic cycloid along the applied magnetic field direction. This will not completely accurately describe the magnetic texture of the cycloid - it is unlikely that at the fields used in this experiment will eliminate any antiferromagnetic domain structure in the sample and so the measurement will only be sensitive to some net moment alignment of the magnetism in the BFO layer with the field direction. This will be sufficient to answer the initial question. The model is the same as that of the CoFeB with two dead layers on either side of the core of the magnetic thickness. This is used as a simple model to consider if the inclusion of a magnetic moment in this layer generates a better fit to the data.

The fit obtained for this model is shown in Fig. 7.15. A lower value of  $\chi^2 = 1.979$  can be obtained, as well as better confidence intervals on the CoFeB and Pt layers in the SLD. The lower dead layer in the CoFeB remains consistent with the thickness that was obtained from the previous model. For the BFO dead layers, There is a smooth transition at the lower interface with the SRO layer but not at the surface with the CoFeB dead layer. The top interface with the CoFeB layer shows a dead layer in the

BFO of 15 Å.

The magnitude of the fitted magnetic SLD obtained is  $\rho_M = 0.1381 \times 10^{-6} \text{Å}^2$  which translates to a saturation magnetization of 48 emu/cc. This is of similar magnitude to previously reported magnetizations - Martin et al. [25] measure a range of 17 - 34 emu/cc by XMCD and Chen et al. [160] measure a range of 10 - 15 emu/cc also via XMCD. Some discrepancy is expected due to the difference in measurement techniques as both of these methods are indirect means of probing the magnetization, but in their paper, Martin et al. find good agreement with values obtained through SQUID magnetometry. This could be accounted for by the fact that our model includes a top dead layer in the BFO which would be difficult to measure by XMCD or SQUID. Equally, the Bayesian confidence intervals generated from the fit indicate that solutions could exist for reduced values of  $\rho_M$ , so it is difficult to say this is the true value of the magnetization.

Considering the top dead layer in more detail, this could be consistent with the interpretation that the dead layer in the CoFeB is increased by the proximity to the oxide interface as the all-oxide SRO-BFO interface shows no significant dead layer. If the oxide layer in the CoFeB is significant then the source of the oxygen at the interface will be the BFO layer, leading to an interface with a higher density of oxygen vacancies. As the magnetic behaviour is strongly tied to the oxygen octahedra in the unit cell, the accumulation of these vacancies could lead to a change in magnetic behaviour at the interface.

Previous PNR studies on BFO by Bea et al. [157] were only able to model magnetic behaviour at the BFO/CoFe interface at or above a thickness of 18 nm, the point at which they began to observe exchange bias in the films. The magnetism at this interface corresponds to the uncompensated spins in the BFO that contribute to the interfacial exchange bias. The model used here would allow for the effect of an interfacial moment if it was the preferred solution by adjustment of the dead layer thicknesses and as it does not we do not believe this model to be applicable. As our BFO film is thinner than this and we observed no exchange bias in our hysteresis loops, it is reasonable that we are not able to observe an interfacial moment as they reported.

In closing I return to the question that was initially posed: Is there magnetic ordering in the bismuth ferrite layer? By including a simple magnetic model for the bismuth ferrite layer which could model the uncompensated moment arising from canted

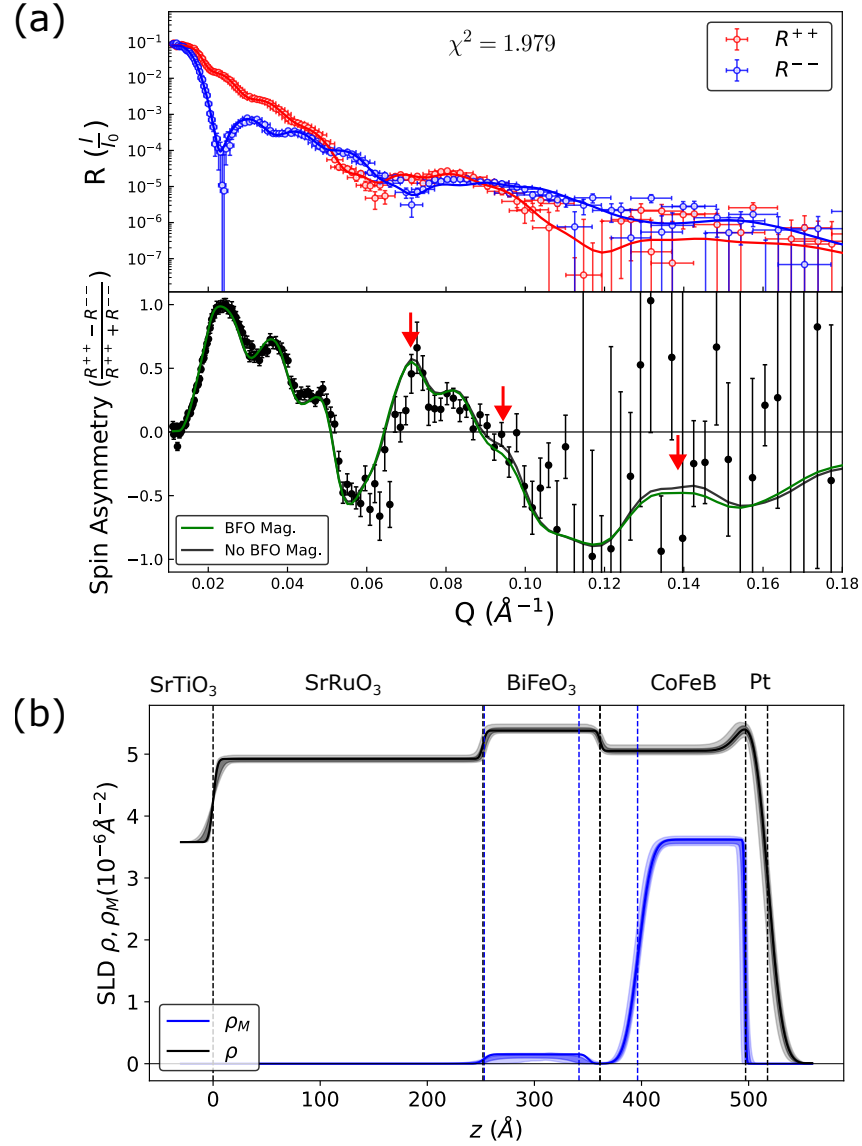


Figure 7.15: (a) PNR data obtained from the STO/SRO/BFO/CoFeB/Pt sample with raw data (points) and fits (lines) fitted to Model 2 where a magnetic moment is allowed in the BFO layer. The spin asymmetry for the previous model (No BFO Mag.) is included and red arrows highlight the key regions where the two fits differ. (b) SLD profile corresponding to the best fit. Black dashed lines show nuclear SLD interface locations and blue dashed lines show magnetic SLD interfaces only. Data shown is for the dataset with a biasing field of 50 Oe.

Fitting Parameter	Fitted Value
STO Roughness	3.2 Å
SRO Roughness	2.6 Å
SRO Density	6.15 g/cm <sup>3</sup>
SRO Thickness	252 Å
BFO Roughness	2.2 Å
BFO Density	7.90 g/cm <sup>3</sup>
BFO Thickness	109 Å
CoFeB Roughness	12.9 Å
CoFeB Density	5.51 g/cm <sup>3</sup>
CoFeB Thickness	136 Å
Pt Roughness	11.2 Å
Pt Density	20.73 g/cm <sup>3</sup>
Pt Thickness	21 Å
BFO $\rho_M$	0.15 10 <sup>-4</sup> nm <sup>-2</sup>
BFO lower magnetic dead layer	1 Å
BFO lower magnetic interface	4.7 Å
BFO upper magnetic dead layer	11 Å
BFO upper magnetic interface	3.5 Å
CoFeB $\rho_M$	3.62 10 <sup>-4</sup> nm <sup>-2</sup>
CoFeB lower magnetic dead layer	36 Å
CoFeB lower magnetic interface	10.1 Å
CoFeB upper magnetic dead layer	0.6 Å
CoFeB upper magnetic interface	1.0 Å

Table 7.3: Fitting parameters obtained for the weak ferromagnetic BiFeO<sub>3</sub> model shown in Fig. 7.15.

antiferromagnetic order, the  $\chi^2$  value improves. This would be consistent with some small ferromagnetic moment in the BFO resulting from an incomplete rotation of the spin cycloid. The magnitude of this moment is very small and the errors are quite significant, but there remains a non-zero moment even within the 95% error band. At this point it can be said that the inclusion of this moment improves the fit and it may be indicative of canted antiferromagnetic ordering in the bismuth ferrite. Given that this is a fitting technique with a large number of parameters we cannot be certain that this is the true solution.

## 7.5 Summary

In summary, I have obtained an optimal set of growth parameters for both SrRuO<sub>3</sub> and BiFeO<sub>3</sub> thin films grown by epitaxial pulsed laser deposition, with the ideal conditions for the SRO layer being a deposition temperature of 700 °C, and the temperature for the BFO layer being 660 °C and the fluence remaining the same for both. An AFM study of the surface explored the complex temperature-fluence relationship with film quality for both thin films, with significant deviations from these optimal temperatures leading to an extremely rough surface that would not be suitable for further growth.

PNR was performed on a BFO/CoFeB sample grown using this optimal recipe and, by comparison of the fitting models, it was determined that the BFO layer is likely to have a weak ferromagnetic moment as might be expected from good quality BFO. Further studies could confirm this with a thickness series which would then be likely to observe exchange bias.

This chapter has also demonstrated the cut-off ranges for two reported effects in the growth mode transitions of SrRuO<sub>3</sub> grown on STO: The transition from layer-by-layer to steady-step density, for which this chapter has shown some fluence dependence of, and the thickness at which it is no longer possible to recover strong layer-by-layer growth after an interruption to the SSD-type growth mode. This could be explored more in future with a more systematic study into the in-between values of fluence and thickness for both of these results to more accurately define the point at which the growth transitions occur.

In future, the quality of grown films could be improved through the use of the HF etch technique briefly mentioned earlier in this chapter or by the use of vicinal substrates, both of which have been shown to improve the growth of SRO on STO. A

better SRO layer may then improve the BFO layer.

---

# CHAPTER 8

---

Conclusions

## 8.1 Summary

The overlap of ferroelectric and ferromagnetic materials is a maturing field with increasing relevance. In this thesis, we built upon existing work by exploring the effects of ferroelectric pattern transfer on substrates based on (111)-oriented BTO surfaces which had previously not been combined with ferromagnetic thin films. We have also detailed the means by which we obtained a recipe for the growth of bismuth ferrite, a more complex ferroelectric material with antiferromagnetic ordering, the growth of which is a more mature field in the literature.

We have explored the strain-coupling between a (111)-cut barium titanite substrate with a sputtered 20 nm CoFeB thin film. On the (111) surface, the projection of the ferroelectric polarization vectors onto the (111) plane leads to two differing domain wall types in which the polarization rotates by either  $60^\circ$  or  $120^\circ$  through the domain wall and we have been able to observe that in the strain-coupled magnetic states this is efficiently transferred into the CoFeB. The change in anisotropy leads to an elastic coupling of ferromagnetic domain walls to ferroelectric domain walls, resulting in stripe domains that match the ferroelectric domain structure exactly. We have found that in the process of reversing the magnetization it is possible to nucleate within a stripe a  $180^\circ$  domain in which the edge follows the orientation of the magnetoelastic anisotropy axis within the stripe leading to either zig-zag domains in  $120^\circ$  magnetoelastic states or arrow-head domains in  $60^\circ$  domains, and that these reversal domains are field-orientation dependent with the process of domain nucleation and expansion changing as the field crosses the magnetoelastic anisotropy axes and the preferred domain wall formation changes from an uncharged domain wall to charged domain wall.

The temperature dependence of the BTO(111)/CoFeB heterostructures has been explored using an optical cryostat attachment to the Kerr microscope. The dependence is dominated strongly by the substrate and the strain it imparts more than any other component of the artificial multiferroic, and we find that it does not have a significant impact on the saturation magnetization of the magnetic thin film. The anisotropy has been observed to change significantly with the crystal phase and polar order of the barium titanite substrate and we have extended our interpretation of the impact by means of micromagnetic simulation of the domain wall widths. At the extremes of the temperature range, where the anisotropy strength is significantly reduced from the tetragonal phase, we expect a large difference between the  $60^\circ$  and  $120^\circ$  domain wall



states which must result only from the difference in the angle at which the magnetization is pinned to either side of the domain wall, the magnetoelastic anisotropy angle as we have called it.

The impact of this magnetoelastic anisotropy angle has been explored in more detail by examining the change of domain wall properties with varied magnetoelastic angle alongside other micromagnetic parameters. We explain the change in properties as dependent upon the spin rotation across the domain wall which for the uncharged domain walls always remains close to the expected value of  $2\theta_A$ , but for the charged domain walls the accumulation of magnetic charge at the domain wall leads to a reduction in the total spin rotation. This leads to differing behaviour with increasing saturation magnetization and some bending of the contours as compared with the uncharged case, but the behaviour remains consistent under an applied magnetic field even with a small reduction in the spin rotation. Importantly, we find that there are inflection points in the angle-dependent behaviour of all domain wall properties investigated which vary with the balance of micromagnetic values relative to each other.

Finally we have begun the work towards the development of all-thin-film ferroelectric-ferromagnet heterostructures in the condensed matter group at Leeds, optimizing the growth of a bismuth ferrite heterostructure grown on STO/SRO. We have developed a recipe that can serve as the foundation for future work growing this thin film ferroelectric material, alongside a recipe for the conducting strontium ruthenate layer which will be useful for the growth of other oxide materials by pulsed laser deposition.

In conclusion the properties of interfacially coupled ferroelectric-ferromagnet heterostructures has been explored in this thesis. The field remains an interesting and promising means of achieving voltage control of magnetism, with a great deal of fundamental physics to explore alongside the development of functional devices.

## 8.2 Future Work

Regarding the work performed on BTO(111)-based heterostructures, an obvious route remains unexplored: The application of an electric field. As compared with the (100) cut of the BTO, the application of an electric field out-of-plane would not be along any crystal axis and so we cannot expect smooth domain wall motion by the formation and expansion/contraction of  $c$ -domains that leads to a smooth control over the position of a magnetic domain wall. However, there are other opportunities. Firstly, there

is the possibility to explore using an electric field to toggle between a  $60^\circ$  or  $120^\circ$  magnetoelastic structure, although we might not expect this to be a ‘clean’ transition in which the domain wall remains in the same orientation before and after the application of an electric field. Secondly, close to the crystal transition temperatures, there is the possibility for an electric field-induced transition which would provide a more broad opportunity for a temperature-electric field control over a magnetic layer [161]. This brings with it some challenges; the electric fields required for this are in the region of 40 kV/cm, which for a 500  $\mu\text{m}$  substrate is an applied voltage of 2 kV/cm. This presents two forms of experimental challenges: one in the experimental design surrounding the experiment and coping with high voltages in existing experimental configurations, and a sample design challenge in that at these high voltages there is a significant chance of dielectric breakdown or film damage that would destroy the sample.

We could also consider the investigation of devices based on these strain-coupled domains in more detail. As we showed at the end of Chapter 6, we would expect particularly significant changes in the dispersion relations and so we could make devices to excite this domain wall of which there are already templates in the literature [146, 147, 162] with a focus on trying to switch between the two strain-states to change the dynamics of the device. It would also be interesting to observe the difference in magnetoresistance of the various charged and uncharged domain textures as measured in a hall bar configuration.

For the work on bismuth ferrite, the optimized recipe obtained presents a good platform for which to conduct future work. Certainly, more material development is preferable to obtain samples more in line with the literature, but an immediate first step would be to grow thicker (60 nm) samples and perform piezoresponse force microscopy to verify the ferroelectric domain structure, or to grow a thin ferromagnetic layer to observe stronger interfacial coupling which we did not see as our optimal samples were below a critical thickness at which these effects start to emerge. From this, it would be interesting to combine this with existing spintronic-relevant heterostructures: Pt/Co/Pt is a prominent PMA trilayer that has already been combined with BFO in some capacity already [163] while keeping an active interest for the electric field control of PMA devices, but we could also explore ferroelectric and magnetoelectric tunnel junction devices.

## REFERENCES

- [1] The Semiconductor Industry Association, 2022 State of the U.S. Semiconductor Industry, 2022. Accessed: Jun. 29th 2023. [Online]. Available: [semiconductors.org](https://www.semiconductors.org)
- [2] I. A. T. Hashem, I. Yaqoob, N. B. Anuar, S. Mokhtar, A. Gani et al., The rise of “big data” on cloud computing: Review and open research issues, *Information Systems* **47**, 98 (2015)
- [3] J. Hoffmann, S. Borgeaud, A. Mensch, E. Buchatskaya, T. Cai et al., Training compute-optimal large language models (2022)
- [4] J.-M. Hu and C.-W. Nan, Opportunities and challenges for magnetoelectric devices, *APL Materials* **7**, 080905 (2019)
- [5] N. A. Spaldin and R. Ramesh, Advances in magnetoelectric multiferroics, *Nature Materials* **18**, 203 (2019)
- [6] G. Burns and F. Dacol, Polarization in the cubic phase of BaTiO<sub>3</sub>, *Solid State Communications* **42**, 9 (1982)
- [7] L. E. Cross, Relaxor ferroelectrics, *Ferroelectrics* **76**, 241 (1987)
- [8] A. Bortis, M. Trassin, M. Fiebig and T. Lottermoser, Manipulation of charged domain walls in geometric improper ferroelectric thin films: A phase-field study, *Physical Review Materials* **6**, 064403 (2022)
- [9] T. Jungk, Á. Hoffmann, M. Fiebig and E. Soergel, Electrostatic topology of ferroelectric domains in YMnO<sub>3</sub>, *Applied Physics Letters* **97**, 012904 (2010)

- 
- [10] Y. Aikawa, T. Katsufuji, T. Arima and K. Kato, Effect of Mn trimerization on the magnetic and dielectric properties of  $\text{YMnO}_3$ , *Physical Review B* **71**, 184418 (2005)
- [11] G. A. Smolenskiĭ and I. E. Chupis, Ferroelectromagnets, *Soviet Physics Uspekhi* **25**, 475 (1982)
- [12] J. Wang, J. B. Neaton, H. Zheng, V. Nagarajan, S. B. Ogale et al., Epitaxial  $\text{BiFeO}_3$  multiferroic thin film heterostructures, *Science* **299**, 1719 (2003)
- [13] S. N. V., K. B. Vinayakumar and K. K. Nagaraja, Magnetoelectric coupling in bismuth ferrite—challenges and perspectives, *Coatings* **10**, 1221 (2020)
- [14] A. F. Popkov, M. D. Davydova, K. A. Zvezdin, S. V. Solov'yov and A. K. Zvezdin, Origin of the giant linear magnetoelectric effect in perovskitelike multiferroic  $\text{BiFeO}_3$ , *Physical Review B* **93**, 094435 (2016)
- [15] R. T. Smith, G. D. Achenbach, R. Gerson and W. J. James, Dielectric properties of solid solutions of  $\text{BiFeO}_3$  at high temperature and high frequency, *Journal of Applied Physics* **39**, 70 (1968)
- [16] J. Silva, A. Reyes, H. Esparza, H. Camacho and L. Fuentes,  $\text{BiFeO}_3$ : A review on synthesis, doping and crystal structure, *Integrated Ferroelectrics* **126**, 47 (2011)
- [17] J. T. Zhang, X. M. Lu, J. Zhou, H. Sun, J. Su et al., Origin of magnetic anisotropy and spiral spin order in multiferroic  $\text{BiFeO}_3$ , *Applied Physics Letters* **100**, 242413 (2012)
- [18] I. Sosnowska, T. P. Neumaier and E. Steichele, Spiral magnetic ordering in bismuth ferrite, *Journal of Physics C: Solid State Physics* **15**, 4835 (1982)
- [19] I. Sosnowska, M. Loewenhaupt, W. David and R. Ibberson, Investigation of the unusual magnetic spiral arrangement in  $\text{BiFeO}_3$ , *Physica B: Condensed Matter* **180-181**, 117 (1992)
- [20] I. Sosnowska and A. Zvezdin, Origin of the long period magnetic ordering in  $\text{BiFeO}_3$ , *Journal of Magnetism and Magnetic Materials* **140-144**, 167 (1995)

- 
- [21] F. Kubel and H. Schmid, Structure of a ferroelectric and ferroelastic monodomain crystal of the perovskite  $\text{BiFeO}_3$ , *Acta Crystallographica Section B Structural Science* **46**, 698 (1990)
- [22] H. Feng, The role of Coulomb and exchange interaction on the Dzyaloshinskii–Moriya interaction (DMI) in  $\text{BiFeO}_3$ , *Journal of Magnetism and Magnetic Materials* **322**, 1765 (2010)
- [23] I. Gross, W. Akhtar, V. Garcia, L. J. Martínez, S. Chouaieb et al., Real-space imaging of non-collinear antiferromagnetic order with a single-spin magnetometer, *Nature* **549**, 252 (2017)
- [24] H. Zhong, A. Finco, J. Fischer, A. Haykal, K. Bouzehouane et al., Quantitative Imaging of Exotic Antiferromagnetic Spin Cycloids in  $\text{BiFeO}_3$  Thin Films, *Physical Review Applied* **17**, 044051 (2022)
- [25] L. W. Martin, Y.-H. Chu, M. B. Holcomb, M. Huijben, P. Yu et al., Nanoscale control of exchange bias with  $\text{BiFeO}_3$  Thin Films, *Nano Letters* **8**, 2050 (2008)
- [26] J. T. Heron, M. Trassin, K. Ashraf, M. Gajek, Q. He et al., Electric-field-induced magnetization reversal in a ferromagnet-multiferroic heterostructure, *Phys. Rev. Lett.* **107**, 217202 (2011)
- [27] J. T. Heron, J. L. Bosse, Q. He, Y. Gao, M. Trassin et al., Deterministic switching of ferromagnetism at room temperature using an electric field, *Nature* **516**, 370 (2014)
- [28] A. Chen, R.-C. Peng, B. Fang, T. Yang, Y. Wen et al., Nonvolatile magnetoelectric switching of magnetic tunnel junctions with dipole interaction, *Advanced Functional Materials* **33**, 2213402 (2023)
- [29] Z. Zhou, M. Trassin, Y. Gao, Y. Gao, D. Qiu et al., Probing electric field control of magnetism using ferromagnetic resonance, *Nature Communications* **6**, 6082 (2015)
- [30] A. Bencan, G. Drazic, H. Ursic, M. Makarovic, M. Komelj et al., Domain-wall pinning and defect ordering in  $\text{BiFeO}_3$  probed on the atomic and nanoscale, *Nature Communications* **11**, 1762 (2020)

- 
- [31] H.-B. Zhang, M.-M. Yang and M. Alexe, Boosting the photocurrent in BiFeO<sub>3</sub> thin films via a domain-wall-defect interaction, *Advanced Photonics Research* **4**, 2200189 (2022)
- [32] G. Catalan, J. Seidel, R. Ramesh and J. F. Scott, Domain wall nanoelectronics, *Reviews of Modern Physics* **84**, 119 (2012)
- [33] M. Acharya, C. R. Joshi and A. Gupta, Growth of samarium-substituted epitaxial bismuth ferrite films by chemical vapor deposition, *Crystal Growth & Design* **23**, 2065 (2023)
- [34] S. M. Yakout, Spintronics and innovative memory devices: a review on advances in magnetoelectric BiFeO<sub>3</sub>, *Journal of Superconductivity and Novel Magnetism* **34**, 317 (2021)
- [35] M. M. S. Mohan, S. Bandyopadhyay, T. Jogi, S. Bhattacharya and R. Ramadurai, Realization of rhombohedral, mixed, and tetragonal like phases of BiFeO<sub>3</sub> and ferroelectric domain engineering using a strain tuning layer on LaAlO<sub>3</sub>(001) substrate, *Journal of Applied Physics* **125**, 012501 (2019)
- [36] Y. Heo, J. H. Lee, L. Xie, X. Pan, C.-H. Yang et al., Enhanced conductivity at orthorhombic–rhombohedral phase boundaries in BiFeO<sub>3</sub> thin films, *NPG Asia Materials* **8**, e297 (2016)
- [37] S. M. Griffin, M. Lilienblum, K. T. Delaney, Y. Kumagai, M. Fiebig et al., Scaling behavior and beyond equilibrium in the hexagonal manganites, *Physical Review X* **2**, 041022 (2012)
- [38] M. Li, H. Tan and W. Duan, Hexagonal rare-earth manganites and ferrites: a review of improper ferroelectricity, magnetoelectric coupling, and unusual domain walls, *Physical Chemistry Chemical Physics* **22**, 14415 (2020)
- [39] W. Wang, J. Zhao, W. Wang, Z. Gai, N. Balke et al., Room-temperature multiferroic hexagonal LuFeO<sub>3</sub> films, *Physical Review Letters* **110**, 237601 (2013)
- [40] S. Goswami, S. Mishra, K. Dana, A. K. Mandal, N. Dey et al., Room-temperature multiferroicity in GaFeO<sub>3</sub> thin film grown on (100) Si substrate, *Journal of Applied Physics* **132**, 214101 (2022)

- 
- [41] C.-W. Nan, M. I. Bichurin, S. Dong, D. Viehland and G. Srinivasan, Multiferroic magnetoelectric composites: Historical perspective, status, and future directions, *Journal of Applied Physics* **103**, 031101 (2008)
- [42] B. B. V. Aken, T. T. Palstra, A. Filippetti and N. A. Spaldin, The origin of ferroelectricity in magnetoelectric YMnO<sub>3</sub>, *Nature Materials* **3**, 164 (2004)
- [43] G. H. Haertling, Ferroelectric ceramics: History and technology, *Journal of the American Ceramic Society* **82**, 797 (1999)
- [44] N. D'Souza, A. Biswas, H. Ahmad, M. S. Fashami, M. M. Al-Rashid et al., Energy-efficient switching of nanomagnets for computing: straintronics and other methodologies, *Nanotechnology* **29**, 442001 (2018)
- [45] Y. Wang, J. Hu, Y. Lin and C.-W. Nan, Multiferroic magnetoelectric composite nanostructures, *NPG Asia Materials* **2**, 61 (2010)
- [46] T. H. E. Lahtinen, J. O. Tuomi and S. van Dijken, Pattern transfer and electric-field-induced magnetic domain formation in multiferroic heterostructures, *Advanced Materials* **23**, 3187 (2011)
- [47] A. Casiraghi, T. Rincón Domínguez, S. Rößler, K. J. A. Franke, D. López González et al., Influence of elastically pinned magnetic domain walls on magnetization reversal in multiferroic heterostructures, *Phys. Rev. B* **92**, 054406 (2015)
- [48] T. H. E. Lahtinen, J. O. Tuomi and S. van Dijken, Electrical writing of magnetic domain patterns in ferromagnetic/ferroelectric heterostructures, *IEEE Transactions on Magnetics* **47**, 3768 (2011)
- [49] T. H. E. Lahtinen, K. J. A. Franke and S. van Dijken, Electric-field control of magnetic domain wall motion and local magnetization reversal, *Scientific Reports* **2**, 258 (2012)
- [50] K. J. A. Franke, B. Van de Wiele, Y. Shirahata, S. J. Hämäläinen, T. Taniyama et al., Reversible electric-field-driven magnetic domain-wall motion, *Phys. Rev. X* **5**, 011010 (2015)

- 
- [51] Y. Shirahata, R. Shiina, D. L. González, K. J. A. Franke, E. Wada et al., Electric-field switching of perpendicularly magnetized multilayers, *NPG Asia Materials* **7**, e198 (2015)
- [52] D. L. González, Y. Shirahata, B. V. de Wiele, K. J. A. Franke, A. Casiraghi et al., Electric-field-driven domain wall dynamics in perpendicularly magnetized multilayers, *AIP Advances* **7**, 035119 (2017)
- [53] M. Goiriena-Goikoetxea, Z. Xiao, A. El-Ghazaly, C. V. Stan, J. Chatterjee et al., Influence of dislocations and twin walls in BaTiO<sub>3</sub> on the voltage-controlled switching of perpendicular magnetization, *Physical Review Materials* **5**, 024401 (2021)
- [54] Y. Cheng, G. Dong, Y. Li, G. Yang, B. Zhang et al., Strain modulation of perpendicular magnetic anisotropy in wrinkle-patterned (Co/Pt)/BaTiO<sub>3</sub> magneto-electric heterostructures, *ACS Nano* **16**, 11291 (2022)
- [55] Z.-W. Yin, H.-S. Luo, P.-C. Wang and G.-S. Xu, Growth, characterization and properties of relaxor ferroelectric PMN-PT single crystals, *Ferroelectrics* **229**, 207 (1999)
- [56] D. B. Gopman, C. L. Dennis, P. J. Chen, Y. L. Iudin, P. Finkel et al., Strain-assisted magnetization reversal in Co/Ni multilayers with perpendicular magnetic anisotropy, *Scientific Reports* **6**, 27774 (2016)
- [57] X. Xiao, L. Sun, Y. M. Luo, D. Zhang, J. H. Liang et al., Electrical manipulation of perpendicular magnetic anisotropy in a Pt/Co/Pt trilayer grown on PMN-PT(011) substrate, *Journal of Physics D: Applied Physics* **51**, 115001 (2018)
- [58] C. Song, B. Cui, F. Li, X. Zhou and F. Pan, Recent progress in voltage control of magnetism: Materials, mechanisms, and performance, *Progress in Materials Science* **87**, 33 (2017)
- [59] Q. Guo and Z. Wang, Temperature assistance of electric field-controlled spin-orbit torque-based magnetization switching in PMN-PT/FePt heterostructures, *RSC Advances* **11**, 12043 (2021)



- 
- [60] M. Filianina, J.-P. Hanke, K. Lee, D.-S. Han, S. Jaiswal et al., Electric-field control of spin-orbit torques in perpendicularly magnetized W/CoFeB/MgO films, *Physical Review Letters* **124**, 217701 (2020)
- [61] X. Wang, Q. Yang, L. Wang, Z. Zhou, T. Min et al., E-field control of the RKKY interaction in FeCoB/Ru/FeCoB/PMN-PT (011) multiferroic heterostructures, *Advanced Materials* **30**, 1803612 (2018)
- [62] N. Gusev, A. Sadovnikov, S. Nikitov, M. Sapozhnikov and O. Udalov, Manipulation of the Dzyaloshinskii–Moriya interaction in Co/Pt multilayers with strain, *Physical Review Letters* **124**, 157202 (2020)
- [63] V. Wadhawan, *Introduction to Ferroic Materials*, CRC Press (2000)
- [64] C. Kittel, *Introduction to solid state physics*, John Wiley & Sons, Nashville, TN, 8 edition (2004)
- [65] A. Aharoni, *Introduction to the theory of ferromagnetism*, International Series of Monographs on Physics, Clarendon Press, Oxford, England, 2 edition (2002)
- [66] W. Pauli, Über den zusammenhang des abschlusses der elektronengruppen im atom mit der komplexstruktur der spektren, *Zeitschrift für Physik* **31**, 765 (1925)
- [67] S. Blundell, *Magnetism in Condensed Matter*, Oxford Master Series in Condensed Matter Physics, Oxford University Press, London, England (2001)
- [68] W. J. Antel, M. M. Schwickert, T. Lin, W. L. O’Brien and G. R. Harp, Induced ferromagnetism and anisotropy of Pt layers in Fe/Pt(001) multilayers, *Physical Review B* **60**, 12933 (1999)
- [69] F. Li, L. Wang, L. Jin, D. Lin, J. Li et al., Piezoelectric activity in perovskite ferroelectric crystals, *IEEE Transactions on Ultrasonics, Ferroelectrics, and Frequency Control* **62**, 18 (2015)
- [70] R. B. Meyer, Ferroelectric liquid crystals; a review, *Molecular Crystals and Liquid Crystals* **40**, 33 (1977)
- [71] R. Kepler and R. Anderson, Ferroelectric polymers, *Advances in Physics* **41**, 1 (1992)

- 
- [72] F. Jona and G. Shirane, *Ferroelectric Crystals*, Dover Publications (1993)
- [73] D. S. Campbell, Soft modes in ferroelectrics and antiferroelectrics, *Physics Bulletin* **27**, 124 (1976)
- [74] A. Devonshire, XCVI. theory of barium titanate, *The London, Edinburgh, and Dublin Philosophical Magazine and Journal of Science* **40**, 1040 (1949)
- [75] P. Chandra and P. B. Littlewood, A Landau primer for ferroelectrics, in *Topics in Applied Physics*, Springer Berlin Heidelberg, pp. 69–116 (2007)
- [76] E. K. Salje, *Phase Transitions in Ferroelastic and Co-elastic Crystals*, Cambridge University Press (1991)
- [77] E. K. H. Salje, Ferroelastic twinning in minerals: A source of trace elements, conductivity, and unexpected piezoelectricity, *Minerals* **11**, 478 (2021)
- [78] Y. Xu, G. Shao, J. Pang, Y. Zhou, X. Ding et al., Avalanches during ferroelectric and ferroelastic switching in barium titanate ceramics, *Physical Review Materials* **6**, 124413 (2022)
- [79] A. T. Hindmarch, A. W. Rushforth, R. P. Champion, C. H. Marrows and B. L. Gallagher, Origin of in-plane uniaxial magnetic anisotropy in CoFeB amorphous ferromagnetic thin films, *Physical Review B* **83**, 212404 (2011)
- [80] M. Getzlaff, *Fundamentals of Magnetism*, Springer (2010)
- [81] E. C. Stoner, XCVII. the demagnetizing factors for ellipsoids, *The London, Edinburgh, and Dublin Philosophical Magazine and Journal of Science* **36**, 803 (1945)
- [82] M. B. Moffett, A. E. Clark, M. Wun-Fogle, J. Linberg, J. P. Teter et al., Characterization of Terfenol-D for magnetostrictive transducers, *The Journal of the Acoustical Society of America* **89**, 1448 (1991)
- [83] M. J. Dapino, *Magnetostrictive Materials*, John Wiley & Sons, Ltd (2002)
- [84] E. Villari, Ueber die Aenderungen des magnetischen Moments, welche der Zug und das Hindurchleiten eines galvanischen Stroms in einem Stabe von Stahl oder Eisen hervorbringen, *Annalen der Physik und Chemie* **202**, 87 (1865)

- 
- [85] E. C. Stoner and E. P. Wohlfarth, A mechanism of magnetic hysteresis in heterogeneous alloys, *Philosophical Transactions of the Royal Society of London. Series A, Mathematical and Physical Sciences* **240**, 599 (1948)
- [86] F. Bloch, Zur theorie des austauschproblems und der remanenzerscheinung der ferromagnetika, in *Zur Theorie des Austauschproblems und der Remanenzerscheinung der Ferromagnetika*, Springer Berlin Heidelberg, pp. 295–335 (1932)
- [87] B. Lilley, LXXI. energies and widths of domain boundaries in ferromagnetics, *The London, Edinburgh, and Dublin Philosophical Magazine and Journal of Science* **41**, 792 (1950)
- [88] M. H. Kryder, T. J. Gallagher and R. A. Scranton, Néel walls and line transitions in a (100) garnet film, *Journal of Applied Physics* **53**, 5810 (1982)
- [89] M. Heide, G. Bihlmayer and S. Blügel, Dzyaloshinskii-moriya interaction accounting for the orientation of magnetic domains in ultrathin films: Fe/W(110), *Physical Review B* **78**, 140403(R) (2008)
- [90] A. Hubert and R. Schäfer, *Magnetic Domains*, Springer Berlin, Heidelberg, 1 edition (1998)
- [91] J. P. Jakubovics, Comments on the definition of ferromagnetic domain wall width, *Philosophical Magazine B* **38**, 401 (1978)
- [92] L. Landau and E. Lifshitz, On the theory of the dispersion of magnetic permeability in ferromagnetic bodies, in *Perspectives in Theoretical Physics*, Elsevier, pp. 51–65 (1992)
- [93] T. Gilbert, Classics in magnetics a phenomenological theory of damping in ferromagnetic materials, *IEEE Transactions on Magnetics* **40**, 3443 (2004)
- [94] J. Slonczewski, Current-driven excitation of magnetic multilayers, *Journal of Magnetism and Magnetic Materials* **159**, L1 (1996)
- [95] M. Stafe, A. Marcu and N. N. Puscas, *Pulsed Laser Ablation of Solids*, Springer Berlin Heidelberg (2014)
- [96] I. N. Mihailescu and A. P. Caricato, eds., *Pulsed Laser Ablation*, Jenny Stanford Publishing (2018)

- 
- [97] N. F. Farrashbandi and M. Eslami-Kalantari, Inverse bremsstrahlung absorption in laser-fusion plasma, *Journal of Theoretical and Applied Physics* **14**, 261 (2020)
- [98] J. Schou, Physical aspects of the pulsed laser deposition technique: The stoichiometric transfer of material from target to film, *Applied Surface Science* **255**, 5191 (2009)
- [99] J. Chen, M. Döbeli, D. Stender, M. M. Lee, K. Conder et al., Tracing the origin of oxygen for  $\text{La}_{0.6}\text{Sr}_{0.4}\text{MnO}_3$  thin film growth by pulsed laser deposition, *Journal of Physics D: Applied Physics* **49**, 045201 (2015)
- [100] L. V. Azaroff, *X-ray Diffraction*, Pure & Applied Physics S., McGraw-Hill, New York, NY (1974)
- [101] J. Als-Nielsen and D. McMorrow, *Elements of Modern X-ray Physics*, John Wiley & Sons, Ltd (2011)
- [102] H. Kiessig, Interferenz von röntgenstrahlen an dünnen schichten, *Annalen der Physik* **402**, 769 (1931)
- [103] M. Björck and G. Andersson, GenX: an extensible X-ray reflectivity refinement program utilizing differential evolution, *Journal of Applied Crystallography* **40**, 1174 (2007)
- [104] L. G. Parratt, Surface studies of solids by total reflection of x-rays, *Physical Review* **95**, 359 (1954)
- [105] R. Cubitt and G. Fragneto, Neutron reflection:, in *Scattering*, Elsevier, pp. 1198–1208 (2002)
- [106] R. M. Moon, T. Riste and W. C. Koehler, Polarization analysis of thermal-neutron scattering, *Physical Review* **181**, 920 (1969)
- [107] P. A. Kienzle, B. B. Maranville, K. V. O'Donovan, J. F. Ankner, N. F. Berk et al., Reflectometry software (2017)
- [108] A. Ichimiya and P. I. Cohen, *Reflection High-Energy Electron Diffraction*, Cambridge University Press (2004)

- 
- [109] F. Niu and B. W. Wessels, Epitaxial growth and strain relaxation of BaTiO<sub>3</sub> thin films on SrTiO<sub>3</sub> buffered (001) si by molecular beam epitaxy, *Journal of Vacuum Science and Technology B: Microelectronics and Nanometer Structures Processing, Measurement, and Phenomena* **25**, 1053 (2007)
- [110] S. Hasegawa, Reflection high-energy electron diffraction, in E. N. Kaufmann, ed., *Characterization of materials*, John Wiley & Sons, Inc. (2012)
- [111] H. Ebert, Magneto-optical effects in transition metal systems, *Reports on Progress in Physics* **59**, 1665 (1996)
- [112] K. Helmut, S. Parkin and R. Schäfer, *Investigation of Domains and Dynamics of domain walls by the magneto-optical Kerr effect*, John Wiley & Sons, chapter Investigation of Domains and Dynamics of domain walls by the magneto-optical Kerr effect (2007)
- [113] I. V. Soldatov and R. Schäfer, Selective sensitivity in kerr microscopy, *Review of Scientific Instruments* **88**, 073701 (2017)
- [114] I. V. Soldatov and R. Schäfer, Advances in quantitative kerr microscopy, *Physical Review B* **95**, 014426 (2017)
- [115] S. Imada, S. Suga, W. Kuch and J. Kirschner, Magnetic microspectroscopy by a combination of XMCD and PEEM, *Surface Review and Letters* **9**, 877 (2002)
- [116] J. Feng, E. Forest, A. A. MacDowell, M. Marcus, H. Padmore et al., An x-ray photoemission electron microscope using an electron mirror aberration corrector for the study of complex materials, *Journal of Physics: Condensed Matter* **17**, S1339 (2005)
- [117] R. L. Fagaly, Superconducting quantum interference device instruments and applications, *Review of Scientific Instruments* **77**, 101101 (2006)
- [118] E. Meyer, H. J. Hug and R. Bennewitz, *Scanning Probe Microscopy*, Springer Berlin Heidelberg (2004)
- [119] Bruker, SPM Training Guide [Online], Available: <https://archive.is/vOmpM>. [Accessed: Jun. 29th 2023] (2010)

- 
- [120] A. Vansteenkiste, J. Leliaert, M. Dvornik, M. Helsen, F. Garcia-Sanchez et al., The design and verification of MuMax3, *AIP Advances* **4**, 107133 (2014)
- [121] S. Zhang and Z. Li, Roles of nonequilibrium conduction electrons on the magnetization dynamics of ferromagnets, *Physical Review Letters* **93**, 127204 (2004)
- [122] K. J. A. Franke, T. H. E. Lahtinen and S. van Dijken, Field tuning of ferromagnetic domain walls on elastically coupled ferroelectric domain boundaries, *Phys. Rev. B* **85**, 094423 (2012)
- [123] R. G. Hunt, K. J. A. Franke, P. M. Shepley and T. A. Moore, Strain-coupled domains in BaTiO<sub>3</sub>(111)-CoFeB heterostructures, *Physical Review B* **107**, 014409 (2023)
- [124] M. Trassin, G. D. Luca, S. Manz and M. Fiebig, Probing ferroelectric domain engineering in BiFeO<sub>3</sub> thin films by second harmonic generation, *Advanced Materials* **27**, 4871 (2015)
- [125] S. Wada, S. Suzuki, T. Noma, T. Suzuki, M. Osada et al., Enhanced piezoelectric property of barium titanate single crystals with engineered domain configurations, *Japanese Journal of Applied Physics* **38**, 5505 (1999)
- [126] P. W. Forsbergh, Domain structures and phase transitions in barium titanate, *Phys. Rev.* **76**, 1187 (1949)
- [127] K. J. A. Franke, D. López González, S. J. Hämäläinen and S. van Dijken, Size dependence of domain pattern transfer in multiferroic heterostructures, *Phys. Rev. Lett.* **112**, 017201 (2014)
- [128] K. J. A. Franke, C. Ophus, A. K. Schmid and C. H. Marrows, Competition between exchange and magnetostatic energies in domain pattern transfer from BaTiO<sub>3</sub>(111) to a Ni thin film, *Phys. Rev. Mater.* **7**, 034403 (2023)
- [129] X. Zhang, T. Hashimoto and D. C. Joy, Electron holographic study of ferroelectric domain walls, *Applied Physics Letters* **60**, 784 (1992)
- [130] B. Jiang, J. L. Peng, L. A. Bursill and W. L. Zhong, Size effects on ferroelectricity of ultrafine particles of PbTiO<sub>3</sub>, *Journal of Applied Physics* **87**, 3462 (2000)

- 
- [131] K. J. A. Franke, C. Ophus, A. K. Schmid and C. H. Marrows, 60° and 120° Domain Walls in Epitaxial BaTiO<sub>3</sub>(111)/Co Multiferroic Heterostructures, *Physical Review B* **107**, L140407 (2023)
- [132] R. G. Hunt, K. J. A. Franke, P. S. Keatley, P. M. Shepley, M. Rogers et al., Temperature dependence of magnetic anisotropy and domain wall tuning in BaTiO<sub>3</sub>(111)/CoFeB multiferroics, *APL Materials* **11**, 071112 (2023)
- [133] G. H. Kwei, A. C. Lawson, S. J. Billinge and S. W. Cheong, Structures of the ferroelectric phases of barium titanate, *Journal of Physical Chemistry* **97**, 2368 (1993)
- [134] R. A. Evarestov and A. V. Bandura, First-principles calculations on the four phases of BaTiO<sub>3</sub>, *Journal of Computational Chemistry* **33**, 1123 (2012)
- [135] M. Uludogan, D. P. Guarin, Z. E. Gomez, T. Cagin and W. Goddard, DFT Studies on Ferroelectric Ceramics and Their Alloys: BaTiO<sub>3</sub>, PbTiO<sub>3</sub>, SrTiO<sub>3</sub>, AgNbO<sub>3</sub>, AgTaO<sub>3</sub>, Pb<sub>x</sub>Ba<sub>1-x</sub>TiO<sub>3</sub> and Sr<sub>x</sub>Ba<sub>1-x</sub>TiO<sub>3</sub>, *Computer Modeling in Engineering and Sciences* **24**, 215 (2008)
- [136] K. Momma and F. Izumi, VESTA 3 for three-dimensional visualization of crystal, volumetric and morphology data, *Journal of Applied Crystallography* **44**, 1272 (2011)
- [137] M. Acosta, N. Novak, V. Rojas, S. Patel, R. Vaish et al., BaTiO<sub>3</sub>-based piezoelectrics: Fundamentals, current status, and perspectives, *Applied Physics Reviews* **4**, 041305 (2017)
- [138] C. A. F. Vaz, J. Hoffman, A.-B. Posadas and C. H. Ahn, Magnetic anisotropy modulation of magnetite in Fe<sub>3</sub>O<sub>4</sub>/BaTiO<sub>3</sub>(100) epitaxial structures, *Applied Physics Letters* **94**, 022504 (2009)
- [139] G. Venkataiah, Y. Shirahata, I. Suzuki, M. Itoh and T. Taniyama, Strain-induced reversible and irreversible magnetization switching in Fe/BaTiO<sub>3</sub> heterostructures, *Journal of Applied Physics* **111**, 033921 (2012)
- [140] T. H. E. Lahtinen and S. van Dijken, Temperature control of local magnetic anisotropy in multiferroic CoFe/BaTiO<sub>3</sub>, *Applied Physics Letters* **102**, 112406 (2013)

- 
- [141] R. Moreno, R. F. L. Evans, S. Khmelevskiy, M. C. Muñoz, R. W. Chantrell et al., Temperature-dependent exchange stiffness and domain wall width in Co, *Phys. Rev. B* **94**, 104433 (2016)
- [142] S. N. Kim, Y. J. Nam, Y. D. Kim, J. W. Choi, H. Lee et al., Formation of magnetic anisotropy by lithography, *Scientific Reports* **6**, 26709 (2016)
- [143] P. Baláž, S. J. Hämäläinen and S. van Dijken, Static properties and current-induced dynamics of pinned  $90^\circ$  magnetic domain walls under applied fields: An analytic approach, *Physical Review B* **98**, 064417 (2018)
- [144] P. Baláž, Interaction of in-plane magnetic skyrmions with  $90^\circ$  magnetic domain walls: Micromagnetic simulations, *Physical Review Applied* **17**, 044031 (2022)
- [145] B. V. de Wiele, S. J. Hämäläinen, P. Baláž, F. Montoncello and S. van Dijken, Tunable short-wavelength spin wave excitation from pinned magnetic domain walls, *Scientific Reports* **6**, 21330 (2016)
- [146] S. J. Hämäläinen, M. Madami, H. Qin, G. Gubbiotti and S. van Dijken, Control of spin-wave transmission by a programmable domain wall, *Nature Communications* **9**, 4853 (2018)
- [147] H. Qin, R. Dreyer, G. Woltersdorf, T. Taniyama and S. van Dijken, Electric-field control of propagating spin waves by ferroelectric domain-wall motion in a multiferroic heterostructure, *Advanced Materials* **33**, 2100646 (2021)
- [148] G. Koster, B. Kropman, A. Rijnders, D. Blank and H. Rogalla, Quasi-ideal strontium titanate crystal surfaces through formation of stontium hydroxide, *Applied physics letters* **73**, 2920 (1998)
- [149] J. Choi, C. B. Eom, G. Rijnders, H. Rogalla and D. H. A. Blank, Growth mode transition from layer by layer to step flow during the growth of heteroepitaxial SrRuO<sub>3</sub> on (001) SrTiO<sub>3</sub>, *Applied Physics Letters* **79**, 1447 (2001)
- [150] F. Sánchez, G. Herranz, I. C. Infante, J. Fontcuberta, M. V. García-Cuenca et al., Critical effects of substrate terraces and steps morphology on the growth mode of epitaxial SrRuO<sub>3</sub> films, *Applied Physics Letters* **85**, 1981 (2004)



- 
- [151] G. Koster, L. Klein, W. Siemons, G. Rijnders, J. S. Dodge et al., Structure, physical properties, and applications of SrRuO<sub>3</sub> thin films, *Reviews of Modern Physics* **84**, 253 (2012)
- [152] R. Bachelet, F. Sánchez, J. Santiso and J. Fontcuberta, Reversible growth-mode transition in SrRuO<sub>3</sub> epitaxy, *Applied Physics Letters* **93**, 151916 (2008)
- [153] Z.-Z. Jiang, Z. Guan, N. Yang, P.-H. Xiang, R.-J. Qi et al., Epitaxial growth of BiFeO<sub>3</sub> films on SrRuO<sub>3</sub>/SrTiO<sub>3</sub>, *Materials Characterization* **131**, 217 (2017)
- [154] S. Greculeasa, G. Schinteie, L. Hrib, V. Stancu, I. Pasuk et al., Complex exchange coupling mechanisms in SRO/BFO/fe heterostructures, *Journal of Alloys and Compounds* **773**, 338 (2019)
- [155] A. J. Ying, C. E. Murray and I. C. Noyan, A rigorous comparison of x-ray diffraction thickness measurement techniques using silicon-on-insulator thin films, *Journal of Applied Crystallography* **42**, 401 (2009)
- [156] B. D. Schrag, A. Anguelouch, S. Ingvarsson, G. Xiao, Y. Lu et al., Néel “orange-peel” coupling in magnetic tunneling junction devices, *Applied Physics Letters* **77**, 2373 (2000)
- [157] H. Béa, M. Bibes, F. Ott, B. Dupé, X.-H. Zhu et al., Mechanisms of exchange bias with multiferroic BiFeO<sub>3</sub> epitaxial thin films, *Physical Review Letters* **100**, 017204 (2008)
- [158] R. O. M. Aboljadayel, C. J. Kinane, C. A. F. Vaz, D. M. Love, R. S. Weatherup et al., Determining the proximity effect-induced magnetic moment in graphene by polarized neutron reflectivity and x-ray magnetic circular dichroism, *ACS Applied Materials & Interfaces* **15**, 22367 (2023)
- [159] S. Y. Jang, S. H. Lim and S. R. Lee, Magnetic dead layer in amorphous CoFeB layers with various top and bottom structures, *Journal of Applied Physics* **107**, 09C707 (2010)
- [160] Z. Chen, J. Liu, Y. Qi, D. Chen, S.-L. Hsu et al., 180° ferroelectric stripe nanodomains in BiFeO<sub>3</sub> thin films, *Nano Letters* **15**, 6506 (2015)

- [161] A. J. Bell, Phenomenologically derived electric field-temperature phase diagrams and piezoelectric coefficients for single crystal barium titanate under fields along different axes, *Journal of Applied Physics* **89**, 3907 (2001)
- [162] S. J. Hämäläinen, F. Brandl, K. J. A. Franke, D. Grundler and S. van Dijken, Tunable short-wavelength spin-wave emission and confinement in anisotropy-modulated multiferroic heterostructures, *Physical Review Applied* **8**, 014020 (2017)
- [163] P. F. Liu, J. Miao, Z. D. Xu, G. Jakob, Q. Liu et al., Large modulation of perpendicular magnetic anisotropy in a BiFeO<sub>3</sub>/Al<sub>2</sub>O<sub>3</sub>/Pt/Co/Pt multiferroic heterostructure via spontaneous polarizations, *Applied Physics Letters* **113**, 062401 (2018)